

A study on nonhumidified fuel cells using
fluorohydrogenate ionic liquids

Pisit Kiatkittikul

2015

Contents

Chapter 1 General introduction

1.1	Necessity of renewable energy	1
1.2	Hydrogen energy system	2
1.3	Fuel cells	2
1.3.1	Basic principle of fuel cells	3
1.3.2	Polymer electrolyte fuel cells (PEFCs)	5
1.3.3	Membrane materials for PEFCs	6
1.3.4	Major drawbacks of conventional PEFCs and solutions	6
1.4	Fluorohydrogenate ionic liquid (FHILs) for fuel cells application	7
1.4.1	Ionic liquids (ILs)	7
1.4.2	Fluorohydrogenate ionic liquids (FHILs)	7
1.4.3	Application of FHILs to fuel cells	8
1.5	Literature reviews on PEFCs using ILs	9
1.5.1	Typical approaches of using ILs as electrolytes for PEFCs	9
1.5.2	IL-polymer composite membranes prepared by polymerization	11
1.5.3	IL-polymer composite membranes prepared by casting method	12
1.6	Oxygen reduction reaction in FHILs	14
1.6.1	ORR in EMIm(FH) _n F and EMPyr(FH) _n F	14
1.6.2	Catalytic activities of Pt alloys	15
1.7	Aim of this study	15
	References	17
	Tables and figures	23

Chapter 2 Experimental

2.1	Preparation of FHILs and apparatus	37
2.1.1	Preparation of FHILs	37
2.1.2	Preparation of FHIL-polymer composite membranes	38
2.1.3	Preparation of Pt alloys	39
2.1.4	Glove box	39
2.1.5	Vacuum line	39
2.2	Measurements of physical and electrochemical properties	40
2.2.1	Ionic conductivities of FHILs	40
2.2.2	Ionic conductivities of FHIL-polymer composite membranes	40
2.2.3	a.c. impedance method for ionic conductivity measurement	41

2.2.4	Thermogravimetry (TG)	41
2.2.5	Differential scanning calorimetry (DSC)	41
2.2.6	X-ray photoelectron spectroscopy	42
2.3	Fuel cell test	42
2.3.1	Fabrication of membrane-electrode assembly (MEA)	42
2.3.2	Single cell test under nonhumidified conditions	42
2.3.3	<i>In-situ</i> a.c. impedance analysis	43
2.3.4	Cross-sectional SEM observation	43
2.4	Electrochemical measurements using RDE and RRDE methods	44
2.4.1	A three-electrode cell	44
2.4.2	RDE method	45
2.4.3	RRDE method	45
	References	46
	Figures	47

Chapter 3 Preparation, characterization and fuel cell performance of EMPyr(FH)_{1.7}F–HEMA composite membranes using a PTFE membrane support

3.1	Introduction	53
3.2	Experimental	54
3.2.1	Preparation of EMPyr(FH) _{1.7} F–HEMA composite membranes using a PTFE membrane support	54
3.2.2	Characterizations of composite membranes	54
3.2.3	MEA fabrication and single cell test	55
3.2.4	Cross-sectional SEM observation	55
3.3	Results and discussion	56
3.3.1	Thermal stability and phase transition behavior	56
3.3.2	Ionic conductivity	56
3.3.3	Single cell performance under nonhumidified conditions	57
3.4	Conclusion	58
	References	60
	Figures	61

Chapter 4 Preparation, characterization and fuel cell performance of EMPyr(FH)_{1.7}F–HEMA composite membranes using a PI membrane support

4.1	Introduction	67
-----	--------------	----

4.2	Experimental	68
4.2.1	Preparation of EMPyr(FH) _{1.7} F–HEMA composite membranes using a PI membrane support	68
4.2.2	Characterizations of composite membranes	69
4.2.3	MEA fabrication and single cell test	70
4.2.4	Cross-sectional SEM Observation	70
4.3	Results and discussion	71
4.3.1	Thermal stability	71
4.3.2	Ionic conductivity	71
4.3.3	Single cell performance under nonhumidified conditions	72
4.3.4	Cross-sectional SEM image	73
4.4	Conclusion	73
	References	75
	Table and figures	77

Chapter 5 Preparation, characterization and fuel cell performance of EMPyr(FH)_{1.7}F/PVdF-HFP composite membranes using no membrane support

5.1	Introduction	84
5.2	Experimental	85
5.2.1	Preparation of EMPyr(FH) _{1.7} F/PVdF-HFP composite membranes	86
5.2.2	Characterizations of composite membranes	86
5.2.3	MEA fabrication and single cell test	87
5.2.4	<i>In-situ</i> a.c. impedance analysis	87
5.2.5	Cross-sectional SEM observation	88
5.3	Results and discussion	88
5.3.1	Thermal stability	88
5.3.2	Ionic conductivity	89
5.3.3	Surface morphology	89
5.3.4	Single cell performance under nonhumidified conditions	90
5.3.5	<i>In-situ</i> a.c. impedance	90
5.3.6	Cross-sectional SEM image	91
5.4	Conclusion	92
	References	93
	Table, scheme and figures	94

<u>Chapter 6</u>	Influence of cationic structures on oxygen reduction reaction at Pt electrode in fluorohydrogenate ionic liquids	
6.1	Introduction	106
6.2	Experimental	107
6.2.1	Preparation of FHILs	107
6.2.2	Electrochemical measurement	108
6.3	Results and discussion	108
6.3.1	Kinetically limited current density	108
6.3.2	Yield of H ₂ O ₂	110
6.3.3	Solubility and diffusion coefficient of oxygen	112
6.4	Conclusion	115
	References	117
	Tables and figures	119
<u>Chapter 7</u>	Catalytic activities of Pt-M alloys (M = Fe, Co, Ni) on oxygen reduction reaction in a fluorohydrogenate ionic liquid	
7.1	Introduction	131
7.2	Experimental	132
7.2.1	Preparation of Pt alloys	132
7.2.2	X-ray photoelectron spectroscopy	133
7.2.3	Electrochemical measurement	133
7.2.4	Field emission scanning electron microscope	133
7.3	Results and discussion	134
7.3.1	XPS analysis before electrochemical measurement	134
7.3.2	Rate constant of ORR	134
7.3.3	XPS analysis after electrochemical measurement	135
7.3.4	FE-SEM observation	136
7.4	Conclusion	137
	References	138
	Figures	140
<u>Chapter 8</u>	General conclusion	145
	List of publications	148
	Acknowledgments	150

Chapter 1

General introduction

1.1 Necessity of renewable energy

In the most recent decades, ones of the most concerned global issues are energy crisis and environmental crisis. With the rapid growth of human population and civil industry, the natural resource has being consumed with an increasingly high pace.

Over 75% of the world current primary energy supply comes from fossil fuels (oil, coal, natural gas, etc.) [1], which are nonrenewable. Along with the increasingly high consuming rate, the lack of energy supply (energy crisis) is inevitable in the near future. Some traces of this problem can be seen from the rise of fossil fuels prices in the recent decades. Fig. 1-1 shows the exponential rise of prices of various oil-based products [2]. This indicates that the fossil fuels reserves are reaching their full capacities. Therefore, the exploration for new sustainable energy sources is an indispensable task in order to lessen the dependence on fossil fuels.

While the solution for the energy crisis has become a major task, another serious problem called “environmental crisis” is an important issue that should not be dismissed. Fig. 1-2 presents the global CO₂ emissions from fossil fuel uses from 1990 to 2010 [3]. The increase of CO₂ emissions in the past decades is obvious. To make thing worse, it is even on the exponential rise.

For these reasons, it is necessary to find a new alternative energy source which is also more environmental friendly. Various efforts have been made in the series of renewable energies such as solar energy, wind energy, geothermal energy, etc. Among

them, hydrogen energy has been receiving much attention in the recent decades.

1.2 Hydrogen energy system

Hydrogen is an abundant element. About 75% of this universe is composed of hydrogen. It contains a large amount of energy in its chemical bond, which makes it an ideal alternative energy source. Hydrogen energy is generated from a chemical reaction between hydrogen and oxygen, which subsequently produces water. Hydrogen is similar to electricity in the way that it carries energy. However, it can be easily stored and transported to wherever it is needed. Hydrogen energy can also be used in areas where electricity is unavailable, such as in water. Another advantage is that hydrogen is much lighter than fossil fuels.

Hydrogen energy system is, to put it simply, an energy system that is based on the use of hydrogen as an energy carrier. It contains the major components as follows;

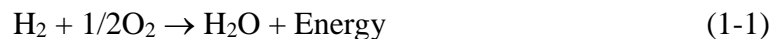
- (i) Hydrogen production system: Not much hydrogen gas is existed on earth. It must be extracted from other substances such as water or other natural gases.
- (ii) Hydrogen storage system: Hydrogen can be stored in many ways, for examples, as hydrogen gas or in metal compound.
- (iii) Electricity generating system: As described previously, to get energy from hydrogen, it is reacted with oxygen. The most common device used to convert hydrogen energy into electricity is “Fuel cell”. This is the main topic of this study and will be discussed later in more details
- (iv) Electricity storage system: Batteries, etc.

1.3 Fuel cells

Fuel cells are electrochemical devices that convert chemical energy directly into electrical energy. Unlike batteries, fuel cells do not wear out so that recharging is not required. This means that they can run as long as the fuel (usually hydrogen) is continuously supplied. They also operate quietly and efficiently in which the wastes are only water and heat. Thus, they are also called “zero emission engine”. When the generated heat is efficiently utilized, the total energy conversion efficiency of fuel cell can reach as high as 85% [4–5]. With these advantages, fuel cells are widely recognized as ones of the most promising and outstanding alternative energy conversion devices.

1.3.1 Basic principle of fuel cells

The basic operation principle of fuel cells is very simple. With the reversed electrolysis of water, hydrogen and oxygen recombine into water while electric power is generated as shown below.



The only visible product of this reaction is water. Here, energy is always generated as a by-product.

The generated energy is in the form of enthalpy (ΔH), which can be calculated from the difference between the heats of formation of products and reactants. At 25 °C under atmospheric pressure, the heat of formation of water is -286 kJ mol^{-1} while those of elements are equal to zero. Therefore:

$$\Delta H = (h_f)_{\text{H}_2\text{O}} - (h_f)_{\text{H}_2} - 1/2(h_f)_{\text{O}_2} = -286 - 0 - 0 = -286 \text{ kJ mol}^{-1} \quad (1-2)$$

The negative sign for enthalpy means that this is an exothermic reaction, in which the energy is being released. Equation (1-1) can be re-written as:



However, not all of this enthalpy can be converted into electricity. There are always some irreversible losses in energy conversion due to the increase of entropy (ΔS), according to the second law of thermodynamics. The only portion of enthalpy that can be converted into electricity corresponds to Gibbs free energy (ΔG) as given by the following equation.

$$\Delta G = \Delta H - T\Delta S \quad (1-4)$$

Similar to ΔH , ΔS can be calculated from the difference between entropies of products and reactants. At 25 °C under atmospheric pressure, it is calculated to be:

$$\Delta S = (s_f)_{\text{H}_2\text{O}} - (s_f)_{\text{H}_2} - 1/2(s_f)_{\text{O}_2} = -0.163285 \text{ kJ mol}^{-1}\text{K}^{-1} \quad (1-5)$$

By subtracting the calculated ΔS into equation (1-3), ΔG is calculated to be 237.34 kJ mol⁻¹. This means from the total energy of 286.02 kJ mol⁻¹, only 237.34 kJ mol⁻¹ can be converted into electricity while the remaining 48.68 kJ mol⁻¹ is released as heat.

ΔG is corresponded to the maximum amount of electrical energy (W) generated by fuel cell.

$$W = -\Delta G \quad (1-6)$$

And electrical work is a product of charge and potential.

$$W = qE = nFE \quad (1-7)$$

Where n = number of electrons per molecule and F = Faraday's constant

Hence, the theoretical potential of fuel cell is:

$$E = -\Delta G/nF \quad (1-7)$$

At 25 °C under atmospheric pressure, the theoretical fuel cell potential is calculated to be 1.23 V.

For comparison with other energy conversion devices, here, the theoretical efficiency (η) of fuel cell is also calculated. Given that all of the Gibbs free energy is

converted into electrical energy, the theoretical efficiency of a fuel cell can be calculated by dividing the output electrical energy (ΔG) with the input enthalpy (ΔH) as follows:

$$\eta = \Delta G/\Delta H = 237.34/286.02 = 83\% \quad (1-9)$$

This value is considerably high compared with conventional combustion engines, whose theoretical efficiencies are around 30% to 60%.

1.3.2 Polymer electrolyte fuel cells (PEFCs)

Fuel cells can be divided into various types based on the electrolyte materials. Among them, the major types of fuel cells which are expected for practical applications are summarized in Table 1-1. Each type of fuel cells is suitable for the use in different range depending on the operation temperature and applications.

Polymer electrolyte fuel cells (PEFCs) are different from other types of fuel cell in the point that they use a layer of proton conducting solid polymer electrolyte. They were first developed at General Electric by W.T. Grubb and L.W. Niedrach [6], and provided on-board electrical power for the Gemini Earth-orbiting program for the U.S. space discovery. A new polymer formulation (Nafion[®]), developed by W. G. Grot at Dupont in 1972 [7], improved the performance and durability of the electrolyte. Furthermore, the electrode fabrication was improved by I. D. Raistrick in 1986 in the form of gas diffusion electrode (GDE) [8]. These achievements largely contributed to the advancement of fuel cell development especially for transportation and portable devices [9].

Recently, PEFCs receive more and more attention due to their wide range of applications, from a micro-sized electrical device to a large-scaled power generation unit. Moreover, because of their considerably low operating temperature, they have

short start-up time and are easy to be handled.

1.3.3 Membrane materials for PEFCs

Membrane is the core component for PEFCs. It typically works as a protons transmitter as well as electrons barrier to complete the chemical reaction of fuel cells. To achieve high efficiency, the membrane is required to have the following properties [10];

- (v) High proton conductivity to support high currents with minimal resistive losses and zero electronic conductivity
- (vi) Adequate mechanical strength and stability
- (vii) Chemical and electrochemical stability under operating conditions
- (viii) Extremely low fuel or oxygen crossover
- (ix) Low production costs

The most famous membrane material used for PEFCs is Nafion[®], which is made from perfluorosulfonated (PFSA) compounds. The chemical structure of Nafion[®] is shown in Fig. 1-4.

1.3.4 Major drawbacks of conventional PEFCs and solutions

The conventional PEFCs, using Nafion[®] membrane, require sufficient humidity (water) for ionic conduction [4–5, 11–14]. This results in the restriction of operating temperature (below 100 °C due to the boiling point of water) and the requirement of a complicated humidification system. Also, because of their low operating temperature, large amount of noble metal catalyst such as Pt is needed to increase the reaction rate. This results in high cost of production. Thus, as a solution to these major drawbacks, a

new electrolyte membrane which enables an operation at elevated temperature without humidification is required.

Many types of proton conducting materials have been developed as alternative membrane electrolytes such as modified perfluorosulfonic acid (PFSA) polymer membranes [14–16], sulfonated hydrocarbon polymer membranes [17–19], acid-base complex membranes [20–2] and polybenzimidazole (PBI) based polymer membranes [23–26].

1.4 Fluorohydrogenate ionic liquid (FHILs) for fuel cells application

1.4.1 Ionic liquids (ILs)

Ionic liquids (ILs, also called room temperature molten salts, RTMSs) are salts in liquid state under room temperature. ILs have recently attracted much attention for applying to electrochemical devices and reaction media due to their notable properties such as high chemical and thermal stability, nonflammability, nonvolatility, and wide electrochemical window [27–29]. After the discovery of 1-ethyl-3-methylimidazolium tetrafluoroborate (EMImBF₄) which is stable in both air and water by J. S. Wilkes et al. [30], many RTILs containing various aromatic or nonaromatic cations and fluorocomplex or halogen-free anions, as shown in Fig. 1-1, have been synthesized and investigated from the viewpoints of academic interest and practical applications such as batteries as well as reaction and extraction solvents.

1.4.2 Fluorohydrogenate ionic liquids (FHILs)

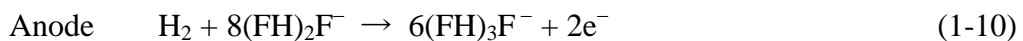
Fluorohydrogenate ionic liquids (FHILs) are a kind of RTILs which consists of organic cations and fluorohydrogenate anions ((FH)_nF⁻), as shown in Fig. 1-2. Here, *n*

number represents average number of ligand HF attached to fluoride anion. This n number decreased when the evacuation temperature increases, which means more HF is removed from FHILs to be stabilized at higher temperature.

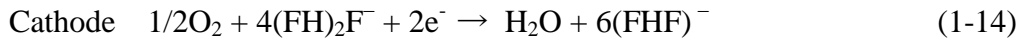
In 1999, the first FHIL, 1-ethyl-3-methylimidazolium fluorohydrogenate (EMIm(FH) $_n$ F), was reported [31]. It exhibits high conductivity (100 mS cm $^{-1}$ at 25 °C), low melting point and glass transition temperatures (−65 and −125 °C). With these excellent properties, FHILs are promising for electrochemical applications. In recent years, a series of FHILs with different cations have been studied and reported [32–39]. One of them, *N*-ethyl-*N*-methylpyrrolidinium fluorohydrogenate (EMPyr(FH) $_{2.3}$ F), was reported to possess good electrochemical stability and have a wider electrochemical window (4.6 V) [35]. In addition, the ionic conductivity was as high as 74.6 mS cm $^{-1}$ at 25 °C.

1.4.3 Application of FHILs to fuel cells

It has already been demonstrated that EMIm(FH) $_{2.3}$ F (structure is shown in Fig. 1-2 (a)) is applicable for a non-humidified fuel cell [40–41]. Because of a unique mechanism of hydrogen and charge transportation using fluorohydrogenate anions, water is not required for the fuel cell operation. Therefore, this type of fuel cell, which was named fluorohydrogenate fuel cell (FHFC), operates under non-humidified condition at elevated temperature. The principle of FHFC ($2 < n < 3$) is shown in Fig. 1-3 (a). The half and total reactions are expressed as:



The n number can be reduced by evacuation elevated temperatures [35]. If EMIm(FH)_{2.3}F is evacuated at 120 °C, the n number is reduced to 1.3. The principle of FHFC in the case of ($1 < n < 2$) is shown in Fig. 1-3 (b). The half and total reactions are expressed as:



In the recent studies, EMPyr(FH)_{1.7}F, whose structure is shown in Fig. 1-2 (b), was found to exhibit higher activity for the oxygen reduction reaction (ORR) on a Pt electrode compared with EMIm(FH)_{1.3}F [42]. It was also revealed that it possesses adequate oxygen permeability with the crossover current as low as 0.143 mA cm⁻² in the case of 177.8 μm electrolyte thickness [43]. These results indicated that EMPyr(FH)_{1.7}F is a very promising electrolyte for FHFCs.

1.5 Literature reviews on PEFCs using ILs

1.5.1 Typical approaches of using ILs as electrolytes for PEFCs

As explained in the previous section, operation at intermediate temperature (> 100 °C) without humidification offers some prominent benefits for PEFCs such as higher efficiency of reaction, reduction of CO poisoning on the Pt catalyst, and simplicity of the unit (due to the removal of humidity management systems). However, most of the conventional perfluorinated sulfonic acid membranes are found to exhibit poor proton conductivities at above 100 °C due to their temperature and humidity dependence. As potential proton (or ion) conductors, ILs have recently received much attention due to their nonvolatility, nonflammability, high ion densities and relatively

high ionic conductivities. Some of them also have wide liquid-phase temperature range which allows the fuel cell operation at over 100 °C [41]. However, to make them applicable for the use as electrolytes for PEFCs, ILs are required to be processed into a solid or quasi-solid form. To answer this need, Angell et al. proposed the concept of a “polymer-in-salt” to obtain highly conductive polymer electrolytes based on the preparation of IL-based polymer electrolytes [44].

Fig. 1-9 shows schematic representation of various methods for IL-based polymer electrolytes preparations. The preparation methods can be categorized into 3 main routes [45]. The first one is by doping (or impregnating) polymer with ILs. This method can be further divided into 2 ways as follows; (1a) mixing ILs with a soluble polymer and then casting into thin film (so-called “casting method”), (1b) impregnating ILs into a polymer membrane. Casting method is the most popular method which is widely used for the preparation of IL-based polymer electrolytes. The second route is by polymerization or crosslinking of the monomers in ILs. This method can be applied by either; (2a) polymerization of IL-monomer mixed solution, or (2b) blending ILs with macro-monomers and crosslinkers. The molecular size of the prepared polymer electrolytes can be modified by controlling the degree of polymerization or the type of monomer itself. However, a porous supporting material may be needed to function as a membrane skeleton. Finally, IL-based polymer electrolytes can also be prepared from polymeric ionic liquids (PILs). In this route, the ILs themselves also works as polymer. In most cases, PILs with polymerizable cations are polymerized to form a polymer electrolyte membrane (3a). An alternative route is to use an anion-exchangeable polymer (3b). After preparing the polymer membrane from it, highly conductive anions are added by anion-exchange mechanisms.

1.5.2 IL-polymer composite membranes prepared by polymerization

As mentioned earlier, by polymerizing a mixture of IL and monomer, a gel-like conductive polymer is obtained. This so-called “ion gel” can be used as electrolyte for PEFCs, giving advantages in terms of improved safety and a higher operating temperature range [46]. Since the composite membrane was prepared from a mixed solution of IL and monomer (via polymerization), it is indispensable to ensure a good compatibility between the selected IL and monomer. This means the monomer needs to be (1) soluble and unreacted with the partnered IL and (2) polymerizable in the presence of that IL.

Table 1-2 shows some combinations of IL and monomer used to prepare polymer composite membranes via polymerization. Various monomers were studied for their compatibilities with a series of ILs; [EMIm][BF₄], [BPy][BF₄], [EMIm][(FH)_{2.3}F] and [EMIm][TFSI] [46-48]. Most of them were reportedly unreacted with the corresponding ILs. However, very few of them were polymerized in the presence of ILs. Moreover, there were a lot of cases in which phase separation occurred during the polymerization. Among these monomers, 2-hydroxyethylmethacrylate (HEMA) showed the best capability as a monomer for IL-based ion gel. It was reported to be compatible with all of the selected ILs and also polymerizable with most of them. It should be noted that a composite polymer electrolyte consisting of HEMA and FHIL has been successfully prepared by Tsuda et al using [EMIm][(FH)_{2.3}F] as an FHIL. Hence, in this study, HEMA monomer was chosen.

However, these ion gel-based polymer electrolytes have one major problem. Prepared from relatively small-size monomer, most of the prepared ion gels are soft and

may not be suitable as electrolyte membranes for PEFCs. For this reason, crosslinkers may be added to provide strong, self-standing and flexible films [46, 48]. Another solution is to use a porous supporting material to act as a skeleton of the composite membrane to improve the mechanical strength. In this study, two types of porous supporting materials made from; (1) polytetrafluoroethylene (PTFE) and (2) polyimide (PI) were used. The more details will be discussed again in chapter 3 and chapter 4.

1.5.3 IL-polymer composite membranes prepared by casting method

To prepare an IL-polymer composite membrane, the most well-known and widely used route is by mixing an IL with a polymer solution (dissolved in a suitable solvent) and then casting into a thin film. This route is called “casting method” [45]. A variety of combinations of polymer and IL were prepared and studied for their potentials as an electrolyte membrane for PEFCs [49–73]. In many cases, acid doping or sulfonation were employed to increase the ionic conductivity.

Table 1-3 summarizes the IL-polymer composite membranes prepared by casting method, also providing the casting conditions, their ionic conductivities and the power densities measured in the actual single cell test. Among various polymers, poly(vinylidene fluoride-co-hexafluoropropylene) (PVdF-HFP) was intensively studied by many research groups [49–55]. Malis et al. prepared polymer electrolytes consisting of PVdF-HFP and either 1-butyl-3-methylimidazolium trifluoromethylsulfonate ([BMIm][TfO]) or *N*-ethylimidazolium trifluoromethylsulfonate ([EMIm][TfO]) [49]. They were reportedly thermally stable up to 140 °C. At 140 °C, single cell tests under anhydrous conditions revealed that these composite membranes showed the maximum power densities of 0.6 and 0.12 mW cm⁻², respectively. Sekhon et al. also prepared

composite membranes of PVdF-HFP and 2,3-dimethyl-1-octylimidazolium trifluoromethylsulfonate ([DMOIm][TfO]) or 2,3-dimethyl-1-octylimidazolium bis(trifluoromethylsulfonyl)imide ([DMOIm][TFSI]) [50–51]. The maximum power densities at 100 °C under anhydrous conditions were 1.0 and 0.2 mW cm⁻², respectively. These values are, however, very low compared with the maximum power density of the conventional PEFCs. Other than PVdF-HFP, poly(vinylidene fluoride) (PVdF), poly(vinyl pyrrolidone) (PVP), poly(styrene) (PS), poly(ethylene glycol) (PEO), poly(methyl methacrylate) (PMMA) and poly(aryl ether ketone) (PAEK) have been investigated by various research groups [56–60]. However, none of them was actually tested in the practical fuel cell operation. There are also many reports for the IL-based polymer composite membranes prepared using poly(ether ether ketone) (PEEK) [61–64] and poly(imide) (PI) [65–69]. In a study by Yasuda et al., the composite membrane of sulfonated polyimide (sPI) and diethylmethylammonium trifluoromethylsulfonate ([dema][TfO]) was found to give the maximum power density of 100 mW cm⁻² at 120 °C under anhydrous conditions, which was very promising [69]. Apart from the polymers described above, many researches have recently been conducted using poly(benzimidazole) (PBI) [70–73]. However, as mentioned earlier, the composite membranes of solely PBI have already been regarded as potential alternative membrane materials for PEFC. Addition of ILs is likely to be done in order to further increase their ionic conductivities.

In case of FHILs, Lee et al. have successfully prepared composite membranes containing EMIm(FH)_nF (*n* = 1.3 and 2.3) and PVdF-HFP [41]. The single cell using one of these membranes was found to exhibit the maximum power density of 20 mW cm⁻². Considering the fact that EMIm(FH)_nF has low ORR activity. A better result can

be expected if PVdF-HFP is incorporated with an FHIL that possesses higher ORR activity, such as EMPyr(FH)_{*n*}F (*n* = 1.7 and 2.3). For this reason, casting method was used for the preparation of the composite membranes consisting of EMPyr(FH)_{1.7}F and PVdF-HFP. This topic will be discussed further in chapter 5.

1.6 Oxygen reduction reaction in FHILs

In the previous study, it has been reported that the contributions of anode overpotential and IR drop to the overall overpotential were negligibly small compared with the cathode overpotential [42–43]. This means that cathode overpotential is the main factor that determines the cell performance. Hence, improvement of ORR activity is an important task to improve the cell performance.

1.6.1 ORR in EMIm(FH)_{*n*}F and EMPyr(FH)_{*n*}F

As mentioned above, the ORR activities in EMIm(FH)_{*n*}F and EMPyr(FH)_{*n*}F have already been investigated in the previous studies, in which EMPyr(FH)_{*n*}F exhibited a significantly better result [42–43]. A further study also revealed that EMPyr(FH)_{1.7}F has the values of solubility and diffusion coefficient of oxygen that are comparable to Nafion [43]. For this reason, EMPyr(FH)_{1.7}F was focused in this study. However, it is also possible that there may be other FHILs that possess even higher ORR activity. For this reason, the investigations on ORR activity for other FHILs are necessary. In chapter 6, a series of FHILs were prepared and investigated for their ORR parameters, such as kinetically limited current density (j_k), yield of H₂O₂ ($X_{H_2O_2}$), and solubility (*C*) and diffusion coefficient (*D*) of oxygen, a on Pt electrode at 25 °C. The detailed results will be explained in chapter 6.

1.6.2 Catalytic activities of Pt alloys

Since the ORR activity is directly related to the activity of catalyst, developing a catalyst which has high catalytic activity is another way to improve the cell performance. Pt-alloys, such as Pt-Fe, Pt-Co, and Pt-Ni alloys, were reported to have higher catalytic activities than a pristine Pt in aqueous acidic solutions [74–76]. However, the ORR on the cathode of FHFCs is not the reaction with protons but with fluorohydrogenate anions. Thus, it is conceivable that the ORR mechanism in FHILs may differ from that in the conventional proton-conductive electrolytes. In other words, catalysts uniquely effective for the cathode of FHFCs may exist. Hence, it is interesting to figure out whether the Pt-alloys also have high catalytic activities in FHILs or not. In chapter 7, Pt-Fe, Pt-Co and Pt-Ni alloys were prepared, characterized and investigated for their catalytic activities in EMPyr(FH)_{1.7}F.

1.7 Aim of this study

The main propose of this study is to develop an FHIL-based non-humidified fuel cell with high single cell performance and good durability. In this study, various efforts have been made through 2 main aspects: (i) preparation, characterization and fuel cell performance evaluation of novel composite membranes and (ii) investigation of the influences of cation structures and Pt-alloy electrodes on ORR activities.

In chapter 2, apparatus and techniques required for the synthesis of FHILs and the preparation of FHIL-polymer composite membranes are described. The apparatus for thermal and electrochemical properties measurement as well as details on fuel cell operations are also given.

In chapter 3, the composite membranes of EMPyr(FH)_{1.7}F and HEMA prepared by polymerization using PTFE supporting material have been studied. Their potentials as membrane materials for a nonhumidified fuel cell are discussed.

In chapter 4, similar to chapter 3, EMPyr(FH)_{1.7}F-HEMA composite membranes have been prepared via polymerization. However, to improve thermomechanical properties, the porous supporting material has been changed from PTFE to PI, which has better mechanical strength and higher thermal deformation temperature. The single cells using PI-equipped membranes have been prepared, characterized and tested for fuel cell performance. The temperature dependence of cell performance is discussed.

In chapter 5, the composite membranes of EMPyr(FH)_{1.7}F and PVdF-HFP have been prepared, without membrane support, by casting method. Physical and electrochemical properties of the prepared membranes have been investigated. Then, single cell tests have been carried out.

In chapter 6, various parameters related to the ORR on a Pt electrode such as j_k , $X_{\text{H}_2\text{O}_2}$, and C and D of oxygen have been evaluated at 25 °C in various FHILs using the rotating ring-disk electrode (RRDE) method.

In chapter 7, rate constants of ORR (k) on Pt and Pt-alloys electrode in EMPyr(FH)_{1.7}F have been evaluated. As Pt-alloys, Pt-Fe, Pt-Co, and Pt-Ni have been employed, because they have been reported to have higher specific activities than Pt in aqueous acidic solution.

Finally, results from each chapter were summarized to give a general conclusion in chapter 8.

References

- [1] International Energy Agency, *World Energy Outlook 2013: Fact sheet*, Paris, 2013.
(www.worldenergyoutlook.org)
- [2] BP p.l.c., *Statistical Review of World Energy June 2013*, London, 2013.
(www.bp.com/statisticalreview)
- [3] PBL Netherlands Environmental Assessment Agency, *Trends in global CO₂ emissions: 2013 Report*, Hague, 2013.
- [4] J. Larminie, A. Dicks, *Fuel Cell Systems Explained (2nd Ed.)*, John Wiley & Sons Ltd, West Sussex, 2003.
- [5] F. Barbir, *PEM Fuel Cells: Theory and Practice*, Elsevier Academic Press, New York, 2005.
- [6] W. T. Grubb, L.W. Niedrach, *J. Electrochem. Soc.* **107** (1960) 131.
- [7] R. L. Coalson, W. G. Grot, *US Patent* 3,684,747 (1972).
- [8] I. Raistrick, *Diaphragms Separators and Ion exchange Membrane* **86** (1986) 172.
- [9] G. Hoogers, *Fuel Cell Technology Handbook*, CRC Press, Florida, 2003.
- [10] Q. F. Li, H. A. Hjuler, N. J. Bjerrum, *Electrochim. Acta* **45** (2000) 4219.
- [11] C. Yang, P. Costamagna, S. Srinivasan, J. Benziger, A. B. Bocarsly, *J. Power Sources* **103** (2001) 1.
- [12] K. D. Kreuer, S. J. Paddison, E. Spohr, M. Schuster, *Chem. Rev.* **104** (2004) 4637.
- [13] F. Meier, G. Eigenberger, *Electrochim. Acta* **49** (2004) 1731.
- [14] M. A. Hickner, H. Ghassemi, Y. S. Kim, B. R. Einsla, J. E. McGrath, *Chem. Rev.* **104** (2004) 4587.
- [15] I. Gatto, A. Sacca, A. Carbone, R. Pedicini, E. Passalacqua, *J. Fuel Cell Sci. Techno.* **3** (2006) 361.

- [16]H. Xiuchong, T. Haolin, P. Mu, *J. Appl. Polym. Sci.* **108** (2008) 529.
- [17]J. H. Chang, J. H. Park, G. G. Park, C. S. Kim, O. O. Park, *J. Power Sources* **124** (2003) 18.
- [18]B. Lakshmanan, W. Huang, D. Olmeijer, J. W. Weidner, *Electrochem. Solid-State Lett.* **6** (2003) A282.
- [19]T. Higashihara, K. Matsumoto, M. Ueda, *Polymer* **50** (2009) 5341.
- [20]M. Rikukawa, K. Sanui, *J. Prog. Polym. Sci.* **25** (2000) 1463.
- [21]X. Chen, P. Chen, Z. An, K. Chen, K. Okamoto, *J. Power Sources* **196** (2011) 1694.
- [22]J. S. Wainright, J.T. Wang, D. Weng, R. F. Savinell, M. Litt, *J. Electrochem. Soc.* **142** (1995) L121.
- [23]J. Lobato, P. Canizares, M. A. Rodrigo, J. J. Linares, G. Manjavacas, *J. Membrane Sci.* **280** (2006) 351.
- [24]D. Plackett, A. Siu, Q. Li, C. Pan, J. O. Jensen, S. F. Nielsen, A. A. Permyakova, N. J. Bjerrum, *J. Membrane Sci.* **383** (2011) 78.
- [25]Y. C. Jin, M. Nishida, W. Kanematsu, T. Hibino, *J. Power Sources* **196** (2011) 6042.
- [26]S. Angioni, P.P. Righetti, E. Quartarone, E. Dilena, P. Mustarelli, A. Magistris, *Int. J. Hydrogen Energy* **36** (2011) 7174.
- [27]K. R. Seddon, *J. Chem. Technol. Biotechnol.* **68** (1997) 351.
- [28]T. Welton, *Chem. Rev.* **99** (1999) 2071.
- [29]P. Wasserscheid, W. Kein, *Angew. Chem. Int. Ed.* **39** (2000) 3772.
- [30]J. S. Wilkes, M. J. Zaworotko, *J. Chem. Soc., Chem. Commun.* **13**, (1992) 965.
- [31]R. Hagiwara, T. Hirashige, T. Tsuda, Y. Ito, *J. Fluorine Chem.* **99** (1999) 1.

- [32] R. Hagiwara, Y. Ito, *J. Fluorine Chem.* **105** (2000) 221.
- [33] R. Hagiwara, T. Hirashige, T. Tsuda, Y. Ito, *J. Electrochem. Soc.* **149** (2002) D1.
- [34] R. Hagiwara, K. Matsumoto, Y. Nakamori, T. Tsuda, Y. Ito, H. Matsumoto, K. Momota, *J. Electrochem. Soc.* **150** (2003) D195.
- [35] K. Matsumoto, R. Hagiwara, Y. Ito, *Electrochem. Solid-State Lett.* **7** (2004) E41.
- [36] K. Matsumoto, J. Ohtsuki, R. Hagiwara, S. Matsubara, *J. Fluorine Chem.* **127** (2006) 1339.
- [37] M. Yamagata, S. Konno, K. Matsumoto, R. Hagiwara, *Electrochem. Solid-State Lett.* **12** (2009) F9.
- [38] S. Kanematsu, K. Matsumoto, R. Hagiwara, *Electrochem. Commun.* **11** (2009) 1312.
- [39] T. Enomoto, S. Kanematsu, K. Tsunashima, K. Matsumoto, R. Hagiwara, *Phys. Chem. Chem. Phys.* **13** (2011) 12536.
- [40] R. Hagiwara, T. Nohira, K. Matsumoto, Y. Tamba, *J. Electrochem. Solid-State Lett.* **8** (2005) A231.
- [41] J.S. Lee, T. Nohira, R. Hagiwara, *J. Power Sources*, **171** (2007) 535.
- [42] T. Nohira, R. Hagiwara, M. Yamagata, K. Ogasawara, T. Hayashida, *Extended Abstracts of the 10th Meeting on Materials for Chemical Batteries in Japan, 2008*, p. 81.
- [43] Y. Tani, T. Nohira, T. Enomoto, K. Matsumoto, R. Hagiwara, *J. Electrochim. Acta* **56** (2011) 3852.
- [44] C. A. Angell, C. Liu and E. Sanchez, *Nature* **362** (1993) 137.
- [45] Y. S. Ye, J. Rick, B. J. Hwang, *J. Mater. Chem. A* **1** (2013) 2719.
- [46] A. Noda, M. Watanabe, *Electrochim. Acta* **45** (2000) 1265.

- [47] T. Tsuda, T. Nohira, Y. Nakamori, K. Matsumoto, R. Hagiwara, Y. Ito, *Solid State Ionics* **149** (2002) 295.
- [48] Md. A. B. H. Susan, T. Kaneko, A. Noda, M. Watanabe, *J. Am. Chem. Soc.* **127** (2005) 4976.
- [49] J. Malis, P. Mazur, J. Schauer, M. Paidar, K. Bouzek, *Int. J. Hydrogen Energy* **38** (2013) 4697.
- [50] S. S. Sekhon, B. Singh Lalia, J. S. Park, C. S. Kim, K. Yamada, *J. Mater. Chem.* **16** (2006) 2256.
- [51] S. S. Sekhon, P. Krishnan, B. Singh Lalia, K. Yamada, C. S. Kim, *Electrochim. Acta* **52** (2006) 1639.
- [52] M. A. Navarra, S. Panero, B. Scrosati, *Electrochem. Solid-State Lett.* **8** (2005) A324.
- [53] B. Singh Lalia, S. S. Sekhon, *Chem. Phys. Lett.* **425** (2006) 294.
- [54] A. Farnicola, S. Panero, B. Scrosati, M. Tamada, H. Ohno, *ChemPhysChem.* **8** (2007) 1103.
- [55] A. Farnicola, M. A. Navarra, S. Panero, *J. Appl. Electrochem.* **38** (2008) 993.
- [56] J. Xiang, R. Chen, F. Wu, L. Li, S. Chen, Q. Zou, *Electrochim. Acta* **56** (2011) 7503.
- [57] A. L. Saroj, R. K. Singh, S. Chandra, *Mat. Sci. and Eng. B* **178** (2013) 231.
- [58] M. W. Schulze, L. D. McIntosh, M. A. Hillmyer, T. P. Lodge, *Nano Lett.* **14** (2014) 122.
- [59] S. Zhang, K. H. Lee, C. D. Frisbie, T. P. Lodge, *Macromolecules* **44** (2011) 940.
- [60] E. K. Cho, J. S. Park, S. S. Sekhon, G. G. Park, T. H. Hyun, W. Y. Lee, C. S. Kim, S. B. Park, *J. Electrochem. Soc.* **156** (2009) B197.

- [61] Q. Che, B. Sun, R. He, *Electrochim. Acta* **53** (2008) 4428.
- [62] P. R. Jothi, S. Dharmalingam, *J. Mem. Sci.* **450** (2014) 389.
- [63] S. Yi, F. Zhang, W. Li, C. Huang, H. Zhang, M. Pan, *J. Mem. Sci.* **366** (2011) 349.
- [64] Q. Che, R. He, J. Yang, L. Feng, R. F. Savinell, *Electrochem. Comm.* **12** (2010) 647.
- [65] H. Deligöz, M. Yılmazoğlu, S. Yılmaztürk, Y. Şahin, K. Ulutaş, *Polym. Adv. Technol.* **23** (2012) 1156.
- [66] H. Deligöz, M. Yılmazoğlu, *J. Power Sources* **196** (2011) 3496.
- [67] S. Y. Lee, T. Yasuda, M. Watanabe, *J. Power Sources* **195** (2010) 5909.
- [68] S. Y. Lee, A. Ogawa, M. Kanno, H. Nakamoto, T. Yasuda, M. Watanabe, *J. Am. Chem. Soc.* **132** (2010) 9764.
- [69] T. Yasuda, S. Nakamura, Y. Honda, K. Kinugawa, S. Y. Lee, M. Watanabe, *ACS Appl. Mater. Interfaces* **4** (2012) 1783.
- [70] S. Liu, L. Zhou, P. Wang, F. Zhang, S. Yu, Z. Shao, B. Yi, *ACS Appl. Mater. Interfaces* **6** (2014) 3195.
- [71] J. T. Wang, S. L. C. Hsu, *Electrochim. Acta* **56** (2011) 2842.
- [72] H. Ye, J. Huang, J. J. Xu, N. K. A. C. Kodiweera, J. R. P. Jayakody, S. G. Greenbaum, *J. Power Sources* **178** (2008) 651.
- [73] L. C. Jheng, S. L. C. Hsu, T. Y. Tsai, W. J. Y. Chang, *J. Mater. Chem. A* **2** (2014) 4225.
- [74] U. A. Paulus, A. Wokaun, G. G. Scherer, T. J. Schmidt, V. Stamenkovic, N. M. Markovic, P. N. Ross, *Electrochimica. Acta* **47** (2002) 3787.
- [75] N. Wakabayashi, M. Takeichi, H. Uchida, M. Watanabe, *J. Phys. Chem. B* **109** (2005) 5836.

[76]M. Watanabe, D. A. Tryk, M. Wakisaka, H. Yano, H. Uchida, *Electrochim. Acta* **84**
(2012) 187.

Table 1-1 Major types of fuel cells and their features [4].

TYPE	PEFC (PEMFC)	PAFC	MCFC	SOFC
Electrolyte	Proton exchange membrane	H ₃ PO ₄	Li ₂ CO ₃ /Na ₂ CO ₃ Li ₂ CO ₃ /K ₂ CO ₃	YSZ
Conducting ions	H ⁺	H ⁺	CO ₃ ²⁻	O ²⁻
Operation temp. (°C)	RT - 80	150 - 200	600 - 700	~1000
Fuel	H ₂ (CO < 100 ppm)	H ₂ (CO < 1 %)	H ₂ , CO, CH ₄	H ₂ , CO, CH ₄
Oxidant	air	air	air	air
Electrodes	Pt-Ru/C Pt/C	Pt/C	Ni NiO	Ni-YSZ cermet LaSrMnO ₃
Efficiency (%)	~40	35~45	45 - 65	45 - 65
Application	domestic, portable, vehicle, space, military	on-site	large-scale, on-site	large-scale, on-site

Table 1-2 ILs and monomers used to prepare polymer composite membranes via polymerization.

	[EMIm][BF ₄] [46]		[BPy][BF ₄] [46]		[EMIm][(FH) _{2,3} F] [47]		[EMIm][TFSI] [48]	
	Monomer	Polymer	Monomer	Polymer	Monomer	Polymer	Monomer	Polymer
Methyl methacrylate	Incomp.	N.A.	Comp.	P.S.	Comp.	P.S.	Comp.	Poly.
Acrylonitrile	Comp.	P.S.	Comp.	P.S.	–	–	Comp.	P.S.
Vinyl acetate	Comp.	Nonpoly.	Comp.	Non.	Incomp.	Nonpoly.	Comp.	Nonpoly.
Styrene	Incomp.	N.A.	Incomp.	N.A.	–	–	Comp.	P.S.
2-hydroxyethyl methacrylate	Comp.	Poly.	Comp.	Poly.	Comp.	Poly.	Comp.	P.S.
1-vinyl imidazole	–	–	–	–	Incomp.	Nonpoly.	–	–
Methyl acrylate	–	–	–	–	–	–	Comp.	Poly.
Acrylamide	–	–	–	–	–	–	Comp.	P.S.

Comp. = Compatible

Incomp. = Incompatible

Poly. = Polymerizable

P.S. = Phase separation

Nonpoly. = Nonpolymerizable

– = No report

N.A. = Not applicable

Table 1-3 IL-polymer composite membranes prepared by casting method.

(C = Concentration, T = Temperature, σ = Conductivity and P = Power density.)

Polymer	Additive	IL	IL:Polym.	Solvent	C / wt%	T / °C	time/ hr	σ / mS cm ⁻¹	P / mW cm ⁻²	Ref.
PVdF-HFP ($M_n = 130000$)	-	[BMIm][TfO]	6:4	acetone	10	RT	48	15 at 140 °C	0.6 at 140 °C	[49]
		[EMIm][TfO]						6 at 140 °C	0.12 at 140 °C	
PVdF-HFP ($M_n = 130000$)	H[TfO]	[DMPIm][TfO]	5:5	CH ₃ CN	-	-	-	0.96 at 80 °C	1.0 at 100 °C	[50]
PVdF-HFP ($M_n = 130000$)	H[TFSI]	[DMPIm][TFSI]	5:5	CH ₃ CN	-	-	-	2.74 at 130 °C	0.2 at 100 °C	[51]
PVdF-HFP ($M_n = 100000$)	H[TfO]	[DMPIm][TFSI]	7.7:2:(0.3)	-	-	130 and RT	repeated several times	10 at 100 °C	-	[52]
PVdF-HFP ($M_n = 130000$)	H[H ₂ PO ₄]	[DMEIm][H ₂ PO ₄]	5:5	CH ₃ CN	-	-	-	70 at 120 °C	-	[53]
PVdF-HFP ($M_n = 100000$)	-	[EMIm][TFSI]	6:4	MP	-	80	overnight	10 at 140 °C	-	[54]
		([Rim][TFSI])	(8:2, 4:6)							
PVdF-HFP ($M_n = 100000$)	H[TfO]	[DMPIm][TFSI]	7.7:2:(0.3)	-	-	130 and RT	repeated several times	20 at 100 °C	-	[55]
PVdF	Polyamide imide	ITSA	6:3.5:(5)	NMP	-	90	5	7.5 at 150 °C	-	[56]
PVP	-	[EMIm][BF ₄]	IL = 5, 10,... 25%	methanol	-	40	2-5 days	Increase with IL	-	[57]
PS-PEO-PS	-	[EMIm][TFSI]	9:1	CH ₂ Cl	-	70	2 days	3 at 90 °C	-	[58-59]
PS-PMMA-PS										

Table 1-3 IL-polymer composite membranes prepared by casting method. (continued)

Polymer	Additive	IL	IL:Polym.	Solvent	C / wt%	T / °C	time/ hr	s / mS cm ⁻¹	P / mW cm ⁻²	Ref.
sPAEK-6F (sPAEK)	Sulfonated	[EMIm][BF ₄]	5:5	DMAc	10	60 (vac.)	-	23 at 180 °C	-	[60]
		[(BMIm)[BF ₄], [EMIm][TfO], [BMIm][TfO)]								
sPEEK	Sulfonation 86%	[TFA][PA]	7:3	DMAc	-	RT	6	19 at 180 °C	-	[61]
PVdF	-	[TFA][PA]	6:4	DMAc	-	RT	6	3.8 at 160 °C	-	[61]
sPEEK	Sulfonation 64%	[EMIm][DEP]	5:5	NMP	-	80 (vac.)	24	3.16 at 145 °C	203 at 145 °C	[62]
sPEEK	Sulfonated	[BMIm][BF ₄]	7.5:2.5	DMAc	1.5	85	24	8.3 at 170 °C	-	[63]
		[(DMIm)[BF ₄)]						(D: 2.2)		
sPEEK	Sulfonation 64%	[BMIm][PF ₄] [(BMIm)[Cl)]	1:9	HPF ₆ (HCl)	-	110	-	2.0 at 160 °C	-	[64]
PI (in PAA form)	Imidized with IL	[RIm][BF ₄]	1:2, 1:1 ,2:1	NMP	-	80 to 240	0.5-1/ step	1-10 at 160 °C	-	[65]
sPI (in sPAA form)	Imidized with IL	[MIm][BF ₄]	5:5	NMP	-	80 to 240	0.5-1/ step	55.9 at 180 °C	-	[66]
sPI	Sulfonated, IEC = 1.51 meq g ⁻¹	[dema][TfO]	5:5	<i>m</i> -cresol	-	60	-	5 at 160 °C	100 at 80 °C	[67]
sPI	Sulfonated, IEC = 2.15 meq g ⁻¹	[dema][TfO]	7.5:2.5	<i>m</i> -cresol	-	60	-	30 at 160 °C	63 at 120 °C	[68]
sPI	Sulfonated, IEC = 2.15 meq g ⁻¹	[dema][TfO]	7.5:2.5	<i>m</i> -cresol	-	60	-	-	100 at 120 °C	[69]

Table 1-3 IL-polymer composite membranes prepared by casting method. (*continued*)

Polymer	Additive	IL	IL:Polym.	Solvent	C / wt%	T / °C	time/ hr	s / mS cm ⁻¹	P / mW cm ⁻²	Ref.
PBI	-	[dema][TfO]	8.3:1.7	DMF	-	80	24	20.73 at 140 °C 160 °C	29.64 at 140 °C (26.50 at 120 °C)	[70]
PBI	-	[HMIm][TfO]	8:2	DMAc	-	80 (vac.)	24	16 at 250 °C	-	[71]
PBI	H[H ₂ PO ₄]	[PMIm][H ₂ PO ₄]	4:1(:2)	DMSO	2	-	-	2 at 150 °C	-	[72]
PBI	H[H ₂ PO ₄] 23.6%	[EMIm][TFSI]	2:1	DMAc	-	80	12	62.6 at 160°C	300 at 170 °C	[73]

List of abbreviations

Polymer

PVdF-HFP = poly(vinylidene fluoride-co-hexafluoropropene), PVdF = poly(vinylidene fluoride), PVP = poly(vinyl pyrrolidone),

PS = poly(styrene), PEO = poly(ethylene glycol), PMMA = poly(methyl methacrylate), PAEK-6F = poly(aryl ether ketone),

PAEK = poly(aryl ether ketone), PEEK = poly(ether ether ketone), PI = poly(imide), PAA = poly(amic acid), (s = sulfonated)

Cation

BMIm = 1-butyl-3-methylimidazolium, EMIm = 1-ethyl-3-methylimidazolium, DMIm = 1-decyl-3-methylimidazolium,

HMIm = 1-hexyl-3-methylimidazolium, PMIm = 1-propyl-3-methylimidazolium, Elm = *N*-ethylimidazolium, MIm = *N*-methylimidazolium,

DMOIm = 2,3-dimethyl-1-octylimidazolium, DMPIIm = 1,2-dimethyl-3-*n*-propylimidazolium, DMEIm = 2,3-dimethyl-1-alkylimidazolium,

TFA = trifluoroacetic, dema = diethylmethylammonium

Anion

TfO = trifluoromethylsulfonate, TFSI = bis(trifluoromethylsulfonyl)imide, BF₄ = tetrafluoroborate, PF₆ = pentafluoroborate,

PA = propylamine, DEP = diethylphosphate

Ionic liquid

ITSA = isobutyramide

Solvent

MP = 4-methyl-2-pentanone, NMP = *N*-methyl pyrrolidone, DMAc = dimethylacetamide, *m*-cresol = 3-methylphenol,

DMF = dimethylformamide, DMSO = dimethylsulfoxide



Fig. 1-1 Prices of oil-based products from 1995 to 2012 [2].

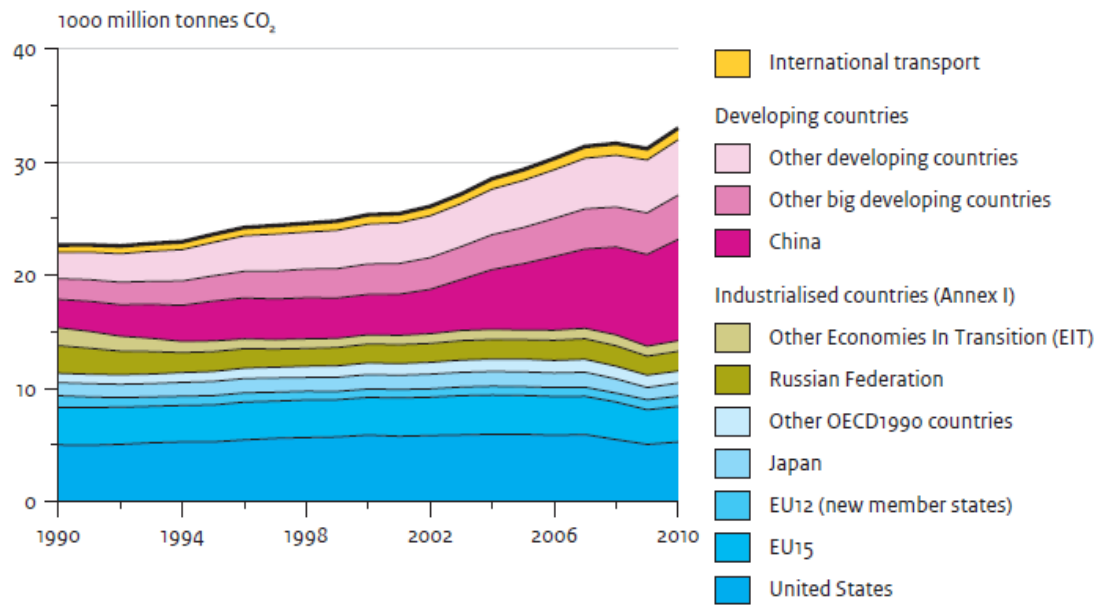


Fig. 1-2 Global CO₂ emissions from fossil fuel uses per region [3].

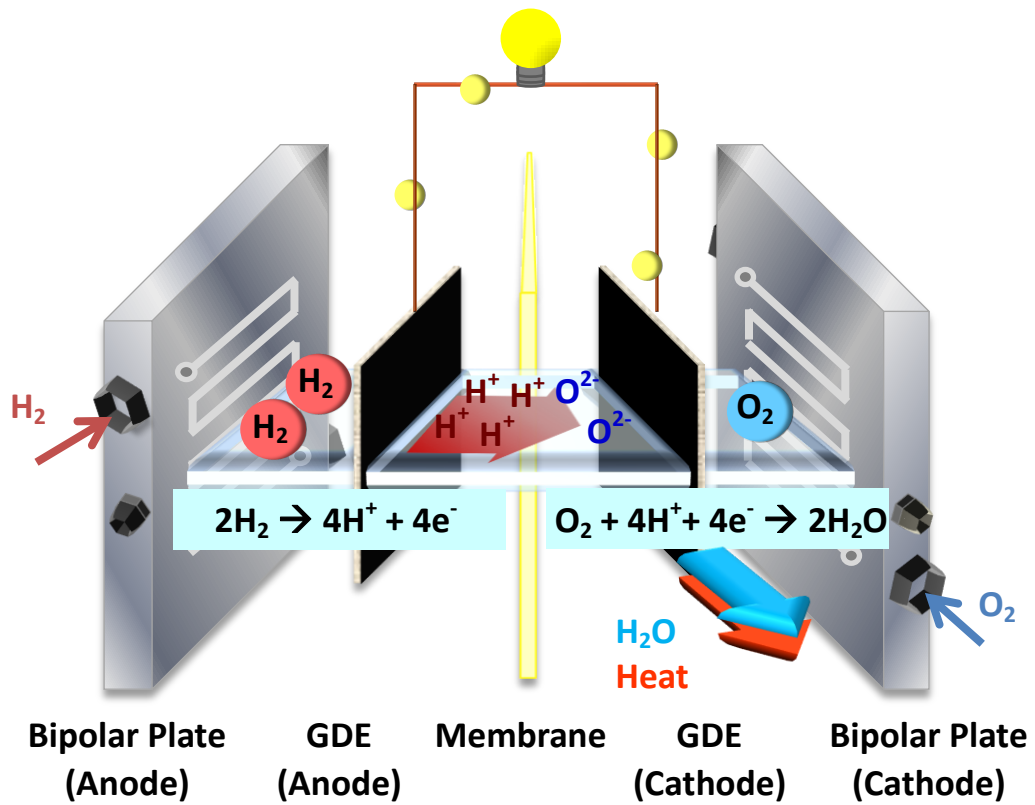


Fig. 1-3 Basic principle of PEFCs.

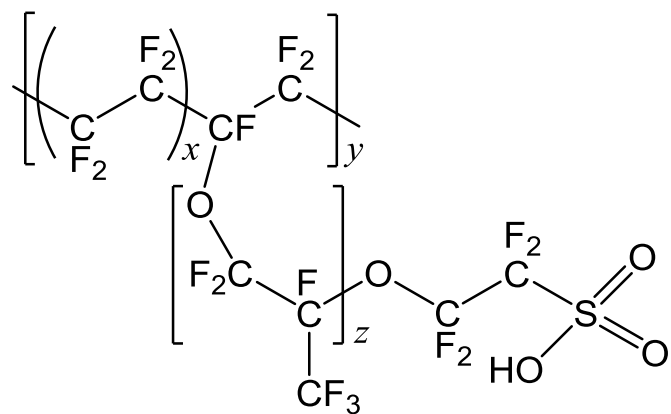


Fig. 1-4 Chemical structure of Nafion®.

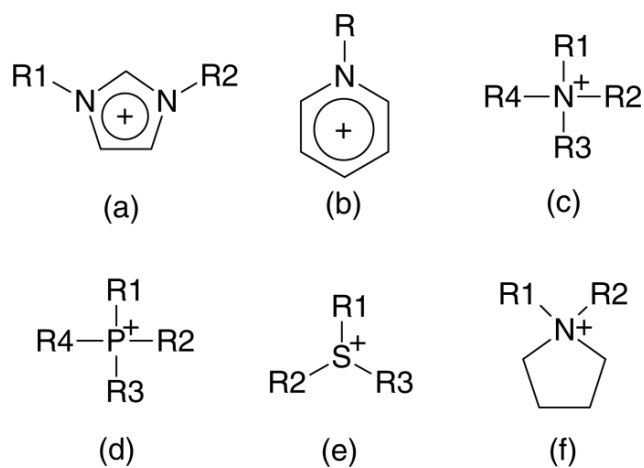


Fig. 1-5 Various types of cations for ILs; (a) dialkylimidazolium, (b) alkylpyridinium, (c) tetraalkylammonium, (d) tetraalkylphosphonium, (e) trialkylsulfonium and (f) *N,N*-dialkylpyrrolidinium.

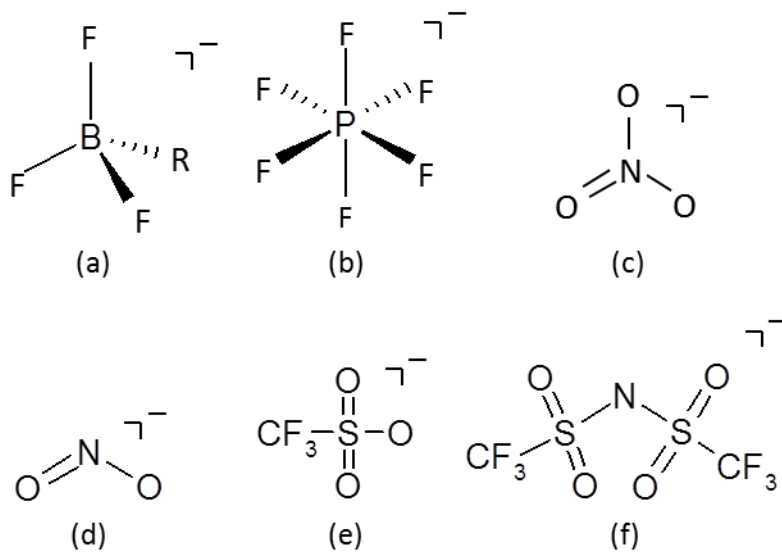


Fig. 1-6 Various types of anions for ILs; (a) perfluoroalkyltrifluoroborate, (b) hexafluorophosphate, (c) nitrate, (d) nitrite, (e) triflate and (f) bis(trifluoromethylsulfonyl)amide.

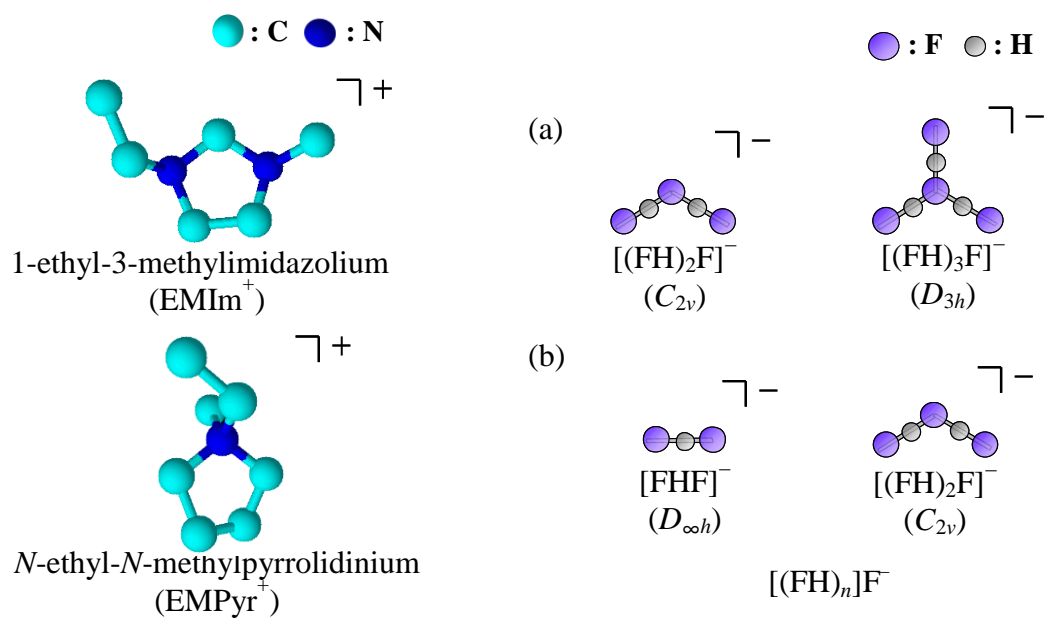


Fig. 1-7 Molecular structures of EMIm⁺ and EMPyr⁺ cations, and [(FH)_nF]⁻ anions ((a) 2 < n < 3, (b) 1 < n < 2).

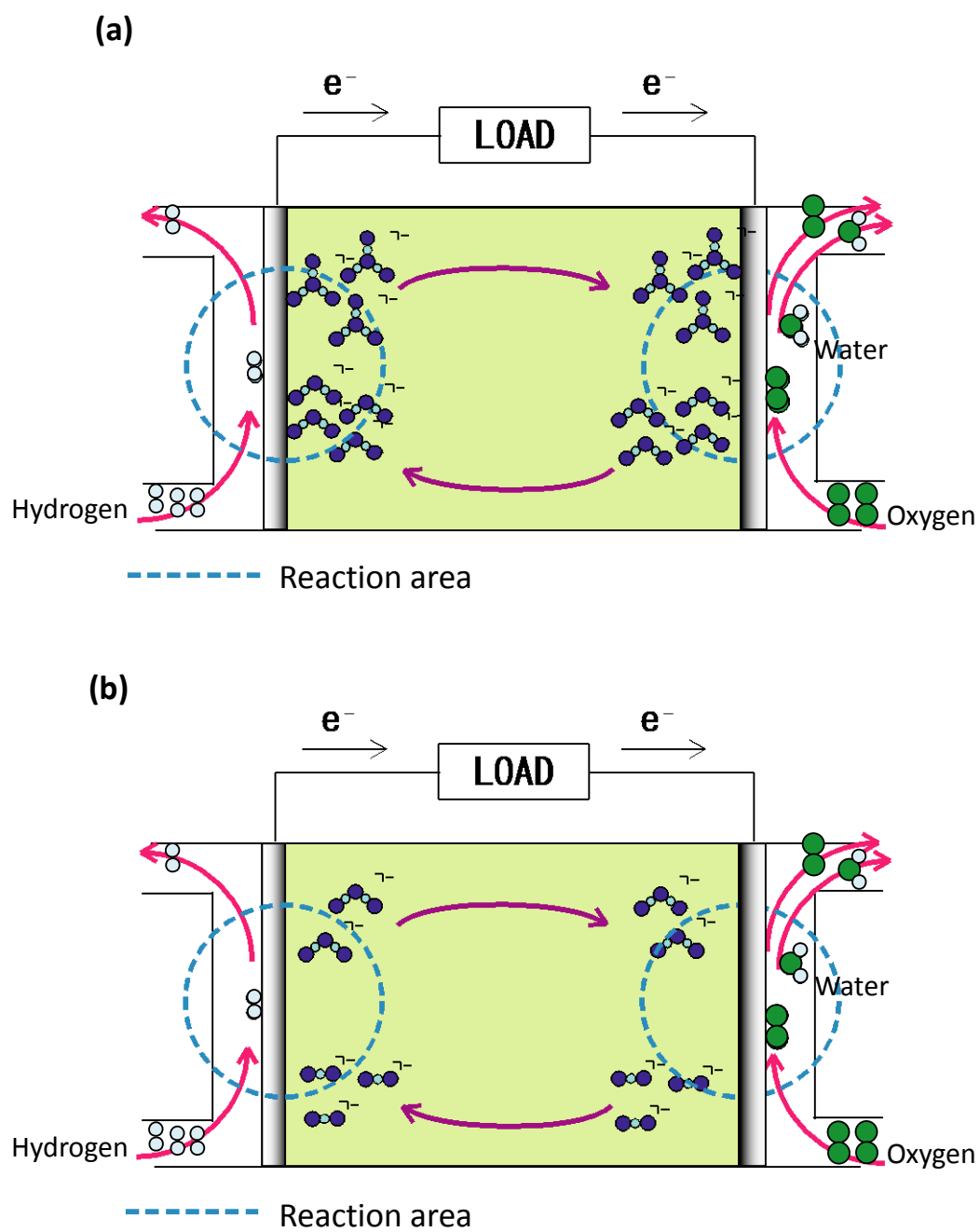
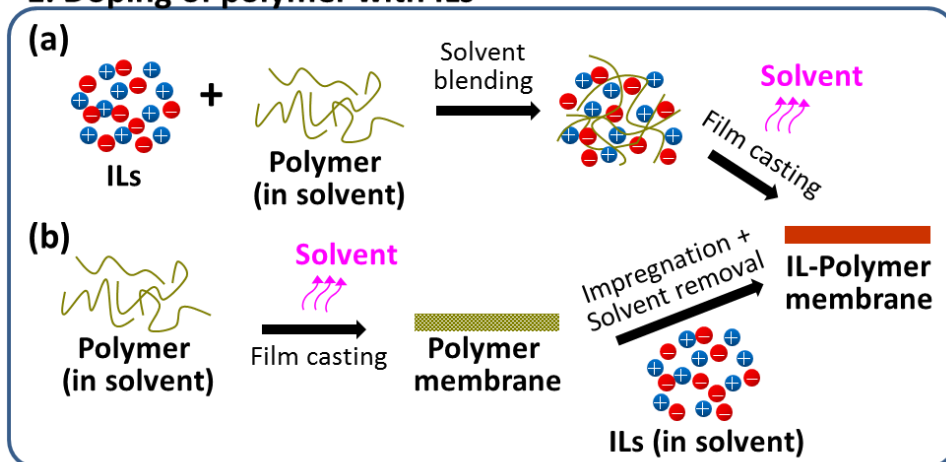
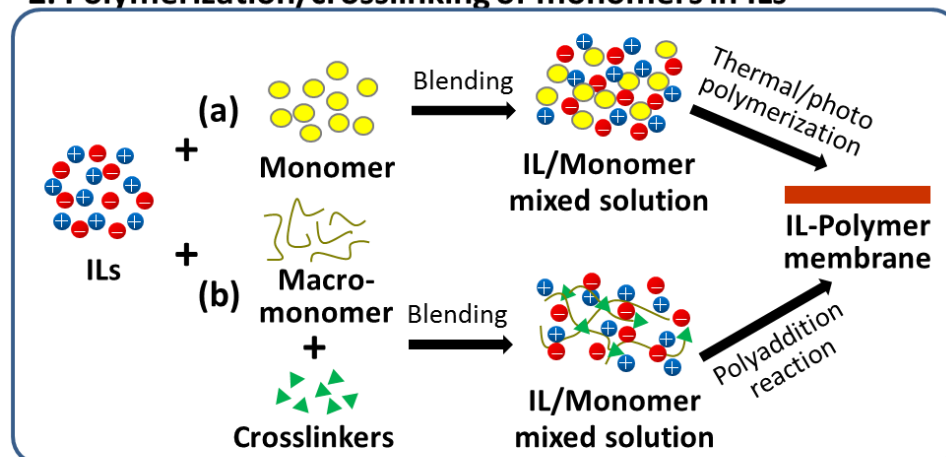


Fig. 1-8 Basic principles of FHFCs. (a) $2 < n < 3$ and (b) $1 < n < 2$.

1. Doping of polymer with ILs



2. Polymerization/crosslinking of monomers in ILs



3. Polymeric ionic liquids (PILs)

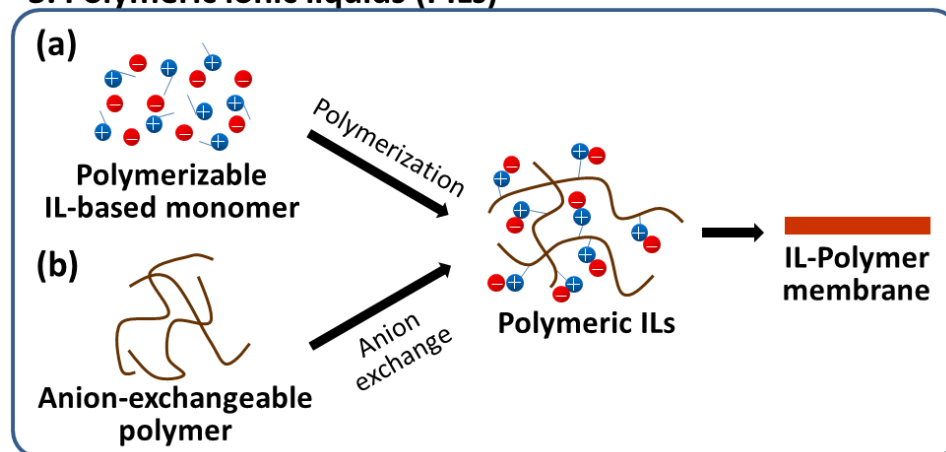


Fig. 1-9 Schematic representation of various methods for IL-based polymer electrolytes preparations.

Chapter 2

Experimental

2.1 Preparation of FHILs and apparatus

2.1.1 Preparation of FHILs

EMIm(FH)_{2.3}F and EMPyr(FH)_{2.3}F were prepared in the manner previously reported [1–2]. An excess of anhydrous HF (Morita Chemical Industry) was distilled onto EMImCl (Yoyu Lab) or EMPyrCl (Yoyu Lab) at –196 °C, followed by elimination of the unreacted HF and byproduct HCl at 25 °C. EMIm(FH)_{2.3}F and EMPyr(FH)_{2.3}F were further evacuated at 120 °C under reduced pressure (<1 Pa), which yielded EMIm(FH)_{1.3}F and EMPyr(FH)_{1.7}F, respectively [3–7]. The *n* values of 1.3 and 1.7 were determined by elemental analyses using a CHN coder and a fluoride ion selective electrode.

Trimethylsulfonium bromide (S₁₁₁Br, Tokyo Chemical Industry, >98%) was recrystallized from acetonitrile (Wako Pure Chemical Industries, >99%) by adding ethyl acetate (Wako Pure Chemical Industries, >99.5%) and dried under vacuum at 80 °C for 1 day. Triethyl-*n*-pentylphosphonium bromide (P₂₂₂₅Br, Nippon Chemical Industry) was dried under vacuum at 80 °C for 1 day. The synthesis of 5-azoniaspiro[4.4]nonane bromide (AS[4.4]Br) was completed using the following typical procedure [8]. Acetonitrile, pyrrolidine (Sigma-Aldrich, 97%), and potassium carbonate (K₂CO₃, Wako Pure Chemical Industries, >99.5%) were mixed, followed by addition of 1,4-dibromobutane (Sigma-Aldrich, 97%) with cooling at 0 °C. The flask was connected to reflux apparatus and stirred at 60 °C for 6 hours. First filtration of the

contents in the flask removed most of the excess K_2CO_3 . Addition of ethyl acetate to the filtrate then resulted in the recrystallization of AS[4.4]Br. After drying at 60 °C for 1 day, the remaining K_2CO_3 was completely removed by passing the solution through a column filled with activated alumina. Recrystallization and washing were repeated several times, followed by drying at 80 °C.

$S_{111}(FH)_{1.9}F$, $P_{2225}(FH)_{2.1}F$, and $AS[4.4](FH)_{2.0}F$ were synthesized by metathesis of the bromides and anhydrous HF (Daikin Industries, >99%), which was dried over K_2NiF_6 (Ozark Mahoning), in the same manner as $EMIm(FH)_{2.3}F$ and $EMPyr(FH)_{2.3}F$ [8–10]. The addition and elimination of anhydrous HF were repeated several times in order to ensure the complete elimination of the bromide in the form of HBr. Since the evolution of HBr was sometimes slow, the pressure inside the closed vessel was constantly monitored in order to ensure the completion of reaction. $AgNO_3$ solution was used to test for the presence of residual Br^- . The product was titrated until there was no further precipitation of AgBr.

2.1.2 Preparation of FHIL-polymer composite membranes

$EMPyr(FH)_{1.7}F$ -HEMA composite membranes were prepared by polymerizing the mixed solution of $EMPyr(FH)_{1.7}F$ ionic liquid and HEMA polymer with a porous supporting material at 70 °C for 12 hours. The preparation procedure will be explained in details in chapter 3. The porous supporting material used in chapter 3 was PTFE while the one used in chapter 4 was PI. The composite membranes of $EMPyr(FH)_{1.7}F$ and PVdF-HFP were prepared without porous supporting material by casting method, as mentioned in section 1.5.3 of chapter 1. The preparation procedure will be thoroughly explained in chapter 5.

2.1.3 Preparation of Pt alloys

Pt-alloys were prepared by a radio frequency magnetron sputtering deposition system (SVC-700 RF 2, SANYU). A Pt disk substrate (5 mm in diameter, 5 mm in thickness), were polished with emery paper and buffing compound. Then, it was set on the stage together with a Si plate in the chamber. The chamber was first evacuated to 1.0×10^{-3} Pa. Then, Ar gas (Kyoto Teisan, > 99.999%) was introduced into the chamber up to the pressure of 5 Pa. The surface of the substrate was etched using argon ion plasma to remove the surface oxide layer for 30 min at room temperature. A Pt, Pt-Fe, Pt-Co, or Pt-Ni layer was deposited by sputtering deposition using Pt, PtFe, PtCo, or PtNi targets (Furuya Metal, purity 3 N), respectively, for 20 min at 300 °C.

2.1.4 Glove box

Reagents were handled in a glove box filled with argon (purity > 99.998 %, Kyoto Teisan) equipped with a continuous gas-refining instrument (DBO-1KH, Miwa). The concentration of water in the atmosphere was always monitored and kept at less than -70 °C in a dew point. Volatile reagents were handled in a glove bag filled with argon.

2.1.5 Vacuum line

Fig. 2-1 shows a schematic illustration of a vacuum line used for elimination of HF and contaminated water. Valves, joints and tubes which construct the line, are made of SUS-316 stainless steel. The pressure in the line was monitored by a Bourdon pressure gauge and a Pirani gauge. Gases in the line were evacuated by a rotary pump

through a chemical trap containing soda lime connected to a cold trap in series. The lowest pressure achieved in this system was below 1 Pa.

2.2 Measurements of physical and electrochemical properties

2.2.1 Ionic conductivities of FHILs

Ionic conductivities of FHILs were measured using a T-shaped cell equipped with platinum disk electrodes as shown in Fig. 2-2. The cell constant was determined with a KCl standard solution at 25 °C. The measurement was conducted by using a.c. impedance method that will be described in the later section. Change of the cell constant with temperature was judged to be negligible for the temperature range of –40 to 80 °C.

2.2.2 Ionic conductivities of FHIL-polymer composite membranes

Ionic conductivity of the composite membranes was measured using four-point probe a.c. impedance method with a cell shown in Fig. 2-3. The cell consists of 2 platinum plates (1 x 0.5 cm²) placed with aperture of 4 cm to feed a.c. current to the sample and 4 platinum needles (0.3 mm ϕ) placed apart by 0.5 cm with each other to measure the potential drops along the film near the center. The atmosphere was dry nitrogen. The conductivity was measured in longitudinal direction. In the calculation of conductivity, the following equation was used.

$$\sigma = l/RS \quad (2-1)$$

where σ , l , R and S denote the ionic conductivity, distance between the reference electrodes, the measured resistance of the membrane, and the cross-sectional area of the membrane, respectively. Before the measurement, water absorbed into the composite membrane during the set up was removed by maintaining the cell at 80 °C for more than

1 h under flowing dry nitrogen. The ionic conductivity was measured from 120 °C to –40 °C in a temperature-controlled chamber (SU-241, Espec).

2.2.3 a.c. impedance method for ionic conductivity measurement

A Solartron 1260 frequency response analyzer (AMETEK) combined with a Solartron 1286 electrochemical interface (AMETEK) was used to provide a.c. signal and analyze the impedance of the membrane. The amplitude of the a.c. signal was 10 mV and the frequency range was from 100 kHz to 1 Hz. The ionic conductivities were calculated from the bulk impedances at zero-phase angle.

2.2.4 Thermogravimetry (TG)

Thermal gravimetric analysis (TGA) was performed by using a differential thermogravimetric analyzer (DTG-60/60H, Shimadzu) to investigate the thermal decomposition behavior of both FHILs and their composite membranes with polymers. Platinum cells, used in this study, were washed with acetone just before the measurement and dried in the equipment at 600 °C for more than 30 min. The measurement was performed under the flow of dry nitrogen gas (purity 99.99 %, 50 mL min⁻¹, Kyoto Teisan). The cells (a blank and a sample-filled ones) were heated to 80 °C and kept at this temperature for 3 h to remove the excess water absorbed into the samples. After the temperature was lowered to 25 °C, the cells were gradually heated to 600 °C with the scan rate of 1 °C min⁻¹.

2.2.5 Differential scanning calorimetry (DSC)

Differential scanning calorimeter (DSC-60, Shimadzu) was used to determine

phase transition behavior and transition temperature of FHILs and their composite membranes. Stainless cell was used because of its good chemical stability with FHILs. The measurement was performed under the flow of dry nitrogen gas (200 mL min⁻¹).

2.2.6 X-ray photoelectron spectroscopy

X-ray photoelectron spectroscopy (XPS) analysis was performed by JPS-9010 MC (JEOL) with MgK α radiation. The samples were fixed on carbon sheets. Before measurement, they were etched for 20 s. The obtained peaks were corrected by C1s peak of 248.6 eV.

2.3 Fuel cell test

2.3.1 Fabrication of membrane-electrode assembly (MEA)

Fig. 2-4 shows schematic drawing of the single cell used in this study. First, the membrane electrode assembly (MEA) was prepared by placing the composite membrane between 2 gas diffusion electrodes (GDEs, 1.0 mg Pt cm⁻², ionomer free, KM Lab). The MEA was then fabricated with gaskets and bipolar plates (ElectroChem). The compressing pressure was below 0.1 MPa; checked by pressure sensitive papers.

2.3.2 Single cell test under nonhumidified conditions

Single cell test was performed using Solartron 1286 electrochemical interface in a temperature control chamber (Espec) at 25–120 °C under nonhumidified conditions. The measurement was carried out using two-electrode method. To evaluate the cell performance, potentiostatic and linear sweep voltammetry were conducted. Dry hydrogen (purity >99.999 %) was supplied from a hydrogen generator (HORIBA

STEC) and dry oxygen (purity >99.9999 %, Kyoto Teisan) was supplied from a cylinder at the flow rates of 10 ml min^{-1} for 1 cm^2 single cell and 20 ml min^{-1} for 5 cm^2 single cell.

2.3.3 *In-situ* a.c. impedance analysis

During the single cell test, *in-situ* electrochemical impedance spectroscopy was also studied by a.c. impedance method using a Solartron 1286 electrochemical interface combined with a Solartron 1260 frequency response analyzer (AMETEK). An a.c. potential of 10 mV, as an excitation signal, was applied to the single cell under a constant cell voltage of 0.8, 0.6 or 0.4 V. The frequency range was from 20 kHz to 0.02 Hz. The plot of real and imaginary parts of the impedance with varied frequency, called Nyquist plot, was used to express the impedance profile. The impedances at *x*-intercept points indicate the resistances in the single cell under that operating condition. The approximated values of resistances, Ohmic resistance, electrochemical reaction resistance and mass transfer resistance, were determined by fitting the Nyquist plot with an equivalent circuit as shown in Fig. 2-5. The internal resistances of a single cell are represented by the values of resistors in equivalent circuit. Ohmic resistance is denoted by R_0 while electrochemical reaction resistance at anode and cathode are denoted by R_1 and R_2 , respectively. R_3 indicates mass transfer resistance. *CPE* denotes the constant phase element which is a non-ideal capacitance used to model the behavior of a double layer capacitor.

2.3.4 Cross-sectional SEM observation

MEA samples from before and after the single cell test were cut by a design

knife and embedded into a resin block using a resin mounting kit (20-3570, VariDur[®]). The sample block was then repeatedly polished with emery papers (No. 300, 600, 1200, 2000 and 3000, successively) on a rotating stage (100 rpm) to expose the cross-sectional area. The exposed surface was coated with gold using ion-sputtering equipment (E-1010, Hitachi) prior to observation with a scanning electron microscope (SEM, VE-8800, Keyence). The atomic compositions of specific areas were analyzed by EDX (EDAX Genesis APEX2, AMETEK).

2.4 Electrochemical measurements using RDE and RRDE methods

2.4.1 A three-electrode cell

A rotating electrode control system (Pine Research Instrumentation) combined with a three-electrode PTFE cell shown in Fig. 2-6 were used for the electrochemical measurements in chapter 7. Either a rotating disk electrode (RDE, Pine Research Instrumentation) or a rotating ring-disk electrode (RRDE, Pine Research Instrumentation) was used as the working electrode. The counter electrode was a Pt wire while the reference electrode was a reversible hydrogen electrode (RHE) made of Pt-black. About 20–30 g of each FHIL was utilized as an electrolyte. Electrochemical measurements were conducted with the aid of a potentio/galvanostat (IVIUMSTAT, Ivium Technologies). Dry hydrogen (purity >99.999%) was supplied from a hydrogen generator (HORIBA STEC) at a flow rate of 10 mL min⁻¹ and dry oxygen (Kyoto Teisan, >99.999%,) was supplied from a cylinder at the same flow rate. Prior to the electrochemical measurement, oxygen was bubbled into the cell for 2 hours in order to saturate the electrolyte.

2.4.2 RDE method

RDE method was used, in chapter 6, to evaluate the ORR activities (eg. kinetically limited current density (j_k)), and solubility (C) and diffusion coefficient (D) of oxygen at 25 °C for each FHIL. In chapter 7, it was used to estimate the activities of the Pt and Pt-alloys in a FHIL from 25 to 60 °C. An RDE consisting of a Pt disk 5.0 mm in diameter was used as the working electrode. The rotation speed was set at 100, 144, 225, 400 and 625 rpm, respectively.

2.4.2 RRDE method

RRDE method was used, in chapter 6, to estimate the yield of H_2O_2 ($X_{H_2O_2}$) at 25 °C for each FHIL. An RRDE consisting of a Pt disk 5.0 mm in diameter surrounded by a Pt ring with an internal diameter of 5.5 mm and an external diameter of 8.0 mm was used as the working electrode. Steady-state disk currents at 0.2 V vs. RHE and steady-state ring currents at 1.5 V vs. RHE were measured at the rotation speed of 100 rpm.

References

- [1] R. Hagiwara, T. Hirashige, T. Tsuda, Y. Ito, *J. Electrochem. Soc.* **149** (2002) D1.
- [2] K. Matsumoto, R. Hagiwara, Y. Ito, *Electrochem. Solid-State Lett.* **7** (2004) E41
- [3] R. Hagiwara, T. Nohira, K. Matsumoto, Y. Tamba, *Electrochem. Solid-State Lett.* **8** (2005) A231.
- [4] J. S. Lee, T. Nohira, R. Hagiwara, *J. Power Sources* **171** (2007) 535.
- [5] T. Hayashida, *Master thesis of Kyoto University* (2009).
- [6] Y. Tani, T. Nohira, T. Enomoto, K. Matsumoto, R. Hagiwara, *Electrochim. Acta* **56** (2011) 3852.
- [7] P. Kiatkittikul, T. Nohira, R. Hagiwara, *J. Power Sources* **220** (2012) 10.
- [8] R. Taniki, K. Matsumoto, R. Hagiwara, *Chem. Lett.* **42** (2013) 1469.
- [9] T. Enomoto, S. Kanematsu, K. Tsunashima, K. Matsumoto, R. Hagiwara, *Phys. Chem. Chem. Phys.* **13** (2011) 12536.
- [10] R. Taniki, K. Matsumoto, R. Hagiwara, *Electrochem. Solid-State Lett.* **15** (2012) F13.

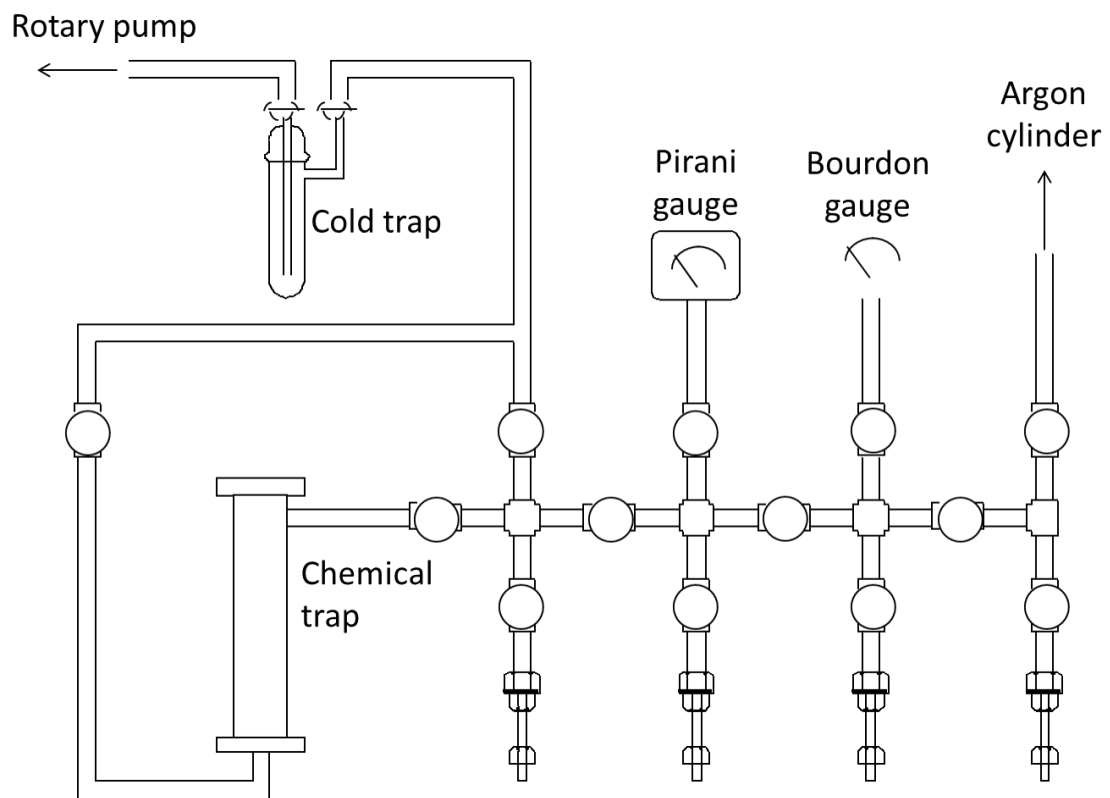


Fig. 2-1 Vacuum line.

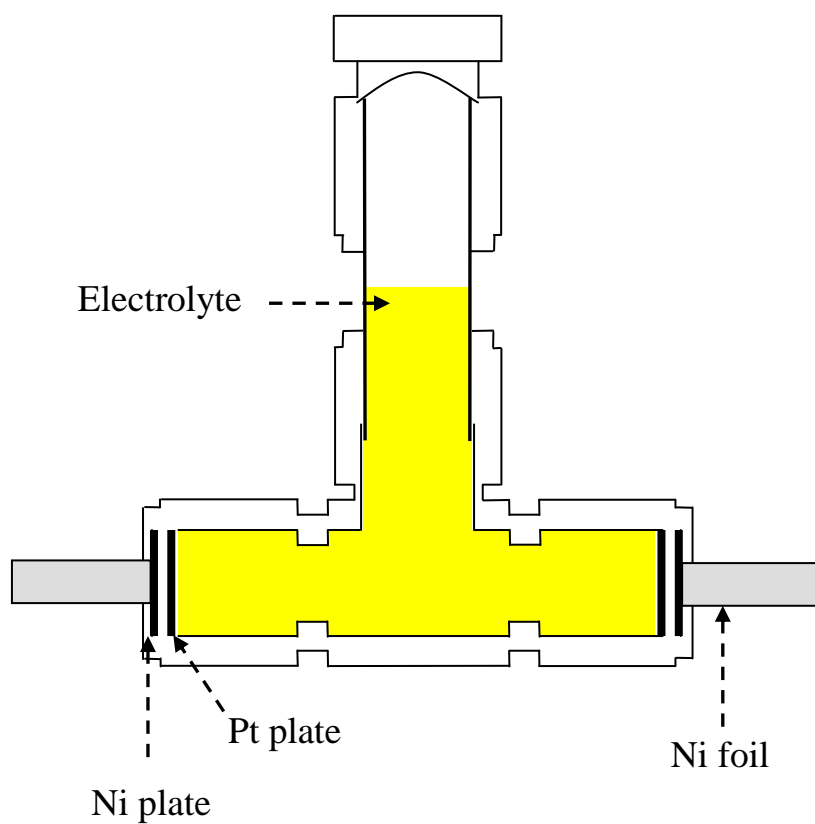


Fig. 2-2 Schematic drawing of the T-shaped cell

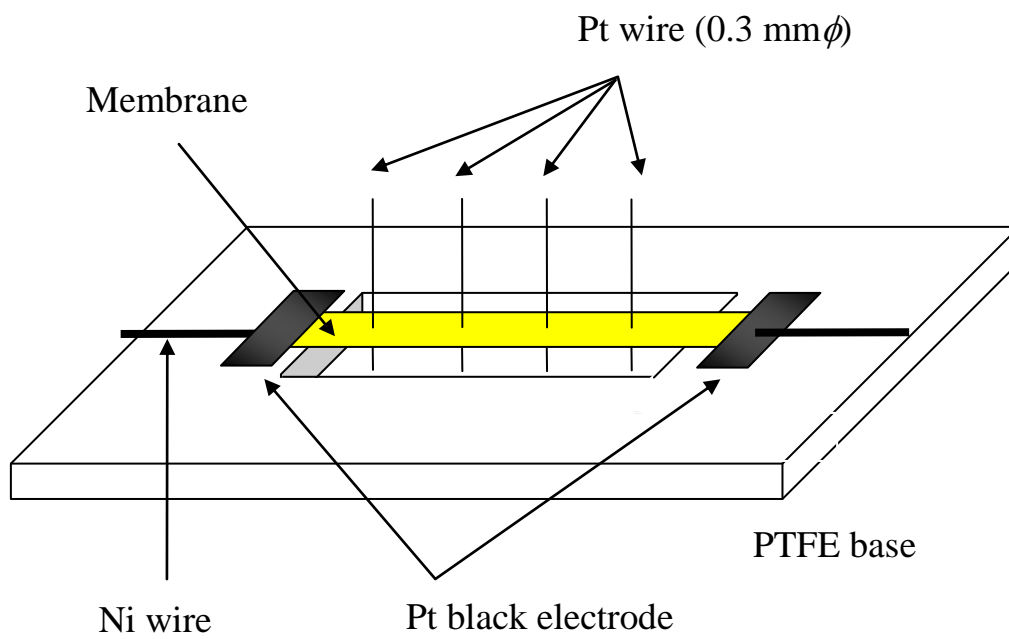


Fig. 2-3 Schematic drawing of the four-point probe cell.

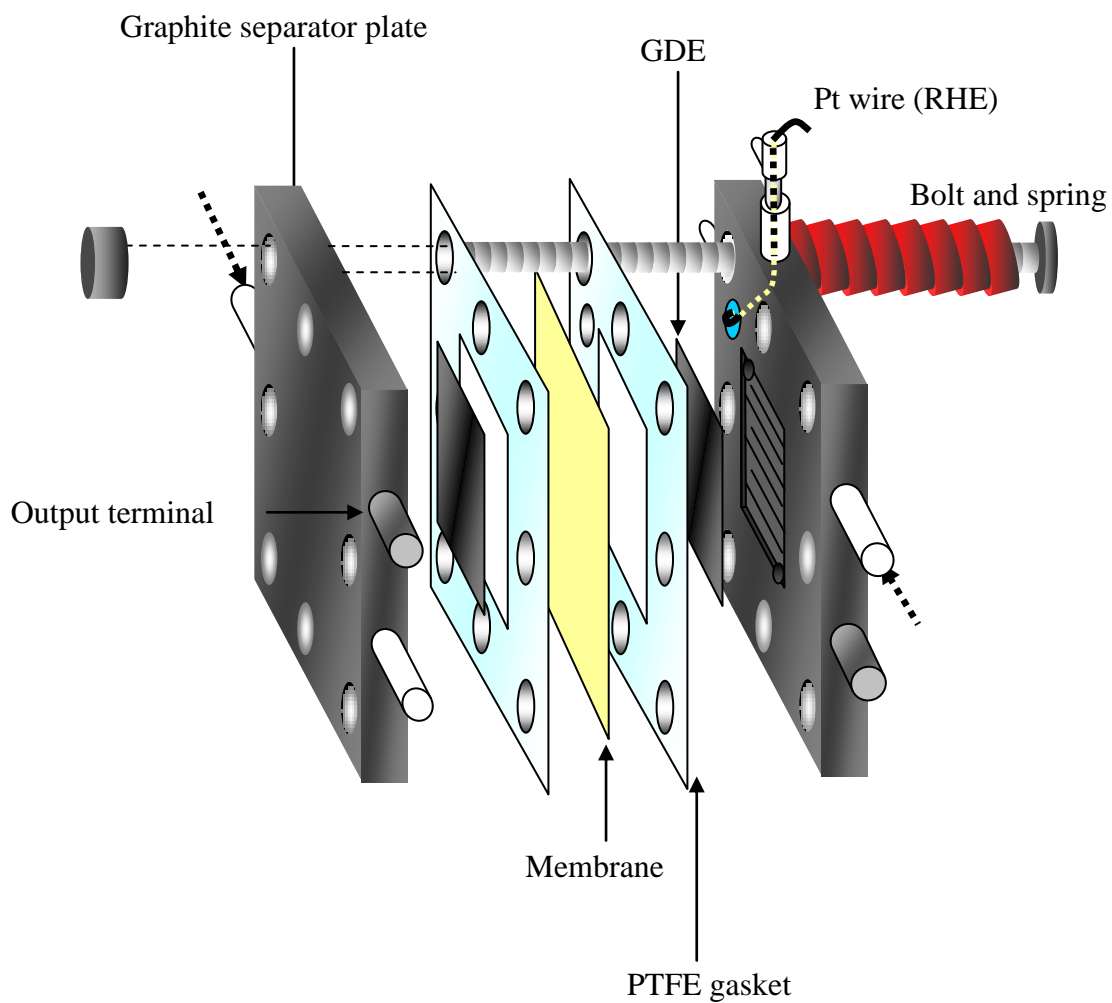


Fig. 2-4 Schematic drawing of the single cell.

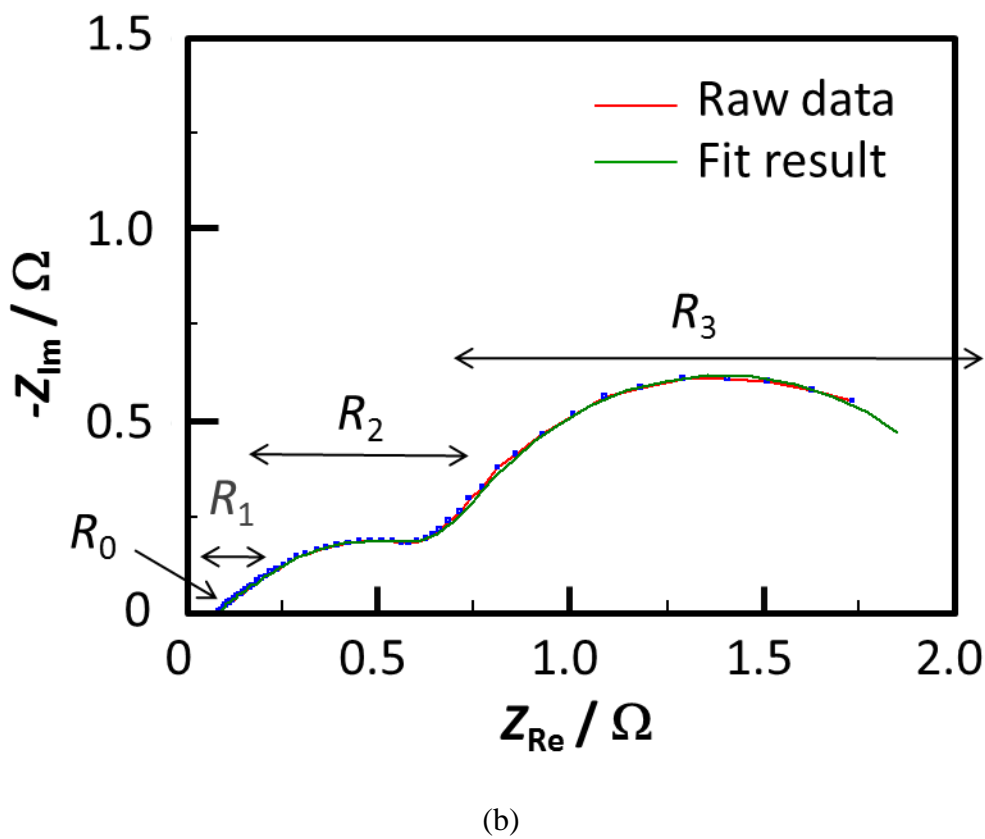
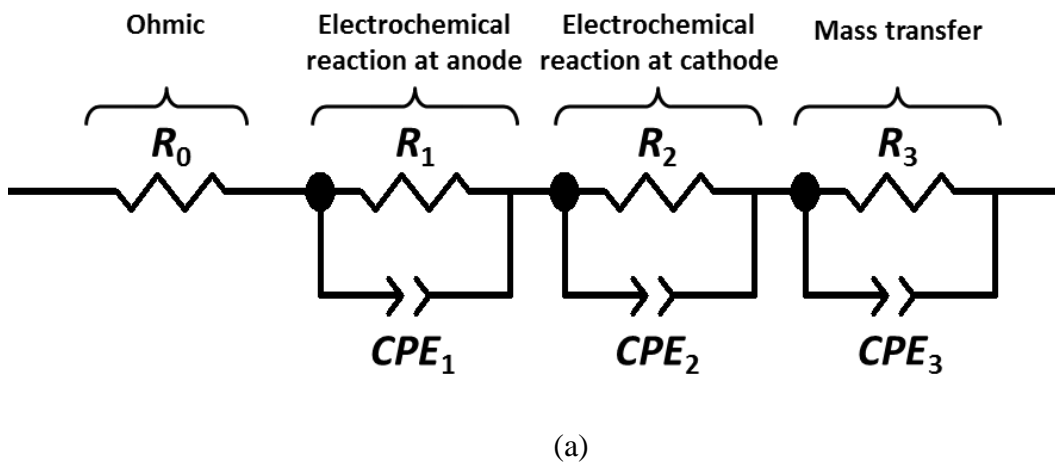


Fig. 2-5 (a) Equivalent circuit and (b) Nyquist plot of the measured impedance and fitting result. R_0 : Ohmic resistance, R_1 : Electrochemical reaction resistance at anode, R_2 : Electrochemical reaction resistance at cathode and R_3 : Mass transfer resistance.

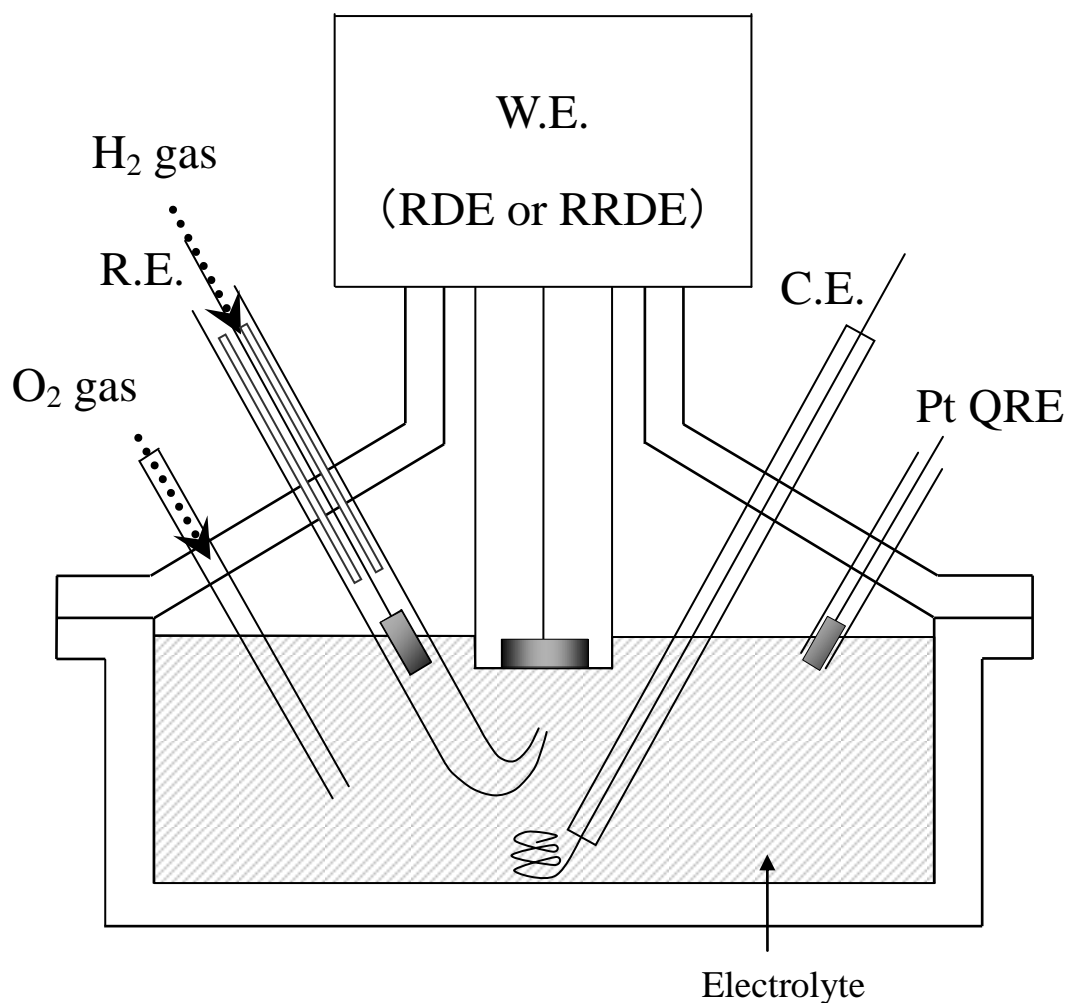


Fig. 2-6 Apparatus of the three-electrode PTFE cell used for RDE and RRDE measurements in FHILs.

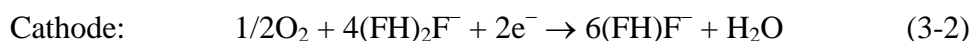
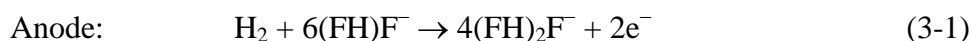
Chapter 3

Preparation, characterization and fuel cell performance of EMPyr(FH)_{1.7}F–HEMA composite membranes using a PTFE membrane support

3.1 Introduction

In the recent studies, *N*-ethyl-*N*-methylpyrrolidinium fluorohydrogenate, EMPyr(FH)_{1.7}F, whose structure is shown in Fig. 3-1, was found to exhibit higher activity for the oxygen reduction reaction (ORR) on a Pt electrode [1]. It was also revealed that EMPyr(FH)_{1.7}F possesses adequate oxygen permeability, with a crossover current as low as 0.143 mA cm⁻² in the case of electrolyte thickness of 177.8 μm [2].

In this chapter, composite membranes of EMPyr(FH)_{1.7}F ionic liquid and 2-hydroxyethylmethacrylate (HEMA) polymer were prepared using PTFE filter as a porous supporting material. Their thermal and electrochemical properties were investigated by means of TG, DSC and ionic conductivity measurement. Using the composite membrane, the single cell performance was studied under nonhumidified conditions. It should be noted that the anode, cathode, and total reactions for the FHFC in this study (using EMPyr(FH)_{1.7}F as the electrolyte) are expressed as follows:



where (FH)F⁻ and (FH)₂F⁻ anions are involved in the reactions.

3.2 Experimental

3.2.1 Preparation of EMPyr(FH)_{1.7}F–HEMA composite membranes using a PTFE membrane support

EMPy_r(FH)_{2.3}F was prepared using the method reported previously [3]. To prepare EMPyr(FH)_{1.7}F, which has a negligible vapor pressure up to 393 K, EMPyr(FH)_{2.3}F was evacuated using a rotary pump through a chemical trap for four days and then directly through a cold trap for two days at 393 K under reduced pressure (<1 Pa). The *n* value of 1.7 was confirmed by elemental analysis of hydrogen, carbon, nitrogen, and fluorine using a CHN coder and a fluoride ion-selective electrode.

The mixed solutions of EMPyr(FH)_{1.7}F and the HEMA monomer (Wako) were prepared in the molar ratios of 7:3, 8:2, and 9:1 under an argon atmosphere. A small amount (1 mol% of HEMA) of azobisisobutyronitrile (AIBN, Wako) was added as a radical initiator. Membrane filters (OmniporeTM, Millipore, thickness: 65 μm, average pore diameter: 0.45 μm, porosity: 80%), which were used as porous supporting materials, were immersed in the mixtures. Each membrane filter was sandwiched between two PTFE sheets and then polymerized in a vacuum oven filled with argon gas at 343 K for 12 h.

3.2.2 Characterizations of composite membranes

A differential thermogravimetric analyzer (DTG-60/60H, Shimadzu) was used to investigate the thermal stability of the EMPyr(FH)_{1.7}F ionic liquid and the composite membranes from 323 K to 873 K at a scanning rate of 1 K min⁻¹ under nitrogen atmosphere. Phase-transition behavior was examined by means of a differential scanning calorimeter (DSC-60, Shimadzu) between 123 K and 423 K at a scanning rate

of 10 K min^{-1} under nitrogen atmosphere. To measure the ionic conductivity of the EMPyr(FH)_{1.7}F ionic liquid, a T-shaped cell with two Pt rods at a fixed distance was used. The cell constant was determined using a 0.1 M KCl standard solution. To measure the ionic conductivity of the composite membranes, the four-point probe method was used. The measurement was carried out by the ac impedance method using a Solartron 1286 electrochemical interface combined with a Solartron 1260 frequency response analyzer (AMETEK) from 233 K to 393 K under nitrogen atmosphere.

3.2.3 MEA fabrication and single cell test

The membrane–electrode assembly (MEA) was prepared by placing the composite membrane between two gas diffusion electrodes (GDEs, $1.0 \text{ mg Pt cm}^{-2}$, ionomer-free, KM Lab) with a geometric surface area of 5 cm^2 . After fabricating the composite membrane into a single cell with fuel-cell hardware (EFC-05-02-H2R, 5 cm^2 , ElectroChem), the single cell test was performed using a Solartron 1286 electrochemical interface in a temperature-controlled chamber (Espec) from 298 K to 393 K under nonhumidified conditions. Anhydrous H_2 (99.999 %) was supplied from a hydrogen generator (HORIBA STEC) and O_2 was supplied from a cylinder (99.9999 %). The gas flow rates of H_2 and O_2 were 20 mL min^{-1} .

3.2.4 Cross-sectional SEM observation

The samples of MEAs before and after the single cell test were cross-sectioned by a knife and embedded with resin into a block. The sample block was then polished with emery paper to expose the cross section. The surface was coated with Au by ion-sputtering (E-1010, Hitachi) prior to observation by scanning electron microscope

(SEM, VE-8800, Keyence).

3.3 Results and Discussion

3.3.1 Thermal stability and phase transition behavior

Fig. 3-2 shows TGA curves for the EMPyr(FH)_{1.7}F ionic liquid and the EMPyr(FH)_{1.7}F–HEMA (9:1, 8:2, and 7:3 in molar ratio) composite membranes. For EMPyr(FH)_{1.7}F, decomposition is observed from approximately 453 K. In the case of the EMPyr(FH)_{1.7}F–HEMA composite membranes, the initial weight loss also starts at 453 K. The value of the initial weight loss cannot be explained only by the decomposition of EMPyr(FH)_{1.7}F because decomposition of HEMA also occurs. These two decompositions are indistinguishable because they proceed in almost the same temperature range. The final weight loss at 753 K corresponds to the decomposition of the membrane (PTFE) filter. These results indicate that the composite membranes are thermally stable up to 453 K, regardless of HEMA content.

Phase-transition behaviors were investigated by means of DSC, as shown in Fig. 3-3. The melting point was found to be 253 K for the EMPyr(FH)_{1.7}F ionic liquid and 203 K for the EMPyr(FH)_{1.7}F–HEMA (9:1) composite membrane. However, a melting point was not observed for the EMPyr(FH)_{1.7}F–HEMA (8:2) composite membrane. The decrease in the melting point suggests an interaction between the EMPyr(FH)_{1.7}F ionic liquid and the HEMA polymer. As expected, the interaction becomes stronger with an increase in the HEMA content.

3.3.2 Ionic conductivity

The ionic conductivities were measured from 233 K to 393 K under

nonhumidified conditions. Fig. 3-4 shows Arrhenius plots of ionic conductivities for the EMPyr(FH)_{1.7}F ionic liquid and the EMPyr(FH)_{1.7}F-HEMA (9:1, 8:2, and 7:3) composite membranes. The ionic conductivity increases with an increase in the FHIL content. For the EMPyr(FH)_{1.7}F ionic liquid, the ionic conductivities were 46.7 and 204.7 mS cm⁻¹ at 293 K and 393 K, respectively. A sudden drop in the ionic conductivity occurred at 253 K, which is explained by the solidification of the EMPyr(FH)_{1.7}F ionic liquid, whose melting point is 253 K. However, this drop was not observed in any of the EMPyr(FH)_{1.7}F-HEMA composite membranes, whose melting points are significantly below the measuring range of ionic conductivity. For the EMPyr(FH)_{1.7}F-HEMA (9:1) composite membrane, the ionic conductivities were 8.7 and 81.9 mS cm⁻¹ at 298 K and 393 K, respectively. These values are very high compared with previously reported values for composite membranes using similar FHILs [4] and other ionic liquid-based polymer membranes [5-11].

3.3.3 Single cell performance under nonhumidified conditions

A single cell using the EMPyr(FH)_{1.7}F-HEMA (9:1) composite membrane was operated at 298, 323, 353, and 393 K under nonhumidified condition. Fig. 3-5 shows the current density-voltage (*i-v*) and current density-power density (*i-p*) curves. From 298 K to 323 K, single cell performance improves significantly owing to the increase in the electrochemical reaction rate by the elevation of the operating temperature. A maximum power density of 32 mW cm⁻² is observed at 323 K. However, a small decrease in the power density is observed when the temperature is increased to 353 K. Furthermore, single cell performance is significantly impaired at 393 K.

Fig. 3-6 shows SEM images of the cross sections of MEAs using the

EMPy_r(FH)_{1.7}F–HEMA (9:1) composite membrane. Before the single cell test, three layers consisting of the membrane, the catalyst layer, and the gas diffusion layer are clearly separated but in good contact with each other. The catalyst Pt/C clusters are also uniformly distributed. However, after the single cell test at 298–353 K, the porosity in the catalyst layer decreases, which restricts the gas transport channels. This deterioration became more obvious for the MEA after the single cell test at 393 K. These results explain the temperature dependence of the single cell performance as follows. At a high temperature, the composite electrolyte in the membrane softens, penetrating into the GDEs and partially plugging the pass in the gas diffusion layer. The deformation of the membrane–electrode layer obstructs the gas supply to the three-phase reaction zone and results in an increase in the mass-transfer resistance. For these reasons, development of a composite membrane that possesses high mechanical strength even at elevated temperatures is necessary.

To improve the single cell performance, optimization of the three-phase reaction zone is necessary. This can be accomplished by the introduction of an ionomer into the catalyst layer. The development of mechanically stronger membranes even at 393 K and the introduction of ionomers are now underway.

3.4 Conclusion

Composite membranes consisting of EMPy_r(FH)_{1.7}F and HEMA polymer were prepared and investigated for nonhumidified fuel cells. The composite membranes showed sufficient thermal stability for operation at elevated temperatures up to 423 K. The ionic conductivities of the EMPy_r(FH)_{1.7}F–HEMA (9:1) composite membrane were 8.7 and 81.9 mS cm⁻¹ at 293 K and 393 K, respectively, values that are higher than

those for other ionic liquid-based polymer membranes. In the single-cell tests, a maximum power density of 32 mW cm^{-2} was observed at 323 K under nonhumidified conditions. The deterioration of the single cell performance at 353 K is explained by the obstruction of gas flow in GDEs caused by the softening of the composite membrane at elevated temperatures.

References

- [1] T. Nohira, R. Hagiwara, M. Yamagata, K. Ogasawara, T. Hayashida, *Abstracts of the 10th Meeting on Materials for Chemical Batteries in Japan*, 2008, p. 81.
- [2] Y. Tani, T. Nohira, T. Enomoto, K. Matsumoto, R. Hagiwara, *J. Electrochim. Acta* **56** (2011) 3852.
- [3] R. Hagiwara, K. Matsumoto, Y. Nakamori, T. Tsuda, Y. Ito, H. Matsumoto, K. Momota, *J. Electrochem. Soc.* **150** (2003) D195.
- [4] J. S. Lee, T. Nohira, R. Hagiwara, *J. Power Sources* **171** (2007) 535.
- [5] S. Y. Lee, A. Ogawa, M. Kanno, H. Nakamoto, T. Yasuda, M. Watanabe, *J. Am. Chem. Soc.* **132** (2010) 9764.
- [6] S. Y. Lee, T. Yasuda, M. Watanabe, *J. Power Sources* **195** (2010) 5909.
- [7] S. S. Sekhon, P. Krishnan, B. Singh, K. Yamada, C.S. Kim, *Electrochim. Acta* **52** (2006) 1639.
- [8] H. Ye, J. Huang, J. J. Xu, N. K. A. C. Kodiweera, J. R. P. Jayakody, S. G. Greenbaum, *J. Power Sources* **178** (2008) 651.
- [9] G. Lakshminarayana, M. Nogami, *Solid State Ionics* **181** (2010) 760.
- [10] G. Lakshminarayana, R. Vijayaraghavan, M. Nogami, I. V. Kityk, *J. Electrochem. Soc.* **158** (2011) B376.
- [11] J. T. W. Wang, S. L. C. Hsu, *J. Electrochim. Acta* **56** (2011) 2842.

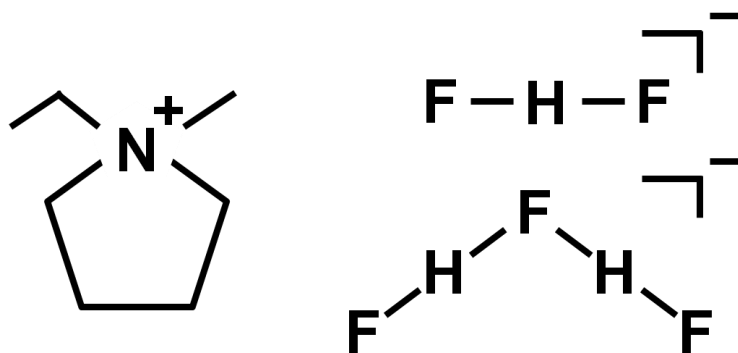


Fig. 3-1 Structures of EMPyr⁺ cation, and (FH)F⁻ and (FH)₂F⁻ anions.

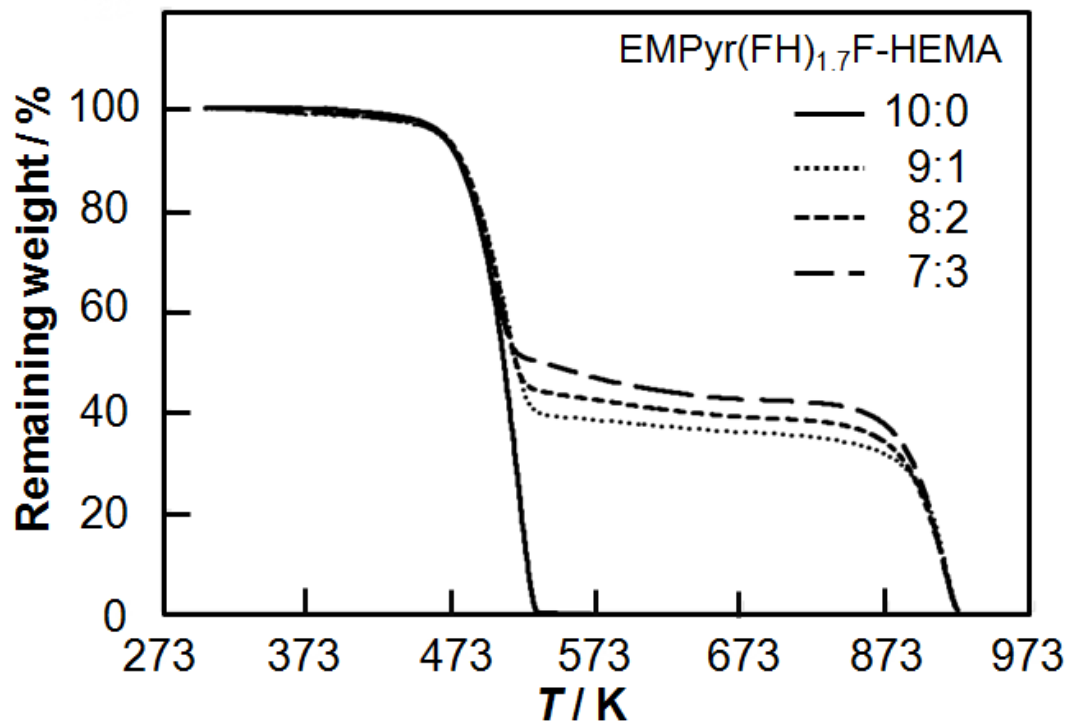


Fig. 3-2 TG curves for EMPyr(FH)_{1.7}F ionic liquid (10:0) and EMPyr(FH)_{1.7}F-HEMA composite membranes (9:1, 8:2, and 7:3).

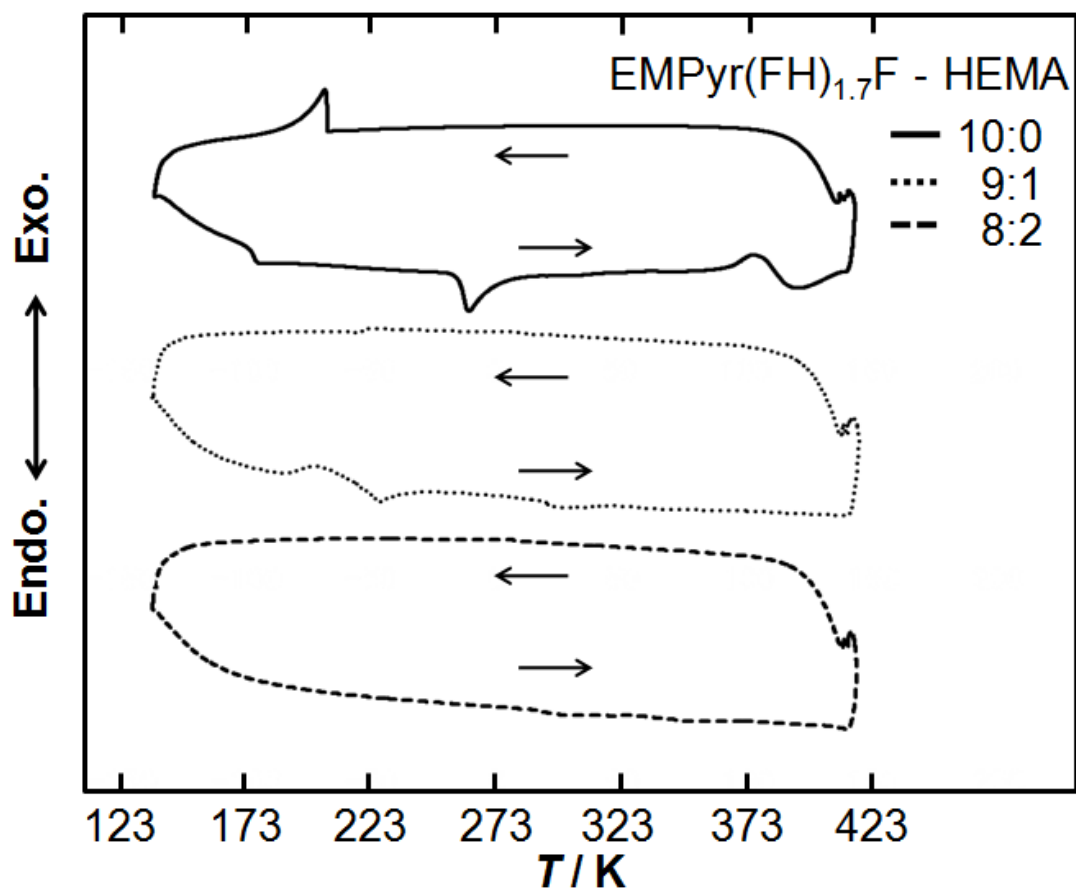


Fig. 3-3 DSC results for EMPyr(FH)_{1.7}F ionic liquid (10:0) and EMPyr(FH)_{1.7}F-HEMA composite membranes (9:1 and 8:2).

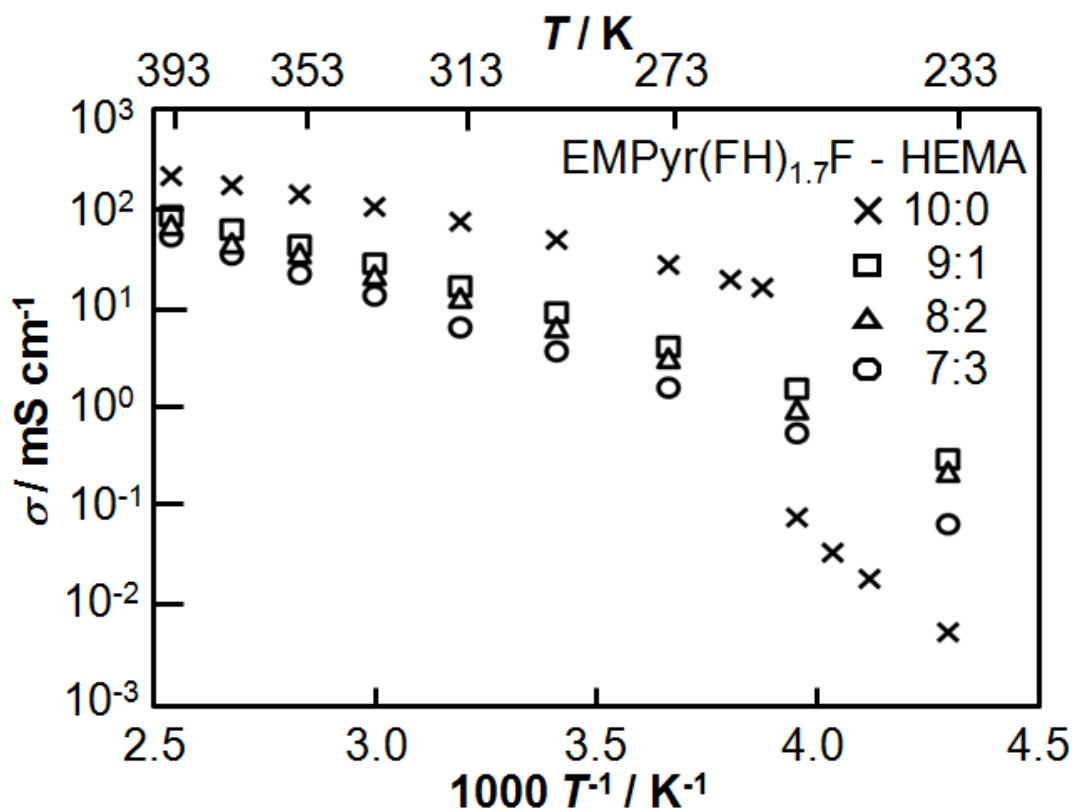


Fig. 3-4 Arrhenius plots of ionic conductivities for EMPyr(FH)_{1.7}F ionic liquid (10:0) and EMPyr(FH)_{1.7}F-HEMA composite membranes (9:1, 8:2, and 7:3).

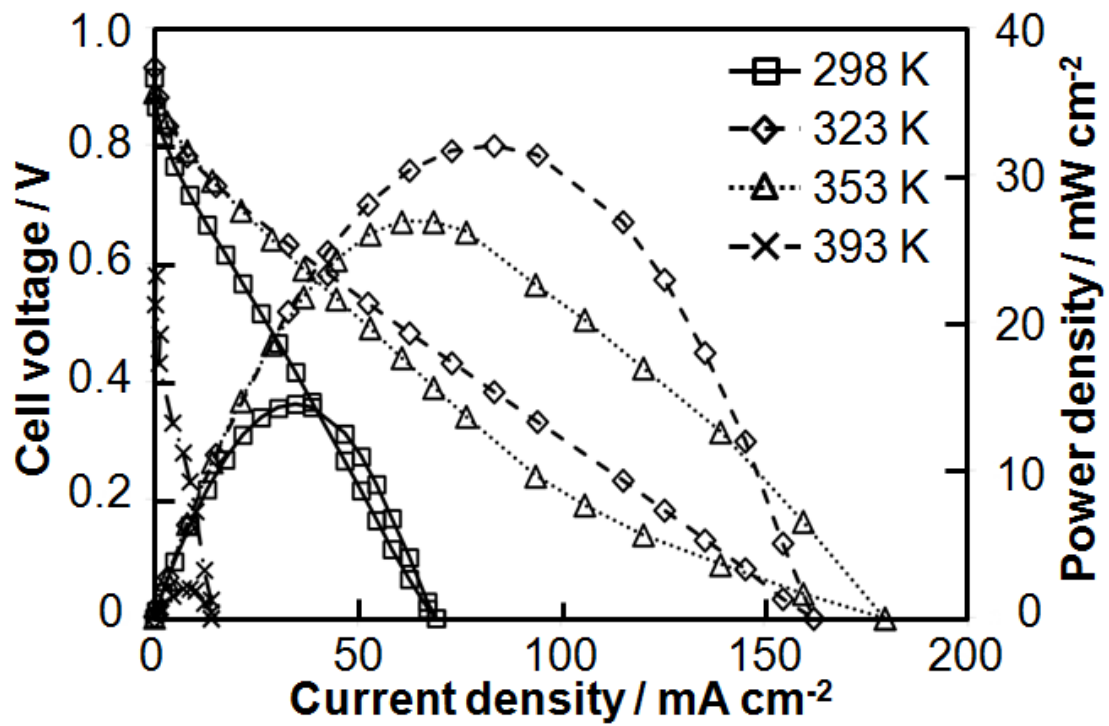


Fig. 3-5 i - V and i - p curves of a single cell using EMPyr(FH)_{1.7}F-HEMA (9:1) composite membrane under nonhumidified conditions. Anode and cathode catalyst: 1.0 mg Pt cm⁻².

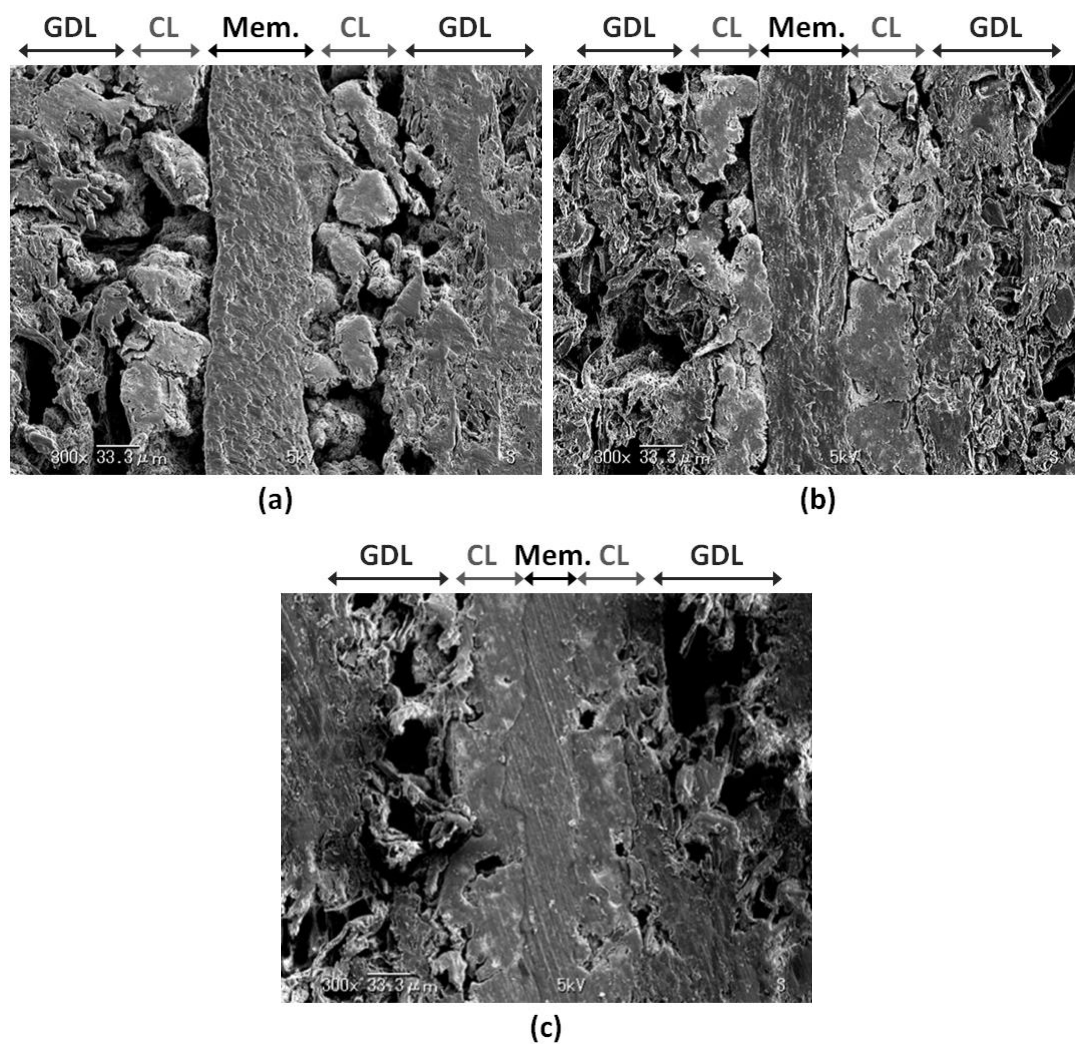


Fig. 3-6 Cross-sectional SEM images of the MEAs using EMPyr(FH)_{1.7}F-HEMA (9:1) composite membrane: (a) before single cell test, (b) after single cell test at 298–353 K, and (c) after single cell test at 393 K. (GDL = gas diffusion layer, CL = catalyst layer, Mem. = membrane.)

Chapter 4

Preparation, characterization and fuel cell performance of EMPyr(FH)_{1.7}F–HEMA composite membranes using a PI membrane support

4.1 Introduction

As mentioned in the previous chapters, ionic liquids (ILs) have recently been investigated for applications in electrochemical devices due to their high chemical and thermal stability, nonflammable and nonvolatile nature, and wide electrochemical window [1–3]. For fuel cell applications, they show potential as electrolytes which are operable under nonhumidified conditions at elevated temperatures [4–16]. Sekhon and coworkers were one of the firsts to report a composite membrane, which consisted of poly (vinylidene fluoride-co-hexafluoropropylene) copolymer and 2,3-dimethyl-1-octylimidazolium trifluoromethylsulfonate IL [4]. While the maximum power density at low humidity was extremely small compared to that of conventional PEFCs, Yasuda and colleagues developed a sulfonated polyimide and diethylmethylammonium trifluoromethylsulfonate composite membrane that showed approximately 100-fold improved performance at even higher temperatures, a very encouraging result [12].

In chapter 3, composite membranes consisting of EMPyr(FH)_{1.7}F and 2-hydroxyethylmethacrylate (HEMA) were prepared. Polytetrafluoroethylene (PTFE) was employed a membrane support. Single cells using this membrane in a molar ratio of 9:1 showed a decent maximum power density at 50 °C [17], yet presented significantly decreased performance once temperature rose to 120 °C. The reason for this

deterioration was revealed by cross-sectional SEM images of the membrane electrode assemblies (MEAs), showing that the composite membrane had softened and that the composite electrolyte had penetrated the gas diffusion electrodes (GDEs); this in turn resulted in a partial plug of the gas channels in the gas diffusion layer. Thermal deformation of the PTFE support likely accounts for at least part of the observed membrane softening; therefore, a new membrane support with higher mechanical strength is needed.

In this chapter, polyimide (PI) was tested as a replacement membrane support given its excellent thermomechanical properties; these improved properties, with respect to PTFE, are summarized in Table 4-1 [18]. Both polymers are thermally stable, with decomposition temperatures of 327 °C for PTFE and over 600 °C for PI; while these are both more than sufficient for operation at 120 °C, PTFE has significantly poorer mechanical strength and tends to easily deform under high pressure. For example, at 1.82 MPa, close to the actual compression pressure of 2 MPa observed during single cell fabrication, the thermal deformation temperature of PTFE is 55 °C, explaining the previously observed deformation; however, PI does not undergo thermal deformation at this pressure until 360 °C, meaning that using it might provide a potential solution to poor performance previously observed.

4.2 Experimental

4.2.1 Preparation of EMPyr(FH)_{1.7}F–HEMA composite membranes using PI membrane support

EMPy_r(FH)_{2.3}F was prepared using a previously reported method [19, 20]. EMPyr(FH)_{2.3}F was evacuated further by a rotary pump through a chemical trap for 4

days and then directly through a cold trap for 2 days at 120 °C under reduced pressure (< 1 Pa) to prepare EMPyr(FH)_{1.7}F which has negligible vapor pressure up to 120 °C. The appropriate extent of HF coordination was confirmed by hydrogen, carbon, nitrogen, and fluorine elemental analysis using a CHN coder and a fluoride ion selective electrode.

Preparation of the composite membrane began by mixing EMPyr(FH)_{1.7}F and HEMA (Wako) in molar ratios of either 8:2 or 9:1 under argon. Azobisisobutyronitrile (AIBN, Wako) was then added as a radical initiator, at 1 mol% of HEMA concentrations. A PI porous support (I.S.T., thickness: 16 or 30 μm, porosity: 50%) was then immersed in the mixture under vacuum for 1 h, after which the composite membrane was sandwiched between two PTFE sheets and polymerized at 70 °C under argon for 12 h. Fig. 4-1 (a) shows the front view of the EMPyr(FH)_{1.7}F–HEMA (9:1) composite membrane prepared with the 16-μm PI support, while the SEM image is presented in Fig. 4-1 (b). The membrane surface is flat and homogeneous.

4.2.2 Characterizations of composite membranes

A differential thermogravimetric analyzer (Thermo plus EVO2, Rigaku) was used to investigate EMPyr(FH)_{1.7}F and EMPyr(FH)_{1.7}F–HEMA thermal stability; the analysis was completed over the temperature range 25–800 °C at a scanning rate of 5 °C min⁻¹ under argon. Platinum pans were used due to their excellent chemical resistance to FHIL. Ionic conductivities of the composite membranes were measured in the longitudinal direction using a four-point probe method. The measurement cell consisted of two 10×5 mm² platinum plate electrodes placed 40 mm apart (these fed current to the sample) and four platinum needles (0.3 mm in diameter) separated by 5 mm (these

measured potential drops near the center of the membrane). Measurements were carried out by a.c. impedance using a Solartron 1286 electrochemical interface combined with a Solartron 1260 frequency response analyzer (AMETEK); scans were completed from -40 to 120 °C under nitrogen.

4.2.3 MEA fabrication and single cell test

The MEA was prepared by placing the composite membrane between two gas diffusion electrodes (KM Lab, 1.0 mg of platinum cm^{-2} , ionomer free) with a geometric surface area of 2.8×2.8 cm^2 . After constructing the single cell with the appropriate hardware (EFC-05-02-H2R, ElectroChem, 5 cm^2), cell tests were conducted using a Solartron 1286 electrochemical interface in a temperature controlled chamber from 25 to 120 °C under nonhumidified conditions. Dry H_2 (99.999%) was supplied from a hydrogen generator (Horiba Stec), while dry O_2 (99.999%) was supplied from a cylinder (Kyoto Teisan). Gas flow rates were set to 20 mL min^{-1} .

4.2.4 Cross-sectional SEM observation

MEA samples from both before and after the single cell test were cut by a design knife and embedded into a resin block using a resin mounting kit (20-3570, VariDur[®]). The sample block was then repeatedly polished with emery papers (No. 300, 600, 1200, 2000 and 3000, successively) on a rotating stage (100 rpm) to expose the cross-sectional area. The exposed surface was coated with gold using ion-sputtering equipment (E-1010, Hitachi) prior to observation with a scanning electron microscope (SEM, VE-8800, Keyence).

4.3 Results and discussion

4.3.1 Thermal stability

Fig. 4-2 shows thermogravimetric (TG) curves for the EMPyr(FH)_{1.7}F–HEMA (9:1 and 8:2) composite membranes with 16- μ m-thick (solid line) and 30- μ m-thick (dash line) PI supports. The TG curve of neat EMPyr(FH)_{1.7}F is provided for comparison. All samples show similar initial weight losses at 170–230 °C, the result of EMPyr(FH)_{1.7}F decomposition. An additional weight loss proceeds gradually until 550 °C, this resulting from the slow decomposition of poly-HEMA; unsurprisingly, this process is significantly slower for the 8:2 samples. Finally, weight loss is also observed from 550 °C, corresponding to the decomposition of the PI support. However they are not completely decomposed and some residues still remain even at 800 °C. Since thermal stability is determined by the initial decomposition temperature, all composites were found to be thermally stable up to 170 °C, regardless of HEMA content or the thickness of the PI support.

4.3.2 Ionic conductivity

Fig. 4-3 shows Arrhenius plots of ionic conductivities for neat EMPyr(FH)_{1.7}F and all prepared EMPyr(FH)_{1.7}F–HEMA composites. The neat IL showed an ionic conductivity of 205 mS cm⁻¹ at 120 °C, while the composite ionic conductivity increased with FHIL content. The EMPyr(FH)_{1.7}F–HEMA (9:1) composite utilizing the 16- μ m PI showed an ionic conductivity of 75 mS cm⁻¹ at 120 °C which, though slightly lower than the 82 mS cm⁻¹ of the previously tested PTFE sample [17], is still high compared to other IL-based composite membranes; e.g., 20 mS cm⁻¹ at 120 °C for [dema][TfO]–sPI (7.5:1.5 in weight ratio) [11]. This decreased ionic conductivity can be

explained by the 50% porosity of the PI support, compared to the 80% porosity of PTFE; this difference results in a lower FHIL loading.

For comparison, the ionic conductivities of composite membranes using thicker membrane supports were also investigated; the corresponding data is also presented in Fig. 4-3, which shows little difference despite the change. This indicates that the EMPyr(FH)_{1.7}F-HEMA composite electrolyte is uniformly distributed in the PI membrane support regardless of thickness.

4.3.3 Single cell performance under nonhumidified conditions

Fig. 4-4 shows the i - V and i - p curves for a single cell constructed from EMPyr(FH)_{1.7}F-HEMA (9:1) and 16- μ m-thick PI. At 25 °C, the open circuit voltage is around 0.9 V and the maximum power density is 12 mW cm⁻². Performance proceeds to increase with temperature owing to the increased electrochemical reaction rate. The maximum power density of 31 mW cm⁻² is observed at 120 °C. Unlike the previous results in which PTFE was used [17], no deterioration was observed over 50 °C, indicating at least a partial solution to the previous problem.

Fig. 4-5 shows the temperature dependence of the maximum power densities for single cells using EMPyr(FH)_{1.7}F-HEMA (9:1) composite membranes and either 16- μ m-thick PI or 65- μ m-thick PTFE. At 25–50 °C, the PTFE shows higher maximum power density, with a highest value of 34 mW cm⁻² at 50 °C. The value then significantly decreases above 80 °C, again likely due to deterioration. However, the corresponding value for the PI sample increases steadily with temperature, with a power density at 120 °C that is far superior to that obtained with PTFE.

The single cells can be stably operated for 5–6 hours. However, the cell

performance gradually declines afterwards. The cause of this problem is explained by the leakage of FHIL from the composite membranes because this FHIL is hydrophilic and water-soluble. The improvement of stability is a major task for this type of membrane.

Single cell performance generally improves when using optimized three-phase boundaries. Note that no surface contact improvement techniques were employed here, however, with the membrane simply having been placed between the two GDEs. The three-phase boundary area can be enhanced by inserting the composite electrolyte directly into the catalyst layer. In addition, hotpressing can also be used in order to improve contact. To effectively employ these techniques, further optimization is needed.

4.3.4 Cross-sectional SEM image

Cross-sectional SEM images of the MEAs for single cells using EMPyr(FH)_{1.7}F-HEMA (9:1) and either 65- μ m-thick PTFE [17] or 16- μ m-thick PI are provided in Fig. 4-6 (a) and (b), respectively; images are provided for samples taken both before and after single cell tests, while the yellow arrows indicate membrane thickness. The thickness of the PTFE membrane decreases significantly after the test, again suggesting deformation. On the other hand, no significant difference is observed in the PI membrane thickness, again indicating improved mechanical performance. Accordingly, the electrolyte penetration into gas diffusion layer is prevented and the MEA structure is well-preserved. Overall, changing the membrane support seems to have resolved the issue of electrolyte softening.

4.4 Conclusion

PI membrane supports have been used in place of PTFE in order to improve the mechanical properties of EMPyr(FH)_{1.7}F and HEMA composite membranes. TG analysis showed that the prepared composite membranes had good thermal stability up to 170 °C. Meanwhile, the EMPyr(FH)_{1.7}F–HEMA (9:1) composite membrane supported by a 16- μ m-thick PI layer showed good ionic conductivity of 75 mS cm⁻¹ at 120 °C. Nonhumidified single cell tests ranging from 25 to 120 °C revealed that performance improved with temperature, a result that was distinct from previous research using PTFE; a maximum power density of 31 mW cm⁻² was observed at 120 °C. Meanwhile, cross-sectional SEM images revealed no significant difference in membrane thickness as a result of testing, meaning that the previous problem of membrane softening and penetration to the GDE has been solved.

Acknowledgment

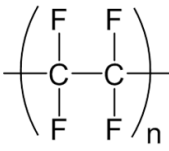
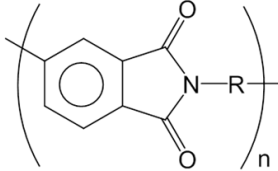
The PI membrane supports were provided free of charge by I.S.T., Japan.

References

- [1] K. R. Seddon, *J. Chem. Technol. Biotechnol.* **68** (1997) 351.
- [2] T. Welton, *Chem. Rev.* **99** (1999) 2071.
- [3] P. Wasserscheid, W. Keim, *Angew. Chem. Int. Ed.* **39** (2000) 3772.
- [4] S. S. Sekhon, B. Singh Lalia, J. S. Park, C. S. Kim, K. Yamada, *J. Mater. Chem.* **16** (2006) 2256.
- [5] S. S. Sekhon, P. Krishnan, B. Singh Lalia, K. Yamada, C. S. Kim, *Electrochim. Acta* **52** (2006) 1639.
- [6] B. Singh Lalia, S. S. Sekhon, *Chem. Phys. Lett.* **435** (2006) 294.
- [7] A. Fericola, S. Panero, B. Scrosati, M. Tamada, H. Ohno, *ChemPhysChem.* **8** (2007) 1103.
- [8] A. Fericola, M. A. Navarra, S. Panero, *J. Appl. Electrochem.* **38** (2008) 993.
- [9] E. K. Cho, J. S. Park, S. S. Sekhon, G. G. Park, T. H. Hyun, W. Y. Lee, C. S. Kim, S. B. Park, *J. Electrochem. Soc.* **156** (2009) B197.
- [10] S. Y. Lee, T. Yasuda, M. Watanabe, *J. Power Sources* **195** (2010) 5909.
- [11] S. Y. Lee, A. Ogawa, M. Kanno, H. Nakamoto, T. Yasuda, M. Watanabe, *J. Am. Chem. Soc.* **132** (2010) 9764.
- [12] T. Yasuda, S. Nakamura, Y. Honda, K. Kinugawa, S. Y. Lee, M. Watanabe, *ACS Appl. Mater. Interfaces* **4** (2012) 1783.
- [13] J. Malis, P. Mazur, J. Schauer, M. Paidar, K. Bouzek, *Int. J. Hydrogen Energy* **38** (2013) 4697.
- [14] A. L. Saroj, R. K. Singh, S. Chandra, *Mat. Sci. and Eng. B* **178** (2013) 231.
- [15] M. W. Schulze, L. D. McIntosh, M. A. Hillmyer, T. P. Lodge, *Nano Lett.* **14** (2014) 122.

- [16]S. Liu, L. Zhou, P. Wang, F. Zhang, S. Yu, Z. Shao, B. Yi, *ACS Appl. Mater. Interfaces* **6** (2014) 3195.
- [17]P. Kiatkittikul, T. Nohira, R. Hagiwara, *J. Power Sources* **220** (2012) 10.
- [18]Yoshida SKT, Properties of fluorine resin, Teflon and other engineering resins (2014), can be found under www.y-skt.co.jp/husso.html.
- [19]K. Matsumoto, R. Hagiwara, Y. Ito, *Electrochem. Solid-State Lett.* **7** (2004) E41.
- [20]R. Hagiwara, T. Hirashige, T. Tsuda, Y. Ito, *J. Electrochem. Soc.* **149** (2002) D1.

Table 4-1 Thermal and mechanical properties of PTFE and PI [18].

Properties	PTFE	PI
Chemical structure		
Melting point / °C	327	—*
Decomposition temp. / °C	360–450	> 600
Tensile strength/ MPa	20–35	86
Elongation/%	200–400	7.5
Compressive strength (10% changed) / MPa	10–15	133
Thermal deformation temp. at 0.45 MPa / °C	120	—
Thermal deformation temp. at 1.82 MPa / °C	55	360

*Glass transition temperature > 400 °C.

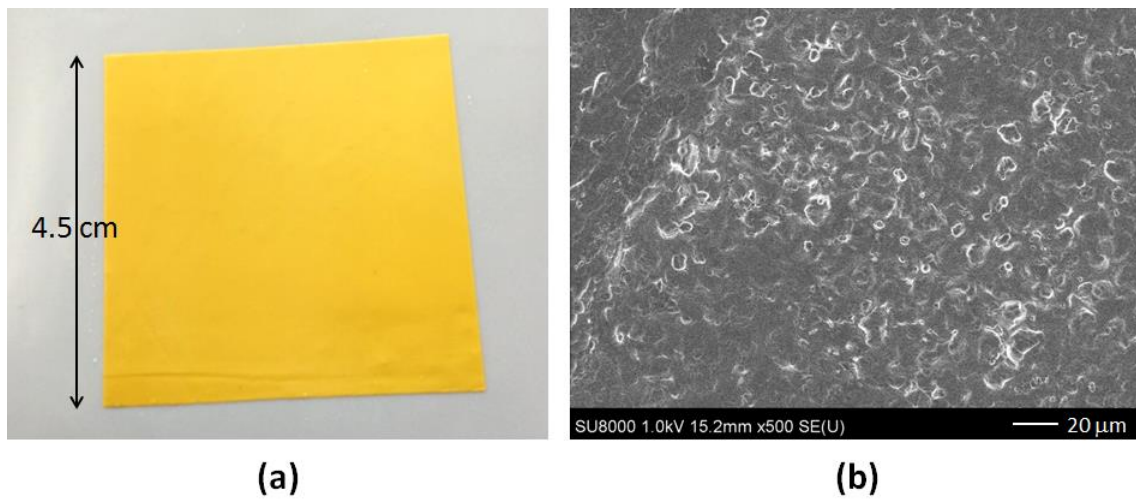


Fig. 4-1 (a) Front view and (b) SEM image of EMPyr(FH)_{1.7}F-HEMA (9:1) composite membrane with PI (16 μm) membrane support.

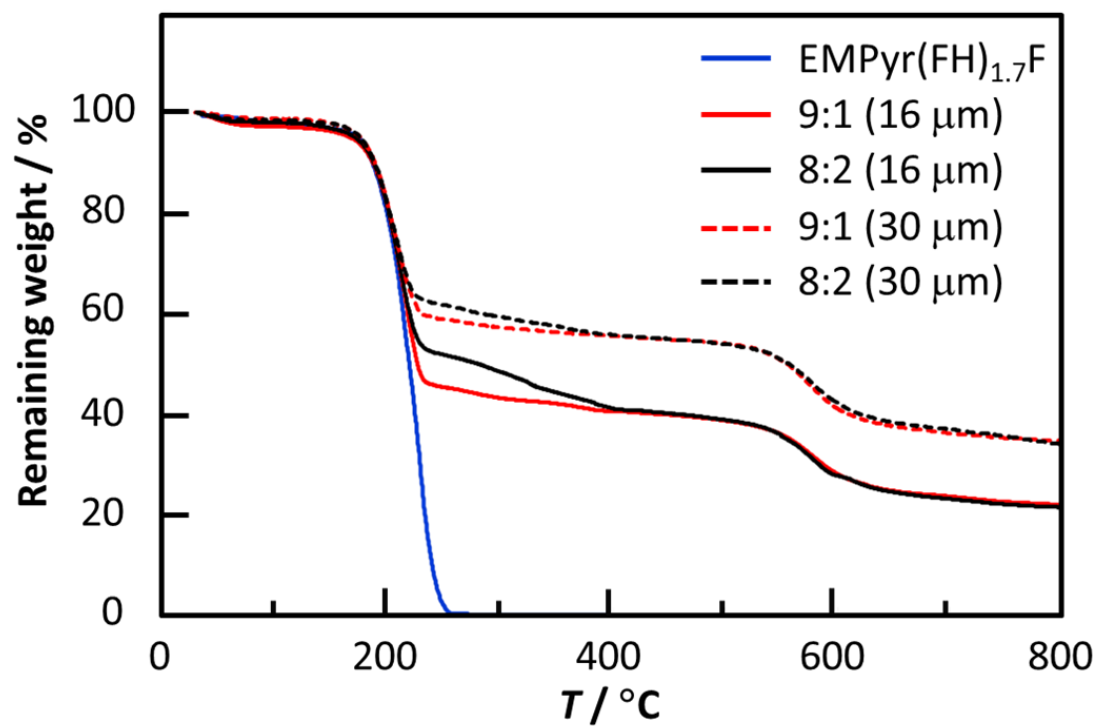


Fig. 4-2 TG curves of neat EMPyr(FH)_{1.7}F IL and EMPyr(FH)_{1.7}F-HEMA (9:1 and 8:2) composite membranes with PI (16 and 30 μm) membrane supports. Scan rate: 5 °C min⁻¹.

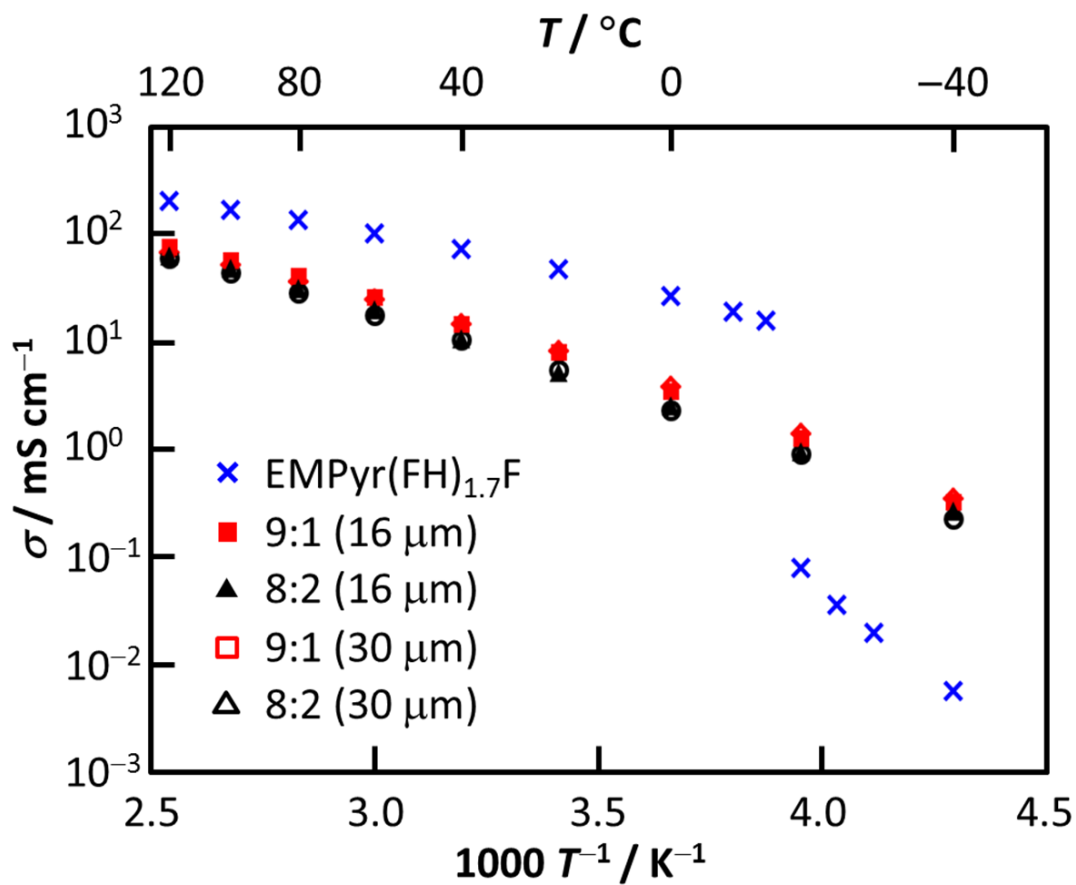


Fig. 4-3 Arrhenius plots of ionic conductivities for neat EMPyr(FH)_{1.7}F IL and EMPyr(FH)_{1.7}F-HEMA (9:1 and 8:2) composite membranes with PI (16 and 30 μm) membrane supports.

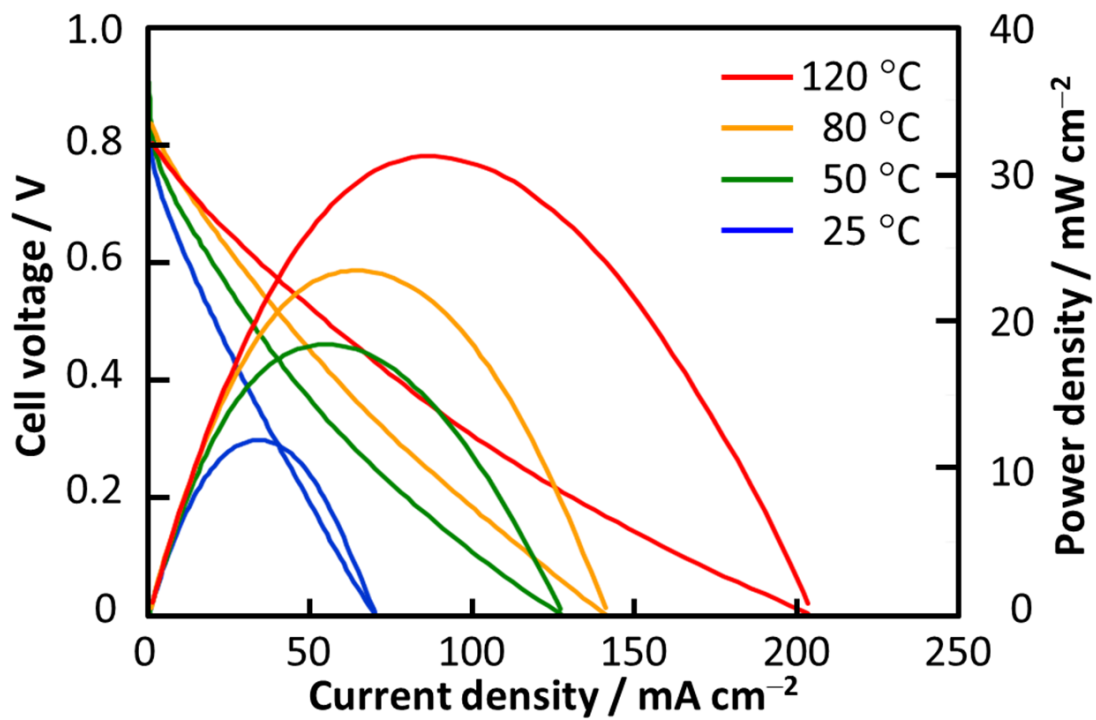


Fig. 4-4 i - V and i - P characteristic curves of a single cell using EMPyr(FH)_{1.7}F-HEMA (9:1) composite membrane with PI (16 μ m) membrane support, operated from 25 to 120 °C under nonhumidified conditions. Anode and cathode catalyst: 1.0 mg Pt cm⁻².

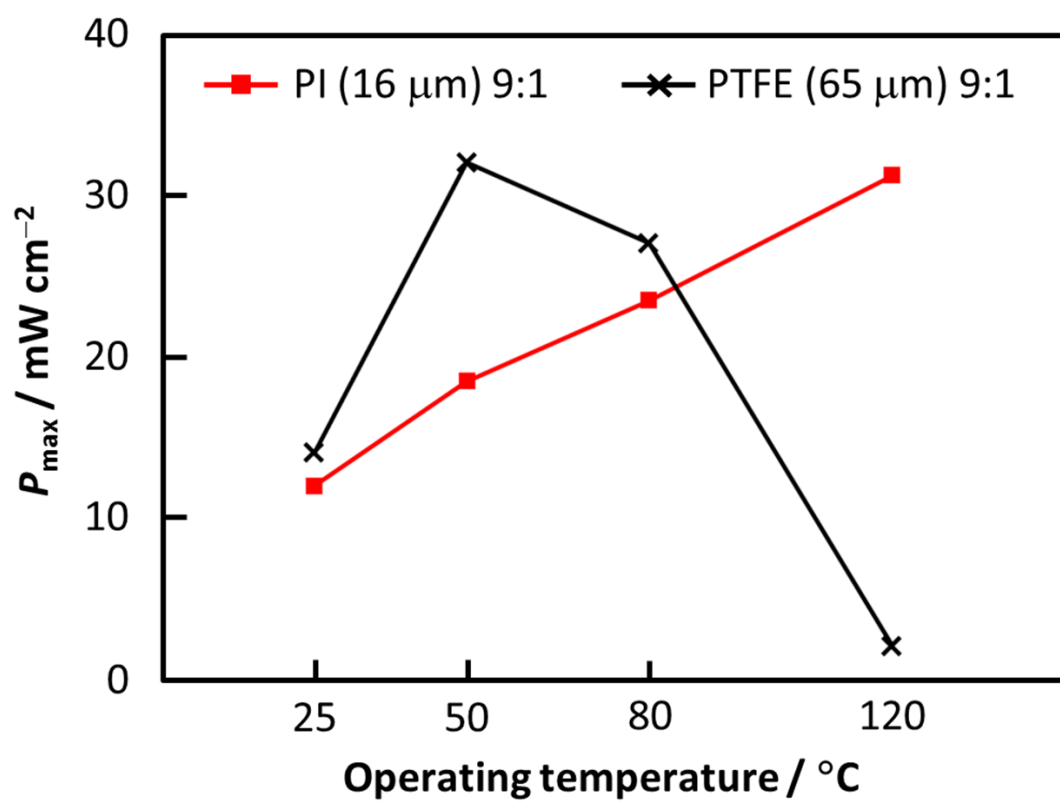


Fig. 4-5 Temperature dependences of maximum power densities (P_{\max}) for single cells using EMPyr(FH)_{1.7}F-HEMA (9:1) composite membranes with PI (16 μm) and PTFE (65 μm) membrane supports under nonhumidified conditions.

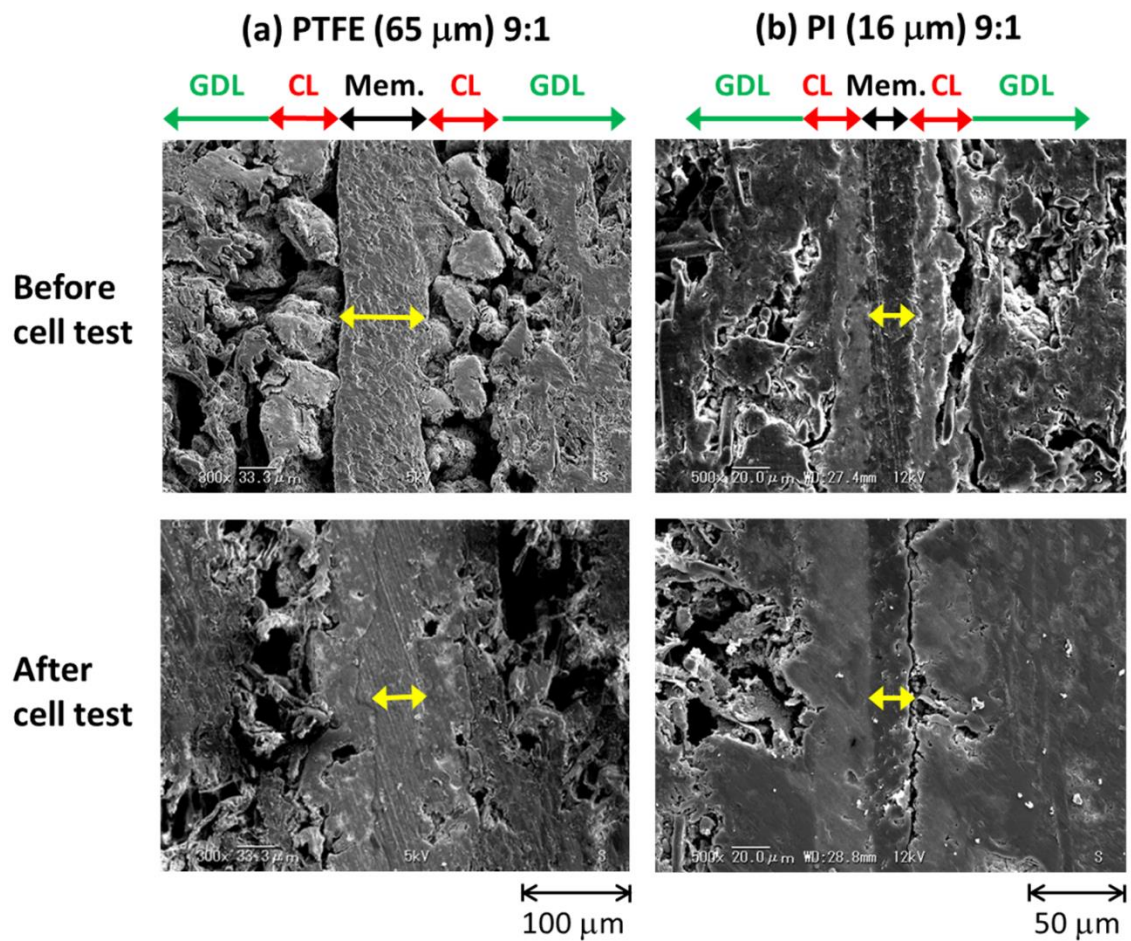


Fig. 4-6 Cross-sectional SEM images of the MEAs using EMPyr(FH)_{1.7}F-HEMA (9:1) composite membranes with; (a) PI (16 μm) and (b) PTFE (65 μm) membrane supports, before and after single cell test at 25–120 $^{\circ}\text{C}$. (GDL = gas diffusion layer, CL = catalyst layer, Mem. = membrane.)

Chapter 5

Preparation, characterization and fuel cell performance of EMPyr(FH)_{1.7}F/PVdF-HFP composite membrane using no membrane support

5.1 Introduction

As mentioned in section 1.4.3 of chapter 1, operation mechanisms for nonhumidified fuel cells using FHILs as electrolytes; whose cells are referred to as fluorohydrogenate fuel cells (FHFCs), has already been reported [1]. This type of fuel cell can be operated at elevated temperatures under nonhumidified conditions owing to their unique mechanism, which involves the transfer of hydrogen and charges by fluorohydrogenate anions. Hence, water is unnecessary for the hydrogen transportation mechanism. Composite membranes consisting of 1-ethyl-3-methylimidazolium fluorohydrogenate (EMIm(FH)_nF, $n = 1.3$ and 2.3) and poly(vinylidene fluoride-co-hexafluoropropylene) (PVdF-HFP) copolymer have also been successfully prepared [2]. A single cell using one of these membranes gave a maximum power density of 20 mW cm^{-2} at $120 \text{ }^\circ\text{C}$ under nonhumidified conditions [2].

A later study revealed that *N*-ethyl-*N*-methylpyrrolidinium fluorohydrogenate (EMPyr(FH)_{1.7}F) is a more promising electrolyte for nonhumidified fuel cells [3]. Chapter 6 further confirmed that it exhibits higher activity towards the oxygen reduction reaction at Pt electrodes and a lower H₂O₂ yield than other FHILs. In chapter 3, a single cell using a composite membrane consisting of EMPyr(FH)_{1.7}F and HEMA in a weight

ratio of 9.2:0.8 showed a decent maximum power density of 32 mW cm^{-2} at $50 \text{ }^\circ\text{C}$. Considering the above reports, a composite membrane consisting of EMPyr(FH)_{1.7}F and PVdF-HFP is expected to give an even higher power density.

In this chapter with the aim of improved cell performance, composite membranes composed of EMPyr(FH)_{1.7}F and PVdF-HFP are investigated. Unlike HEMA, PVdF-HFP, whose structure is shown in Fig. 5-1, has been widely used and investigated as a potential polymer material for IL-based polymer membranes due to its good thermal and chemical stabilities [4–10]. The IL/PVdF-HFP composite membranes that have been prepared using a casting method are summarized in Table 5-1. Sekhon et al. prepared composite membranes of PVdF-HFP and 2,3-dimethyl-1-octylimidazolium trifluoromethylsulfonate ([DMOIm][TfO]) or 2,3-dimethyl-1-octylimidazolium bis(trifluoromethylsulfonyl)imide ([DMOIm][TFSI]) [5, 6]; the maximum power densities of cells with these membranes at $100 \text{ }^\circ\text{C}$ under nonhumidified conditions were 1.0 and 0.2 mW cm^{-2} , respectively. Malis et al. also reported polymer electrolytes prepared by casting PVdF-HFP with either 1-butyl-3-methylimidazolium trifluoromethylsulfonate ([BMIm][TfO]) or *N*-ethylimidazolium trifluoromethylsulfonate ([EIm][TfO]) [10]. They were reportedly thermally stable up to $140 \text{ }^\circ\text{C}$. At $140 \text{ }^\circ\text{C}$, single cell tests under nonhumidified conditions revealed that these composite membranes showed maximum power densities of 0.6 and 0.1 mW cm^{-2} , respectively [10]. Although they still have low power densities, which are mainly due to their low ionic conductivities, the performance should improve upon the combination of PVdF-HFP with a highly conductive IL such as EMPyr(FH)_{1.7}F.

5.2 Experimental

5.2.1 Preparation of EMPyr(FH)_{1.7}F/PVdF-HFP composite membranes

EMPy_r(FH)_{2.3}F was prepared using a previously reported method [11, 12]. EMPyr(FH)_{2.3}F was evacuated further by a rotary pump through a chemical trap for 4 days and then directly through a cold trap for 2 days at 120 °C under reduced pressure (< 1 Pa). Finally, EMPyr(FH)_{1.7}F which has a negligible vapor pressure at 120 °C was prepared.

Scheme 5-1 shows the procedure for preparation of the composite membranes. PVdF-HFP ($M_n = 110000$, Aldrich) was dissolved in acetone (99.9%, Wako) to prepare a 5 wt% PVdF-HFP solution. EMPyr(FH)_{1.7}F was added to the polymer solution at FHIL/polymer weight ratios of 7:3, 6:4, and 5:5. This method differs from the previous method used in chapter 3 and 4 in that no membrane support was used. The mixed solution was stirred for >1 h using a magnetic stirrer until a homogeneous solution was obtained. Then, it was cast onto perfluoroalkoxy (PFA) Petri dishes and dried at 80 °C for 12 h under an argon atmosphere. Finally, the composite membranes were peeled from the Petri dishes. Fig. 5-2 shows a photograph of the EMPyr(FH)_{1.7}F/PVdF-HFP (7:3) composite membrane. Transparent, thin, and homogeneous membranes were obtained.

5.2.2 Characterizations of composite membranes

The thermal stabilities of the prepared membranes were determined via TG analysis using a differential thermogravimetric analyzer (Thermo plus EVO2, Rigaku). The analysis was conducted in the temperature range of 25–800 °C at a scanning rate of 5 °C min⁻¹ under an argon atmosphere. Platinum pans were used because of their excellent chemical resistance to FHILs. The ionic conductivities of the composite

membranes were measured in the longitudinal direction using a four-point probe method. Measurements were carried out from -40 to 120 °C under a nitrogen atmosphere using an a.c. impedance method with a Solartron 1286 electrochemical interface combined with a Solartron 1260 frequency response analyzer (AMETEK). Field emission scanning electron microscopy (FE-SEM; SU-8020, Hitachi) was utilized to observe the membrane surface morphologies. Prior to the observation, the membrane samples were coated with platinum using ion-sputtering equipment (MC-100, Hitachi).

5.2.3 MEA fabrication and single cell test

The MEA was prepared by placing the composite membrane directly between two gas diffusion electrodes (GDEs, 1.0 mg Pt cm^{-2} , ionomer free, KM Lab) with geometric surface areas of 1 cm^2 . After incorporating the MEA into a single cell with fuel cell hardware (EFC-01-02, 1 cm^2 , ElectroChem), single cell tests were conducted using a Solartron 1286 electrochemical interface in a temperature-controlled chamber at 25 – 120 °C under nonhumidified conditions. Anhydrous H_2 (99.999%) was supplied by a hydrogen generator (HORIBA STEC), and O_2 was supplied from a cylinder (99.9999%, Kyoto Teisan); their flow rates were set at 10 mL min^{-1} .

5.2.4 *In-situ* a.c. impedance analysis

Along with the fuel cell operation, *in situ* AC impedance analysis was also performed. A Solartron 1260 frequency response analyzer (AMETEK) combined with a Solartron 1286 electrochemical interface (AMETEK) was used to provide a.c. signal and analyze the responding impedance. An a.c. potential of 10 mV was applied to the single cell as an excitation signal under a constant cell voltage of 0.6 V. The frequency

range was from 20 kHz to 20 mHz. The approximate values of bulk resistance, charge transfer resistance, and mass transfer resistance were determined by fitting the resultant Nyquist plots with a suitable equivalent circuit.

5.2.5 Cross-sectional SEM observation

MEA samples from before and after the cell test were cut using a knife and embedded into a resin block using a resin mounting kit (20-3570, VariDur[®]). The prepared sample block was then consecutively polished with No. 300, 600, 1200, 2000, and 3000 emery papers on a rotating stage (100 rpm) to expose the cross-sectional area. The exposed surface was coated with gold using ion-sputtering equipment (E-1010, Hitachi) and then observed via SEM (VE-8800, Keyence).

5.3 Results and Discussion

5.3.1 Thermal stability

Fig. 5-3 shows TG curves for the EMPyr(FH)_{1.7}F/PVdF-HFP (7:3 and 6:4) composite membranes. For comparison, the TG curves of neat EMPyr(FH)_{1.7}F and neat PVdF-HFP are also provided. All the FHIL/PVdF-HFP membranes showed similar initial weight losses at 140 °C, which is at a lower temperature than that of neat FHIL. This early weight loss is considered to be due to decomposition of some parts of PVdF-HFP, which has a melting point of about 140 °C. A second weight loss was observed at 170 °C, which corresponds to decomposition of EMPyr(FH)_{1.7}F, as has been previously observed for EMPyr(FH)_{1.7}F/HEMA membranes in chapter 3.3.1. Between 250 and 600 °C, additional weight was slowly lost because of the slow decomposition of the major fraction of PVdF-HFP. However, some residues remained even at 800 °C.

Since the thermal stability is determined by the initial decomposition temperature, all composite membranes were expected to be thermally stable up to 140 °C regardless of the FHIL content. This value is considered to be sufficient for fuel cell operation at 120 °C.

5.3.2 Ionic conductivity

Fig. 5-4 shows Arrhenius plots of the ionic conductivities of the EMPyr(FH)_{1.7}F/PVdF-HFP (7:3, 6:4, and 5:5) composite membranes. The ionic conductivities of EMPyr(FH)_{1.7}F/HEMA (9.2:0.8) and neat EMPyr(FH)_{1.7}F are also given for comparison. While the ionic conductivity of neat FHIL was as high as 205 mS cm⁻¹ at 120 °C, those of the composite membranes were lower and dependent on the FHIL content. The EMPyr(FH)_{1.7}F/PVdF-HFP (7:3) composite membrane exhibited an ionic conductivity of 41 mS cm⁻¹ at 120 °C, which is lower than the 82 mS cm⁻¹ of EMPyr(FH)_{1.7}F/HEMA (9.2:0.8). This decrease of the conductivity was attributed to its lower FHIL content. Nevertheless, this value remains impressive in comparison to those of other IL/PVdF-HFP composite membranes, as listed in Table 5.1.

5.3.3 Surface morphology

Figs. 5-5(a) and (b) show SEM images of EMPyr(FH)_{1.7}F/PVdF-HFP (7:3) and EMPyr(FH)_{1.7}F/HEMA (9.2:0.8) composite membranes, respectively. While the FHIL/HEMA membranes had a rather smooth and consistent surface, the FHIL/HEMA membrane had a rough surface; this roughness is evident at both macroscopic and microscopic scales. These results indicate that the EMPyr(FH)_{1.7}F/PVdF-HFP (7:3) composite membrane possessed a large membrane surface area, especially when

compared with that of HEMA-based membranes. The increased membrane surface area is expected to enhance the effective three-phase boundary area and improve cell performance. In addition, the effect of FHIL content on the surface morphology of the composite membrane was also studied. Figs. 5-6(a), (b), and (c) exhibit SEM images of EMPyr(FH)_{1.7}F/PVdF-HFP membranes with FHIL/PVdF-HFP weight ratios 7:3, 6:4, and 5:5, respectively. The roughness of the membrane surface increased with increasing FHIL content in the membrane. Hence, the largest surface area is expected to be obtained for the membrane with a weight ratio of 7:3.

5.3.4 Single cell performance under nonhumidified conditions

Fig. 5-7 shows $i-V$ and $i-P$ characteristic curves for a single cell containing the EMPyr(FH)_{1.7}F/PVdF-HFP (7:3) composite membrane. At 25 °C, a maximum power density of 63 mW cm⁻² was observed; this is the highest value ever reported for FHFCs at 25 °C. The cell performance continued to increase with increasing temperature owing to the increased electrochemical reaction rate until 50 °C, at which the maximum power density of 103 mW cm⁻² was observed. This value is very high and exceeds the 32 mW cm⁻² of a single cell using an EMPyr(FH)_{1.7}F/HEMA (9.2:0.8) composite membrane, reported in chapter 3.3.3, at the same temperature. However, the cell performance deteriorated above 80 °C. This deterioration trend is similar to that of cells containing FHIL/HEMA membranes. The problem is explained as follows: At higher temperatures, the composite electrolyte softens and penetrates into the gas diffusion electrodes, which partially plugs the gas channels in the gas diffusion layer.

5.3.5 *In-situ* a.c. impedance

To elucidate the cause of performance deterioration, *in situ* a.c. impedance analysis was carried out along with the single cell tests. Fig. 5-8(a) shows a Nyquist plot of a single cell with an EMPyr(FH)_{1.7}F/PVdF-HFP (7:3) composite membrane at 0.6 V. The first x-intercept corresponds to the bulk (or Ohmic) resistance while the next two semicircles represent the resistances from charge transfer and mass transfer, respectively. To approximate each resistance, the resultant Nyquist plot was fitted to an equivalent circuit shown in Fig. 5-9. Fig. 5-8(b) exhibits the temperature dependence of the bulk resistance (R_b), charge transfer resistance (R_{CT}), mass transfer resistance (R_{MT}), and total resistance (R_{tot}). R_b decreased with temperature because of the increased ionic conductivity. The change in R_b was, however, negligible because its value was very small relative to the total resistance. On the other hand, R_{MT} significantly increased when the temperature was elevated from 50 to 80 °C. This result reflects the poor mobility of the reactant gases to the three-phase boundary above 50 °C, which is consistent with the speculation that the gas channels were obstructed by the softened composite electrolyte, as mentioned in section 5.3.4. Similarly, R_{CT} also significantly increased with increasing temperature from 50 to 80 °C. The reason is as follows: At elevated temperatures, the softened composite electrolyte penetrates into both the catalyst layer and gas diffusion layer. Since the majority of the catalyst layer is fully filled with electrolyte, the effective three-phase boundary area decreases. Thus, the catalyst was ineffectively utilized, resulting in increased R_{CT} .

5.3.6 Cross-sectional SEM image

To verify whether the composite electrolyte softened, cross-sectional SEM observations of the MEAs before and after the cell test were performed, as shown in Fig.

5-10. The dashed lines indicate the interface between the membrane and catalyst layer. Before the cell test, the membrane (Mem.), catalyst (CL), and gas diffusion (GDL) layers were in good contact with each other. However, after the cell test, the membrane thickness decreased, indicating softening of the membrane. The softened electrolyte then escaped from the original location and penetrated into both the CL and GDL, thereby decreasing the three-phase boundary area of the CL and plugging the gas channels in the GDL. This result well explains the increase in the R_{CT} and R_{MT} values at 80 °C in the a.c. impedance analysis.

5.4 Conclusion

Composite membranes consisting of EMPyr(FH)_{1.7}F IL and PVdF-HFP copolymer were successfully prepared by a casting method using acetone as the solvent. The prepared membranes had rough surfaces, which could enlarge the three-phase boundaries. For the EMPyr(FH)_{1.7}F/PVdF-HFP (7:3 weight ratio) composite membrane, the ionic conductivity was 41 mS cm⁻¹ at 120 °C. In a single cell test, a maximum power density of 103 mW cm⁻² was observed at 50 °C under nonhumidified conditions, which is the highest value among reported FHFCs. However, the cell performance decreased at 80 °C. According to *in situ* a.c. impedance analyses and cross-sectional SEM observations of the MEAs, the deterioration was caused by penetration of the softened composite electrolyte into the gas diffusion electrodes, which decreased the three-phase boundary area in the CL and plugged gas channels in the GDL.

References

- [1] R. Hagiwara, T. Nohira, K. Matsumoto, Y. Tamba, *J. Electrochem. Solid-State Lett.* **8** (2005) A231.
- [2] J.S. Lee, T. Nohira, R. Hagiwara, *J. Power Sources* **171** (2007) 535.
- [3] Y. Tani, T. Nohira, T. Enomoto, K. Matsumoto, R. Hagiwara, *J. Electrochim. Acta* **56** (2011) 3852.
- [4] M. A. Navarra, S. Panero, B. Scrosati, *Electrochem. Solid-State Lett.* **8** (2005) A324.
- [5] S. S. Sekhon, B. Singh Lalia, J. S. Park, C. S. Kim, K. Yamada, *J. Mater. Chem.* **16** (2006) 2256.
- [6] S. S. Sekhon, P. Krishnan, B. Singh Lalia, K. Yamada, C. S. Kim, *Electrochim. Acta* **52** (2006) 1639.
- [7] B. Singh Lalia, S. S. Sekhon, *Chem. Phys. Lett.* **425** (2006) 294.
- [8] A. Fericola, S. Panero, B. Scrosati, M. Tamada, H. Ohno, *ChemPhysChem.* **8** (2007) 1103.
- [9] A. Fericola, M. A. Navarra, S. Panero, *J. Appl. Electrochem.* **38** (2008) 993.
- [10] J. Malis, P. Mazur, J. Schauer, M. Paidar, K. Bouzek, *Int. J. Hydrogen Energy* **38** (2013) 4697.
- [11] R. Hagiwara, T. Hirashige, T. Tsuda, Y. Ito, *J. Electrochem. Soc.* **149** (2002) D1.
- [12] K. Matsumoto, R. Hagiwara, Y. Ito, *Electrochem. Solid-State Lett.* **7** (2004) E41.

Table 5-1 IL/PVdF-HFP composite membranes prepared by casting method.

(IL = ionic liquid, Pol. = polymer, Ad. = additive, T = temperature, σ = conductivity and P = power density)

Polymer	Additive	IL	IL:Pol.(:Ad.) (w/w/w)	Solvent	T / °C	time / h	σ / mS cm ⁻¹	P / mW cm ⁻²	Ref.
PVdF-HFP ($M_n = 100000$)	H[TfO]	[DMPIm][TFSI]	7.7:2(:0.3)	-	130 and RT	Repeated several times	10 at 100 °C	-	[24]
PVdF-HFP ($M_n = 130000$)	H[TfO]	[DMOIm][TfO]	5:5	CH ₃ CN	-	-	0.96 at 80 °C	1.0 at 100 °C	[25]
PVdF-HFP ($M_n = 130000$)	H[TFSI]	[DMOIm][TFSI]	5:5	CH ₃ CN	-	-	2.74 at 130 °C	0.2 at 100 °C	[26]
PVdF-HFP ($M_n = 130000$)	H[H ₂ PO ₄]	[DMEIm][H ₂ PO ₄]	5:5	CH ₃ CN	-	-	70 at 120 °C	-	[27]
PVdF-HFP ($M_n = 100000$)	-	[EMIm][TFSI]	6:4	MP	80	Overnight	10 at	-	[28]
		[(RIm][TFSI)]	8:2 and 4:6				140 °C		
PVdF-HFP ($M_n = 100000$)	H[TfO]	[DMPIm][TFSI]	7.7:2(:0.3)	-	130 and RT	Repeated several times	20 at 100 °C	-	[29]
PVdF-HFP ($M_n = 130000$)	-	[BMIm][TfO]	6:4	Acetone	RT	48	15 at 140 °C	0.6 at 140 °C	[30]
		[Elm][TfO]					6 at 140 °C	0.1 at 140 °C	

Cation:

DMPIm = 1,2-dimethyl-3-*n*-propylimidazolium, DMOIm = 2,3-dimethyl-1-octylimidazolium, DMEIm =

2,3-dimethyl-1-ethylimidazolium, EMIm = 1-ethyl-3-methylimidazolium, BMIm = 1-butyl-3-methylimidazolium, Elm =

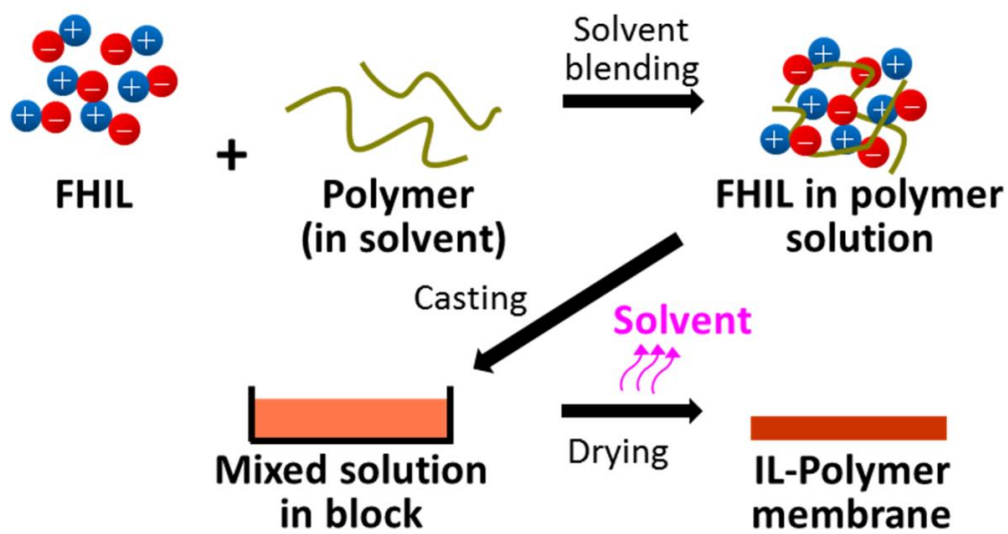
N-ethylimidazolium, MIm = *N*-methylimidazolium

Anion:

TFSI = bis(trifluoromethylsulfonyl)imide, TfO = trifluoromethylsulfonate

Solvent:

MP = 4-methyl-2-pentanone



Scheme 5-1 Preparation procedure of EMPyr(FH)_{1.7}F/PVdF-HFP composite membrane.

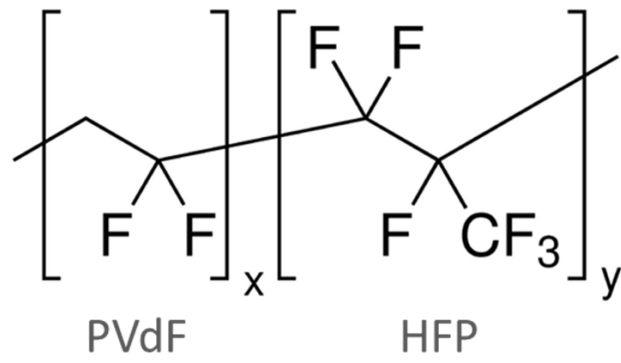


Fig. 5-1 Chemical structure of PVdF-HFP.

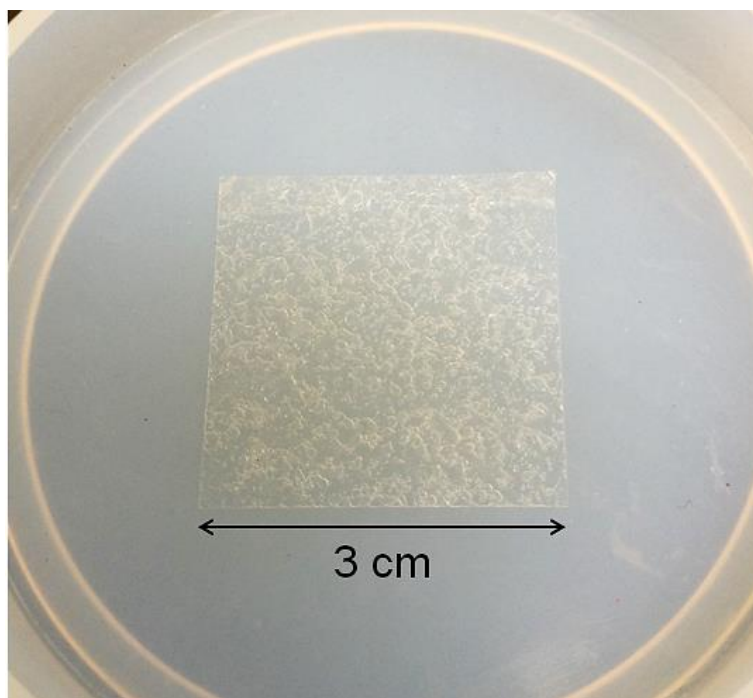


Fig. 5-2 Photograph of EMPyr(FH)_{1.7}F/PVdF-HFP (7:3) composite membrane.

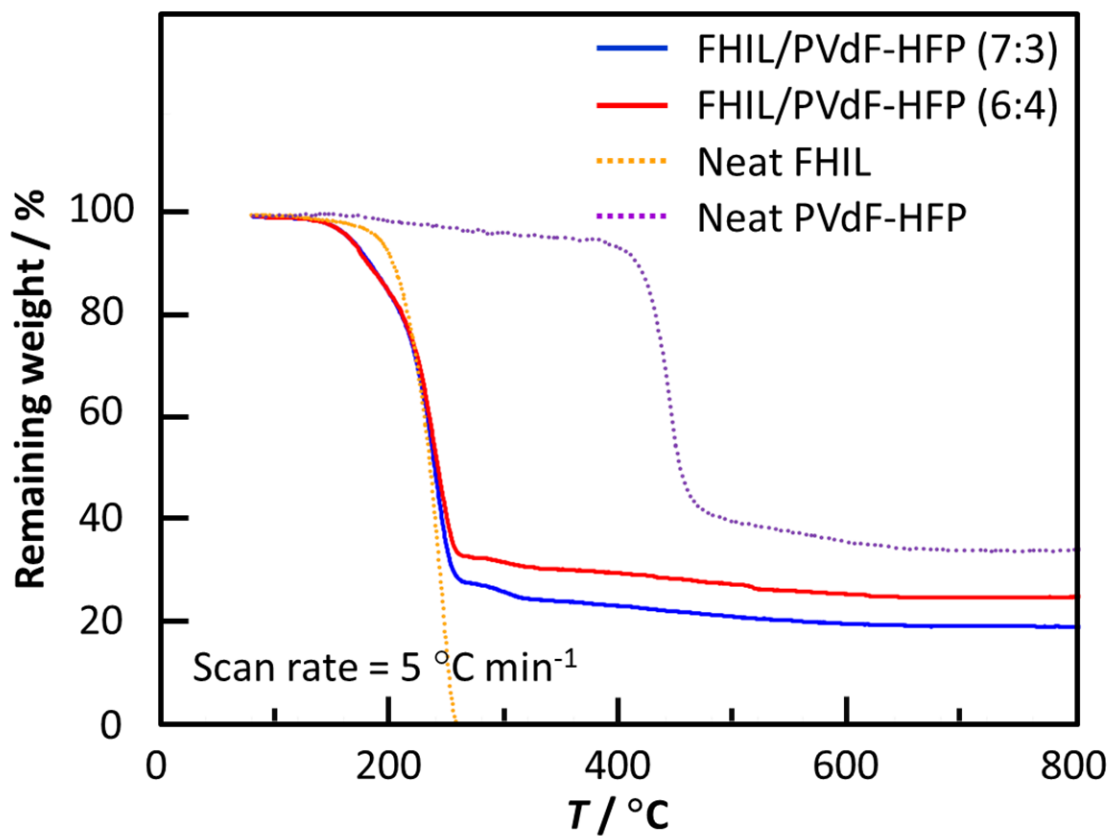


Fig. 5-3 TG curves of EMPyr(FH)_{1.7}F/PVdF-HFP (7:3 and 6:4) composite membranes, neat FHIL and neat PVdF-HFP. Scan rate: 5 °C min⁻¹.

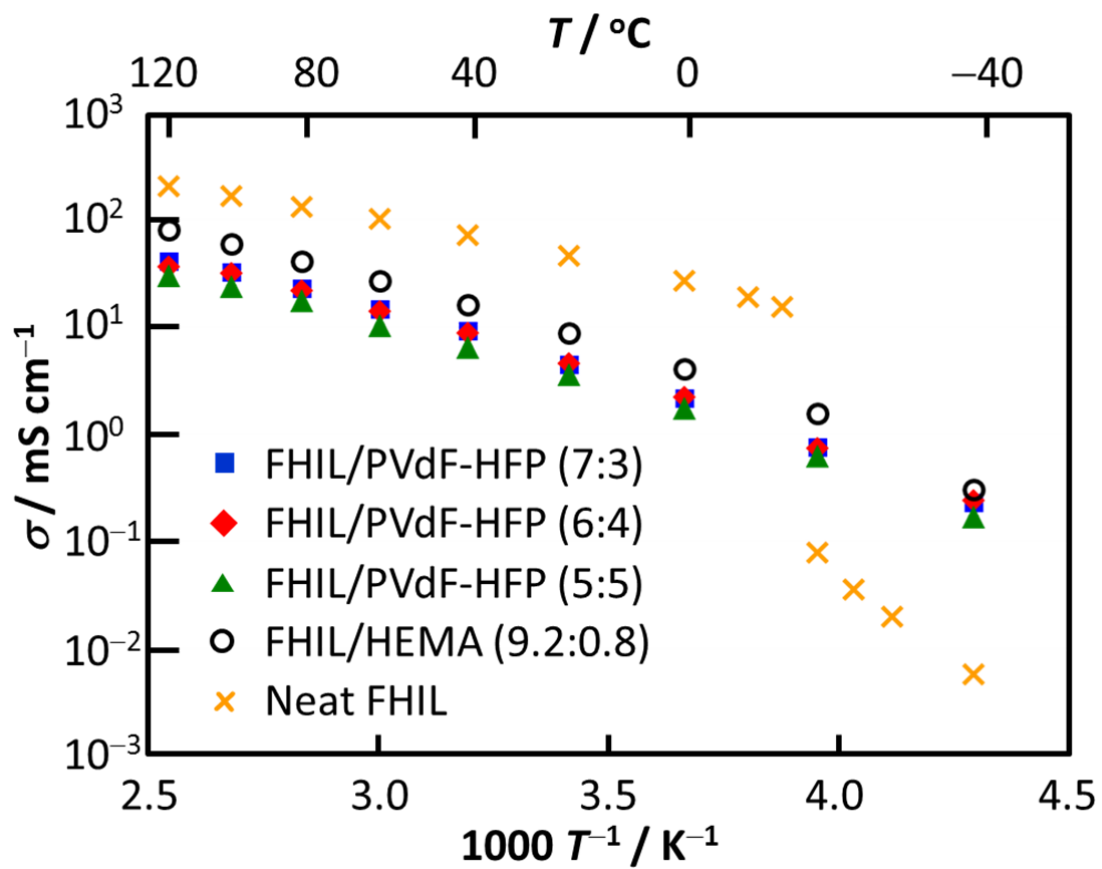


Fig. 5-4 Arrhenius plots of ionic conductivities of EMPyr(FH)_{1.7}F/PVdF-HFP (7:3, 6:4 and 5:5) composite membranes, EMPyr(FH)_{1.7}F/HEMA (9.2:0.8) composite membrane, and neat FHIL.

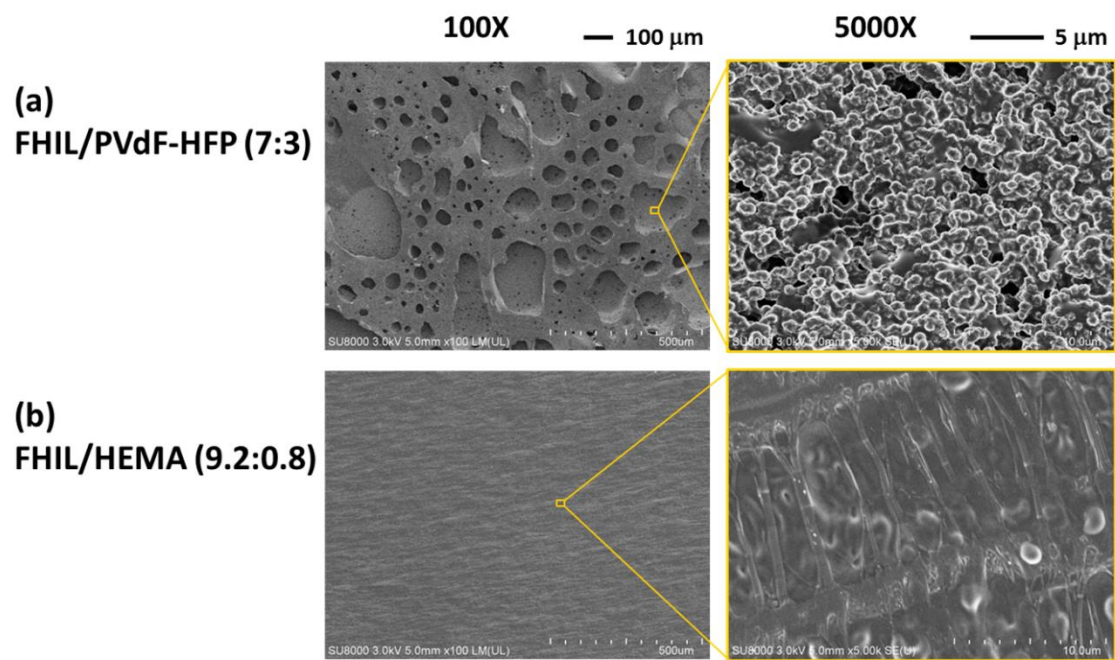


Fig. 5-5 SEM images of (a) EMPyr(FH)_{1.7}F/PVdF-HFP (7:3) composite membrane and (b) EMPyr(FH)_{1.7}F/HEMA (9.2:0.8) composite membrane.

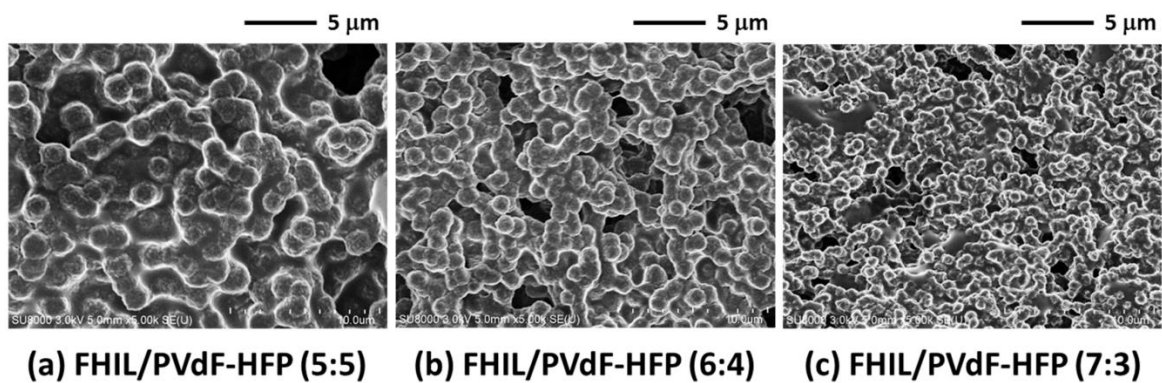


Fig. 5-6 SEM images of EMPyr(FH)_{1.7}F/PVdF-HFP composite membranes with the FHIL:polymer weight ratio of (a) 7:3, (b) 6:4, and (c) 5:5.

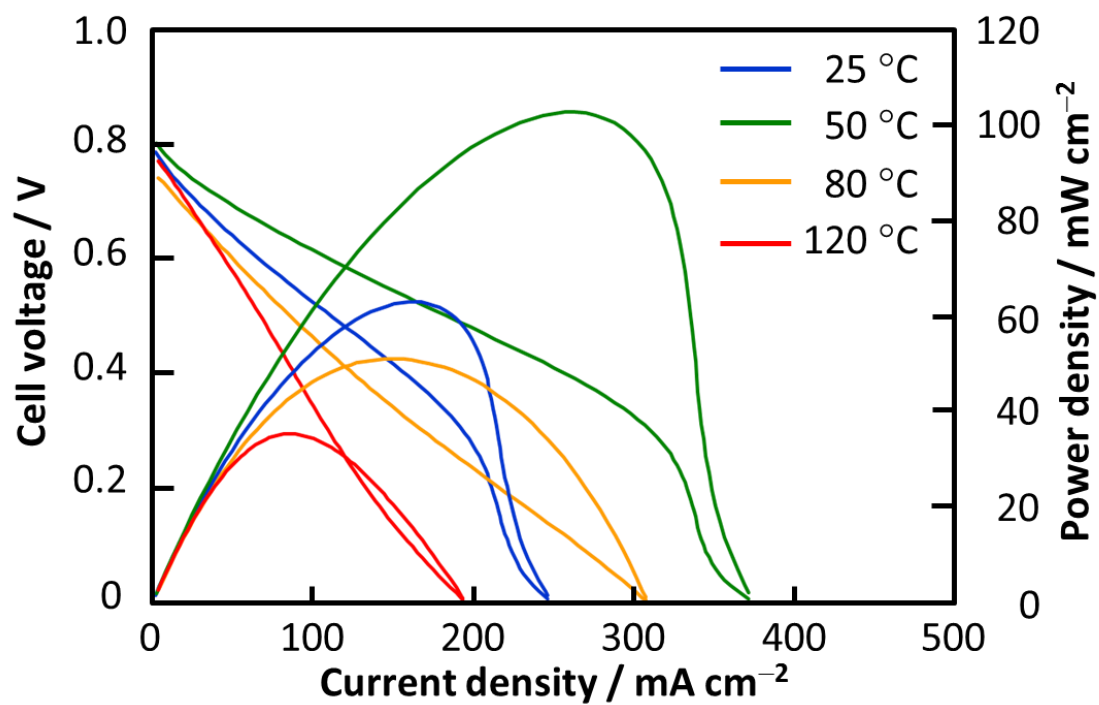


Fig. 5-7 i - V and i - P characteristic curves of a single cell using EMPyr(FH)_{1.7}F/PVdF-HFP (7:3) composite membrane at 25–120 °C under nonhumidified conditions. Anode and cathode catalyst: 1.0 mg Pt cm⁻².

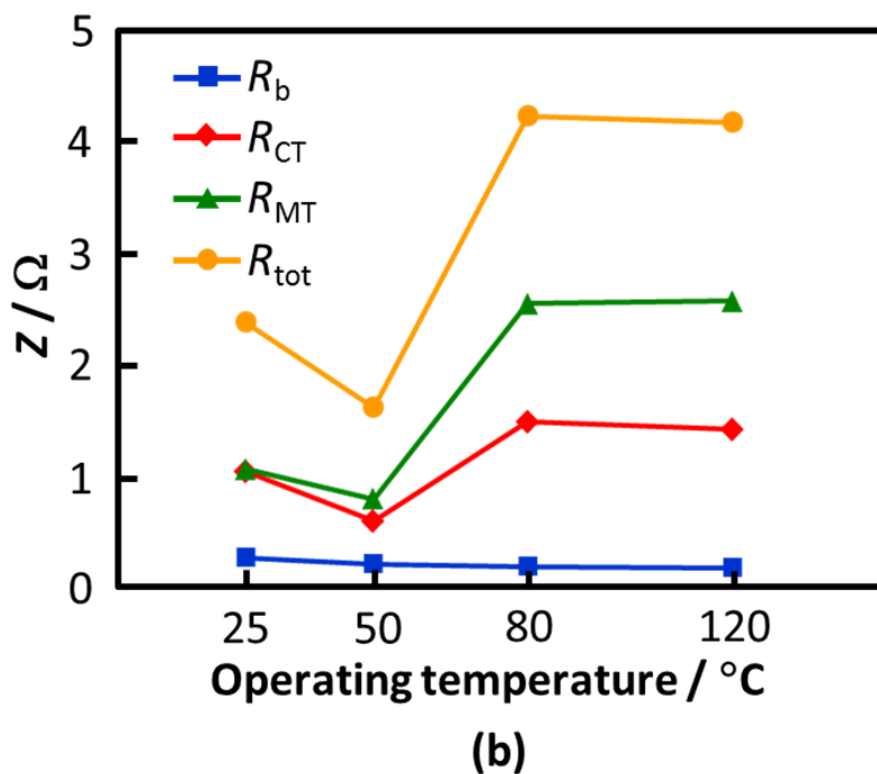
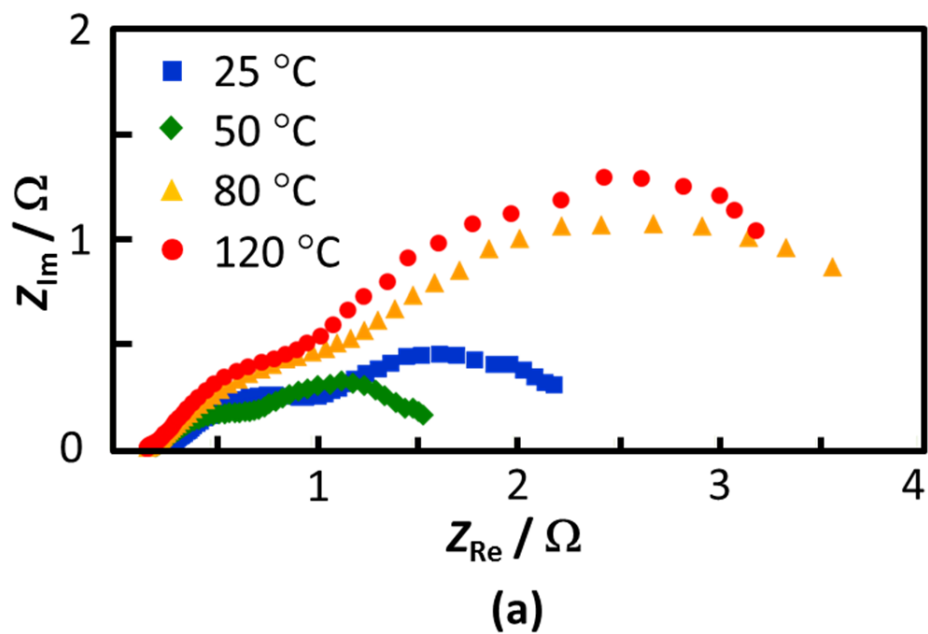
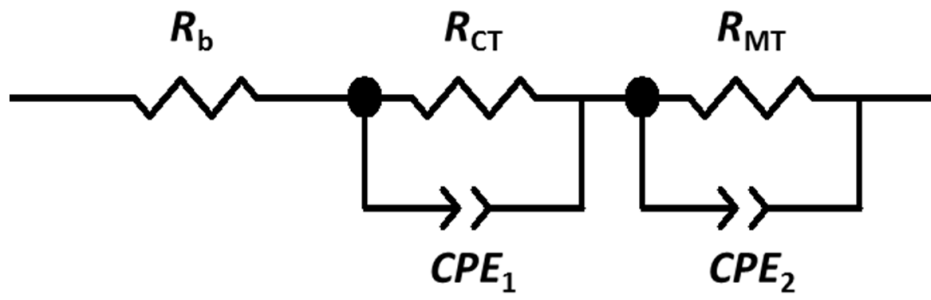


Fig. 5-8 (a) Nyquist plots of a single cell using EMPyr(FH)_{1.7}F/PVdF-HFP (7:3) composite membrane, operated from 25 to 120 °C under nonhumidified conditions and (b) temperature dependence of bulk resistance (R_b), charge transfer resistance (R_{CT}), mass transfer resistance (R_{MT}) and total resistance (R_{tot}).



R: resistance, CPE: constant phase element
 Total resistance, $R_{tot} = R_b + R_{CT} + R_{MT}$

Fig. 5-9 Equivalent circuit used in this chapter.

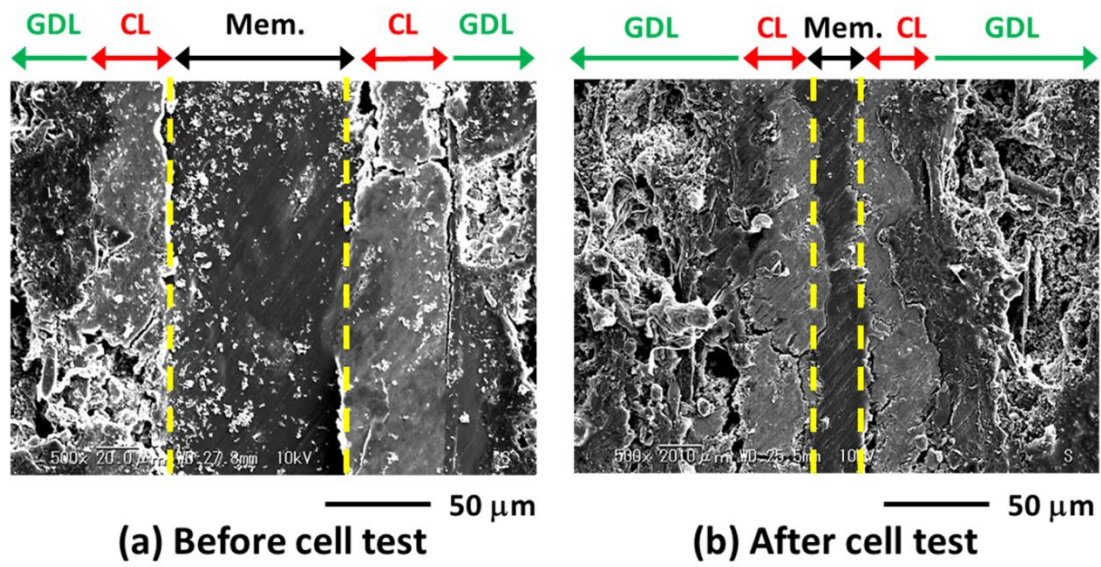


Fig. 5-10 Cross-sectional SEM images of the MEAs using EMPyr(FH)_{1.7}F/PVdF-HFP (7:3) composite membrane (a) before and (b) after cell test at 25–120 °C. (GDL = gas diffusion layer, CL = catalyst layer, Mem. = membrane)

Chapter 6

Influence of cationic structures on oxygen reduction reaction at Pt electrode in fluorohydrogenate ionic liquids

6.1 Introduction

As previously described in section 1.4 of chapter 1, fluorohydrogenate fuel cells (FHFCs) are fuel cells using FHILs as the electrolytes to generate electrical power through the process of fluorohydrogenate anion conduction [1]. Since FHFCs are not based on the conventional proton conduction mechanism that takes place in the presence of water, they do not require humidification. This enables them to operate at higher temperatures.

In the first report on FHFCs, EMIm(FH)_{*n*}F (EMIm⁺: 1-ethyl-3-methyl imidazolium, *n* = 1.3 and 2.3), was used as an electrolyte [1]. FHFCs that use composite membranes consisting of EMIm(FH)_{1.3}F and polymers demonstrate a power density of 20.2 mW cm⁻² at 393 K [2]. Recently, FHFCs using *N*-ethyl-*N*-methyl pyrrolidinium fluorohydrogenate (EMPyr(FH)_{1.7}F) have also been studied, and have exhibited a maximum cell performance of 32 mW cm⁻² [3]. FHFCs are promising as a new type of fuel cell capable of operating at intermediate temperatures without humidification. However, the cathodic overpotential is larger than the anodic overpotential for FHFCs, similar to the other conventional fuel cells [4–5]. The higher rate of the oxygen reduction reaction (ORR) is crucial for the improvement of cell performance. It was found that EMPyr(FH)_{*n*}F exhibited a higher ORR activity on the Pt electrode than did the EMIm(FH)_{*n*}F [5], the reason for this higher activity has not yet been clarified.

In this chapter, the influence of the cationic structures on the ORR parameters in FHILs has been evaluated at 298 K. The FHILs used in this study were EMIm(FH)_{1.3}F, EMIm(FH)_{2.3}F, EMPyr(FH)_{1.7}F, EMPyr(FH)_{2.3}F, trimethylsulfonium fluorohydrogenate (S₁₁₁(FH)_{1.9}F), triethyl-*n*-pentylphosphonium fluorohydrogenate (P₂₂₂₅(FH)_{2.1}F), and 5-azoniaspiro[4.4]nonane fluorohydrogenate (AS[4.4](FH)_{2.0}F). The structures and physicochemical properties [3–10] of the FHILs used in this study are summarized in Fig. 6-1 and Table 6-1, respectively. The following ORR parameters were determined on a Pt electrode; (1) kinetically limited current density (j_k), which corresponds to the rate of ORR in the absence of any mass-transfer effects, (2) yield of H₂O₂ ($X_{H_2O_2}$) on Pt, which is the ratio of the H₂O₂ production rate to that of the overall ORR, (3) solubility (C) and diffusion coefficient (D) of oxygen in the FHILs, which correlate with the O₂ transfer ability.

6.2 Experimental

6.2.1 Preparation of FHILs

The preparation of FHILs used in this study was thoroughly explained in section 2.2.1 of chapter 2. EMIm(FH)_{2.3}F and EMPyr(FH)_{2.3}F were prepared in the manner previously reported [7, 11]. An excess of anhydrous HF (Morita Chemical Industry) was distilled onto EMImCl (Yoyu Lab) or EMPyrCl (Yoyu Lab) at 77 K, followed by elimination of the unreacted HF and byproduct HCl at 298 K. EMIm(FH)_{2.3}F and EMPyr(FH)_{2.3}F were further evacuated at 393 K under reduced pressure (<1 Pa), which yielded EMIm(FH)_{1.3}F and EMPyr(FH)_{1.7}F, respectively. S₁₁₁(FH)_{1.9}F, P₂₂₂₅(FH)_{2.1}F, and AS[4.4](FH)_{2.0}F were synthesized by metathesis of the bromides and anhydrous HF (Daikin Industries, >99%), which was dried over K₂NiF₆

(Ozark Mahoning), in the same manner as for EMIm(FH)_{2,3}F and EMPyr(FH)_{2,3}F [8–10]. The addition and elimination of anhydrous HF was repeated several times in order to ensure the complete elimination of the bromide in the form of HBr.

6.2.2 Electrochemical measurement

The electrochemical measurement was explained in section 2.4 of chapter 2. A rotating electrode system (Pine Research Instrumentation) and a thermostated, three-electrode PTFE cell were used. Either a rotating disk electrode (RDE, Pine Research Instrumentation) or a rotating ring-disk electrode (RRDE, Pine Research Instrumentation) was used as the working electrode. The counter electrode was a Pt wire while the reference electrode was a reversible hydrogen electrode (RHE) made of Pt-black. About 20-30 g of each FHIL was utilized as an electrolyte. Electrochemical measurements were conducted with the aid of a potentio/galvanostat (IVIUMSTAT, Ivium Technologies). Dry hydrogen (purity >99.999%) was supplied from a hydrogen generator (HORIBA STEC, Co., Ltd) at a flow rate of 10 mL min⁻¹ and dry oxygen (Kyoto Teisan, >99.999%,) was supplied from a cylinder at the same flow rate. Prior to the electrochemical measurement, oxygen was bubbled into the cell for two hours in order to saturate the electrolyte with O₂.

6.3 Results and Discussion

6.3.1 Kinetically limited current density

Fig. 6-2 shows typical linear-sweep voltammograms for ORR on a Pt rotating disk electrode (RDE) in EMPyr(FH)_{2,3}F at 298 K. Cathodic currents increase as the rotating speed increases, while almost no currents are observed under nitrogen gas.

From the obtained data, kinetically limited current density, j_k , was calculated using the Koutecky-Levich equation as expressed below [12–15]:

$$j^{-1} = j_k^{-1} + j_d^{-1} \quad (6-1)$$

$$j_d = 0.62nFD^{2/3}C\nu^{-1/6}\omega^{1/2} \quad (6-2)$$

where j , j_d , n , F , ν , and ω denote the observed current density, diffusion-limited current density (so-called Levich current), reaction electron number, Faraday constant, kinematic viscosity (the ratio of dynamic viscosity to the electrolyte density) and the rotating speed of the disk electrode, respectively. Fig. 6-3 shows the value for j_k on a Pt electrode in EMIm(FH)_{1.3}F, EMIm(FH)_{2.3}F, EMPyr(FH)_{1.7}F, EMPyr(FH)_{2.3}F, S₁₁₁(FH)_{1.9}F, P₂₂₂₅(FH)_{2.1}F, and AS[4.4](FH)_{2.0}F at 298 K. The values of j_k at 0.7 V vs. RHE have been summarized in Table 6-2. Very small ORR currents were observed for EMIm(FH)_{1.3}F, EMIm(FH)_{2.3}F, and S₁₁₁(FH)_{1.9}F. These results can be explained as follows. The adsorbed IL on Pt surface hinders the four-electron path. Since the available four-electron path is lessened, the ORR activity significantly decreases.

The largest j_k value of 1.5 mA cm⁻² and the most positive onset potential (approximately 0.9 V vs. RHE) were observed in EMPyr(FH)_{1.7}F. This j_k value is approximately one sixth of that seen on Pt at 0.7 V vs. RHE in 0.1 M H₂SO₄ [16]. According to the study by Munakata et al. on three different protic ionic liquids based on perfluoroalkylsulfonylimides (HN(SO₂(CF₂)_{*n*}F)₂, $n = 0-2$), the ORR activity depends on the degree of ion adsorption on the electrode surface [17]. By analogy, the high ORR activity found for EMPyr(FH)_{1.7}F may result from the much weaker adsorption of

EMPy^{r+} onto the electrode.

Tafel plots of j_k in FHILs on Pt electrodes at 298 K are shown Fig. 6-4. Except for EMIm(FH)_{1.3}F, Tafel slopes range from 0.16 V to 0.20 V, as listed in Table 6-3. Since these values are larger than the well-known value of 0.12 V for ORR in protic electrolytes, further consideration is necessary for the elucidation of ORR mechanism for these FHILs. From the extrapolations of the Tafel plots to 1.23 V vs. RHE, the exchange current densities (j_0) were estimated, as shown in Table 6-3. The highest j_0 of 2.2×10^{-3} mA cm⁻² was obtained for EMPyr(FH)_{1.7}F. For EMIm(FH)_{1.3}F, it is difficult to estimate the Tafel slope and exchange current density due to the abnormal shape of the plot.

6.3.2 Yield of H₂O₂

The yield of H₂O₂ ($X_{\text{H}_2\text{O}_2}$) in the ORR was determined using the rotating ring disk electrode (RRDE) method. Steady-state disk currents at 0.2 V vs. RHE and steady-state ring currents at 1.5 V vs. RHE were measured. If H₂O₂ is produced at the disk electrode in addition to H₂O, the produced H₂O₂ is oxidized at 1.5 V. Fig. 6-5 (a) shows cyclic voltammograms on a Pt electrode in EMIm(FH)_{1.3}F with the addition of H₂O₂ from 0 to 100 mM. An oxidation of H₂O₂ was found at above 1.0 V vs. RHE, at which the current density apparently increased with the increase of H₂O₂ addition. On the other hand, addition of H₂O did not significantly affect the voltammograms as shown in Fig.6-5 (b). These results suggest that the presence of H₂O₂ in the ionic liquid electrolyte notably affects the cyclic voltammogram. The difference would be significant at a high potential region (at above 1.0 V vs. RHE in the case of EMIm(FH)_{1.3}F at 298 K).

When a disk potential becomes more negative than 0.3 V, ring currents start increasing. $X_{\text{H}_2\text{O}_2} / \%$ can be calculated from the following equations [18]:

$$X_{\text{H}_2\text{O}_2} / \% = \frac{2I_{\text{R}}/N}{I_{\text{D}} + I_{\text{R}}/N} \times 100 \quad (6-3)$$

where I_{D} , I_{R} , and N denote the disk current, the ring current, and the collection efficiency, respectively. At a disk potential of 0.2 V, $X_{\text{H}_2\text{O}_2}$ was calculated to be 8.4 %. It has been reported that strong adsorbates such as Cl^- and Br^- inhibit the four-electron reduction of O_2 to produce H_2O , while the two-electron reduction of O_2 to produce H_2O_2 also proceeds, resulting in high $X_{\text{H}_2\text{O}_2}$ values [19–21].

$X_{\text{H}_2\text{O}_2}$ values in EMIm(FH)_{2.3}F, EMPyr(FH)_{1.7}F, EMPyr(FH)_{2.3}F, P₂₂₂₅(FH)_{2.1}F, and AS[4.4](FH)_{2.0}F at the Pt electrode at 298 K were also calculated, and are given together with the value for EMIm(FH)_{1.3}F in Table 6-2. As expected from their low ORR activities, EMIm(FH)_{1.3}F and EMIm(FH)_{2.3}F showed very high $X_{\text{H}_2\text{O}_2}$ values compared with other FHILs. The $X_{\text{H}_2\text{O}_2}$ values of EMIm(FH)_{1.3}F was 8.4% and that of EMIm(FH)_{2.3}F was 21%. One possible explanation for the high $X_{\text{H}_2\text{O}_2}$ values is that the adsorption of IL on Pt surface hinders the four-electron path resulting in the low ORR activity and pushing towards the two-electron H_2O_2 path.

The $X_{\text{H}_2\text{O}_2}$ value in S₁₁₁(FH)_{1.9}F, however, cannot be determined due to a large anodic current corresponding to the decomposition of S₁₁₁(FH)_{1.9}F. Cyclic voltammograms on a Pt electrode in S₁₁₁(FH)_{1.9}F at 298 K under O_2 atmosphere is shown in Fig. 6-6. In a previous report, the anodic current was not observed in such a potential region under an inert atmosphere [9]. Hence, the electrochemical stability in the positive potential region may have been changed under the oxygen atmosphere.

Since a very small ORR current was observed in Fig. 6-6, a high $X_{\text{H}_2\text{O}_2}$ value is predicted from the same reason.

$X_{\text{H}_2\text{O}_2}$ values in EMPyr(FH)_{1.7}F, EMPyr(FH)_{2.3}F, and P₂₂₂₅(FH)_{2.1}F were around 1.5%. These values were smaller than those observed for EMIm(FH)_{1.3}F, EMIm(FH)_{2.3}F, and S₁₁₁(FH)_{1.9}F and were slightly higher than those seen for the 0.5 M aqueous solution of H₂SO₄ (<1% [18]). This means that the interaction of these cations with the Pt electrode was weak, which is consistent with the large value for j_k and the positive onset potential shown in Fig. 6-6.

6.3.3 Solubility and diffusion coefficient of oxygen

The C and D values for oxygen were determined by hydrodynamic chronocoulometry using an RDE. As a typical example, the experimental procedure and the obtained data are shown for the case of EMPyr(FH)_{2.3}F. Firstly, linear-sweep voltammograms were measured for ORR on a Pt RDE in EMPyr(FH)_{2.3}F at 298 K, as shown in Fig. 6-2. From the shapes of the voltammograms, the electrode reaction is regarded as diffusion-controlled at 0.2 V vs. RHE. Then, hydrodynamic chronocoulometry was conducted at this potential. Fig. 6-7 shows the hydrodynamic chronocoulometric curves obtained by the potential step method in which a stepwise potential was applied from the rest potential up to 0.2 V vs. RHE on a Pt RDE in EMPyr(FH)_{2.3}F at 298 K. There is a linear relationship between the charge, Q , and the time, t , in the region from 3 s to 5 s for both cases. According to Tsushima *et al.* [22], such a linear relationship can be expressed by the following equations:

$$Q = Q_{\text{intercept}} + I_d t \quad (6-4)$$

where $Q_{\text{intercept}}$ denotes the Q -intercept of the straight line, and I_d denotes the diffusion limited current, which corresponds to the gradient of the straight line. $Q_{\text{intercept}}$ and I_d are expressed by the following equations:

$$Q_{\text{intercept}} = 0.3764 nFAC \times 1.610D^{1/3}v^{1/6}\omega^{-1/2} (1 + 0.2980Sc^{-1/3} + 0.1451Sc^{-2/3}) + Q_{\text{adsorption}} \quad (6-5)$$

$$I_d = j_d A = nFADC / 1.610D^{1/3}v^{1/6}\omega^{-1/2} (1 + 0.2980Sc^{-1/3} + 0.1451Sc^{-2/3}) \quad (6-6)$$

where $Q_{\text{adsorption}}$, A , and Sc denote the charge passed in electrolysis of the adsorbed species, the disk electrode surface area, and the Schmidt number, which is re-expressed by the ratio of the kinematic viscosity to the diffusion coefficient of O_2 , respectively. The plots of j_d against $\omega^{1/2}$ and $Q_{\text{intercept}}$ against $\omega^{-1/2}$ for each FHIL are presented in Fig. 6-8 and Fig. 6-9, respectively. In both graphs, linear relationships were confirmed. In the present study, the number of electrons associated with ORR, n , was calculated from $X_{H_2O_2}$ using the following equation:

$$n = 4 \left(1 - \frac{X_{H_2O_2}}{100} \right) + 2 \frac{X_{H_2O_2}}{100} \quad (6-7)$$

The values of n are listed in Table 6-2. For $S_{111}(\text{FH})_{1.9}\text{F}$, since the $X_{H_2O_2}$ value could not be determined, the n value was unable to be calculated. Thus, it was assumed to be 4 (four electron reduction) in the calculation of C .

The plots of j_d against $\omega^{1/2}$ and $Q_{\text{intercept}}$ against $\omega^{-1/2}$ show a linear relationship.

From each gradient, the values of C and D were determined by combining eqs. 6-5 and 6-6. The C and D values for EMIm(FH)_{1.3}F, EMIm(FH)_{2.3}F, EMPyr(FH)_{1.7}F, EMPyr(FH)_{2.3}F, S₁₁₁(FH)_{1.9}F, P₂₂₂₅(FH)_{2.1}F, AS[4.4](FH)_{2.0}F are given in Table 6-2. It has been reported that the solubilities of hydrogen and oxygen in ionic liquids correlate with their free volumes [5, 23]. Assuming that oxygen occupies the free space in ionic liquids, a smaller C value should be attributable to a smaller free volume in that ionic liquid. The smallest C value in the present FHILs is observed for S₁₁₁(FH)_{1.9}F, suggesting that it has the smallest free volume, which is consistent with it having the most compact ion size of S₁₁₁⁺. On the other hand, P₂₂₂₅(FH)_{2.1}F has the most bulky cation in the series, giving it the largest free volume for these liquids. As a result, it exhibits the highest C value. The D values tend to decrease with increasing viscosity, which is typical for diffusion coefficients in ionic liquids. For comparison, the C and D values in 0.5 M H₂SO₄ [24], Nafion[®] [25], EMImBF₄ [26] and DEMATfO [27] at 298 K, and BMPyrTFSI [28] at 303 K are also given in Table 6-2. The C values obtained for the FHILs are in the region of 0.2–1.3 mmol dm⁻³ and are not much different from those for Nafion[®]. However, the D values are rather large in comparison with those in Nafion[®], which is a solid.

The reaction electron number (n) can also be calculated by substituting the obtained C and D values in eq. 6-2. For example, in the case of EMIm(FH)_{2.3}F, the n value was calculated to be 3.8 at 100 rpm. This value is not much different from the n value calculated from eq. 6-7 using the ring data (3.6).

For the application to fuel cells, too high C and D values can cause a large amount of O₂ crossover from the cathode to the anode. On the contrary, too low C and D values hinder the supply of O₂ to the cathode. In order to evaluate the amount of O₂

crossover, the current density caused by the crossover of oxygen from cathode to anode ($j_{\text{crossover}}$) has been calculated. The following assumptions were used in this calculation: (1) the electrolyte thickness is 50.8 μm , which is equal to that of the Nafion[®] 212 membrane used in the present study, and (2) the reaction of the oxygen at the anode is ORR on a Pt electrode. Firstly, the permeability of oxygen (CD) was calculated. Then, the permeation rate was obtained by dividing the permeability with the thickness of electrolyte. Finally, the crossover current was calculated by multiplying the permeation rate with $4F$. The calculated $j_{\text{crossover}}$ for FHILs, 0.5 M H_2SO_4 , Nafion[®], EMImBF₄ and DEMATfO at 298 K, and BMPyrTFSI at 303 K are listed in Table 6-2. It has been reported that a single cell using the EMPyr(FH)_{1.7}F-HEMA (9:1) composite membrane exhibited a maximum current density of 150 mA cm^{-2} [3]. This value was much larger than the value calculated for $j_{\text{crossover}}$, indicating that the crossover currents are negligible for the fuel cell applications of FHILs.

6.4 Conclusion

In this study, the ORR was investigated in an attempt to improve the performance of fluorohydrogenate fuel cells from the viewpoint of the electrolyte. The influence of different cationic species on the ORR parameters were evaluated on a Pt electrode in EMIm(FH)_{1.3}F, EMIm(FH)_{2.3}F, EMPyr(FH)_{1.7}F, EMPyr(FH)_{2.3}F, S₁₁₁(FH)_{1.9}F, P₂₂₂₅(FH)_{2.1}F, and AS[4.4](FH)_{2.0}F at 298 K. The ORR parameters were kinetically limited current density (j_k), H_2O_2 yield ($X_{\text{H}_2\text{O}_2}$), solubility (C), and diffusion coefficient (D) of oxygen. EMPyr(FH)_{1.7}F showed the largest j_k value that could be explained by the low adsorbability of the EMPyr⁺ at the Pt surface as a result of the weaker interaction between EMPyr⁺ and Pt. The $X_{\text{H}_2\text{O}_2}$ values in EMPyr(FH)_{1.7}F,

EMPy_r(FH)_{2.3}F, and P₂₂₂₅(FH)_{2.1}F were 1.6, 1.9, and 1.2%, respectively. The *C* and *D* values in these FHILs were considered to be appropriate for fuel cell application; the estimated crossover currents were small enough in comparison to the currents in practical use.

References

- [1] R. Hagiwara, T. Nohira, K. Matsumoto, Y. Tamba, *Electrochem. Solid-State Lett.* **8** (2005) A231.
- [2] J. S. Lee, T. Nohira, R. Hagiwara, *J. Power Sources* **171** (2007) 535.
- [3] P. Kiatkittikul, T. Nohira, R. Hagiwara, *J. Power Sources* **220** (2012) 10.
- [4] T. Hayashida, *Master thesis of Kyoto University* (2009).
- [5] Y. Tani, T. Nohira, T. Enomoto, K. Matsumoto, R. Hagiwara, *Electrochim. Acta* **56** (2011) 3852.
- [6] R. Hagiwara, K. Matsumoto, Y. Nakamori, T. Tsuda, Y. Ito, H. Matsumoto, K. Momota, *J. Electrochem. Soc.* **150** (2003) D195.
- [7] K. Matsumoto, R. Hagiwara, Y. Ito, *Electrochem. Solid-State Lett.* **7** (2004) E41.
- [8] T. Enomoto, S. Kanematsu, K. Tsunashima, K. Matsumoto, R. Hagiwara, *Phys. Chem. Chem. Phys.*, **13** (2011) 12536.
- [9] R. Taniki, K. Matsumoto, R. Hagiwara, *Electrochem. Solid-State Lett.* **15** (2012) F13.
- [10] R. Taniki, K. Matsumoto, R. Hagiwara, *Chem. Lett.* **42** (2013) 1469.
- [11] R. Hagiwara, T. Hirashige, T. Tsuda, Y. Ito, *J. Electrochem. Soc.* **149** (2002) D1.
- [12] A. J. Bard, L. R. Faulkner, *Electrochemical Methods, Fundamentals and Applications (2nd ed.)*, John Wiley & Sons, New York, 2001, pp. 331.
- [13] B. N. Ferdousi, Md. M. Islam, T. Okajima, T. Ohsaka, *Electrochim. Acta* **53** (2007) 968.
- [14] R. Baker, D. Wilkinson, J. Zhang, *ECS Trans.* **16** (2009) 43.
- [15] J. Gonzalez, C. Real, L. Hoyos, R. Miranda, F. Cervantes, *J. Electroanal. Chem.* **651** (2011) 150.

- [16]R. Halseid, T. Bystron, R. Tunold, *Electrochim. Acta.* **51** (2006) 5737.
- [17]H. Munakata, T. Tashita, M. Haibara, K. Kanamura, *ECS Trans.* **33** (2010) 463.
- [18]U. A. Paulus, T. J. Schmidt, H. A. Gasteiger, R. J. Behm, *J. Electroanal. Chem.* **495** (2001) 134.
- [19]N. M. Markovic, H. A. Gasteiger, B. N. Grgur, P. N. Ross, *J. Electroanal. Chem.* **157** (1999) 467.
- [20]M. Stamenkovic, N. M. Markovic, P. N. Ross Jr., *J. Electroanal. Chem.* **500** (2001) 44.
- [21]M. D. Maciá, J. M. Campiña, E. Herrero, J. M. Feliu, *J. Electroanal. Chem.* **564** (2004) 141.
- [22]M. Tsushima, K. Tokuda, T. Ohsaka, *Anal. Chem.* **66** (1994) 4551.
- [23]R. Fukuta, Y. Katayama, T. Miura, *ECS Trans.* **3** (2007) 567.
- [24]S. Gottesfeld, I. D. Raistrick, S. Srinivasan, *J. Electrochem. Soc.* **134** (1987) 1455.
- [25]V. A. Sethuraman, S. Khan, J. S. Jur, A. T. Haug, J. W. Weidner, *Electrochim. Acta* **54** (2009) 6850.
- [26]Y. Katayama, H. Onodera, M. Yamagata, T. Miura, *J. Electrochem. Soc.* **151** (2004) A59.
- [27]L. Johnson, A. Ejigu, P. Licence, D. A. Walsh, *J. Phys. Chem. C* **116** (2012) 18048.
- [28]S. Monaco, A. M. Arangio, F. Soavi, M. Mastragostino, E. Paillard, S Passerini, *J. Electrochim. Acta* **83** (2012) 94.

Table 6-1 Density (ρ), viscosity (η), and conductivity (σ) of EMIm(FH)_{1.3}F, EMIm(FH)_{2.3}F, EMPyr(FH)_{1.7}F, EMPyr(FH)_{2.3}F, S₁₁₁(FH)_{1.9}F, P₂₂₂₅(FH)_{2.1}F and AS[4.4](FH)_{2.0}F at 298 K.

	$\rho / \text{g cm}^{-3}$	η / cP	$\sigma / \text{mS cm}^{-1}$	Ref.
EMIm(FH) _{1.3} F	1.17	12	33.4	[4]
EMIm(FH) _{2.3} F	1.13	4.9	100	[6]
EMPy(FH) _{1.7} F	1.07	25	46.7	[3, 5]
EMPy(FH) _{2.3} F	1.07	12	74.6	[7]
S ₁₁₁ (FH) _{1.9} F	1.18	7.8	131	[9]
P ₂₂₂₅ (FH) _{2.1} F	0.999	28	12.4	[8]
AS[4.4](FH) _{2.0} F	1.13	16	82.1	[10]

Table 6-2 Kinetically limited current density (j_k), yield of H_2O_2 on Pt ($X_{H_2O_2}$), number of electrons associated with ORR (n), solubility (C) and diffusion coefficient (D) of oxygen, and the current density caused by oxygen crossover ($j_{crossover}$) of EMIm(FH)_{1.3}F, EMIm(FH)_{2.3}F, EMPyr(FH)_{1.7}F, EMPyr(FH)_{2.3}F, S₁₁₁(FH)_{1.9}F, P₂₂₂₅(FH)_{2.1}F, AS[4.4](FH)_{2.0}F, 0.1 M H₂SO₄, 0.5 M H₂SO₄, Nafion[®], EMImBF₄ and DEMATfO at 298 K, and BMPyrTFSI at 303 K.

	$ j_k ^a$ / mA cm ⁻²	$X_{H_2O_2}^b$ / %	n^b	C / mmol dm ⁻³	$10^6 D$ / cm ² s ⁻¹	$j_{crossover}^c$ / mA cm ⁻²	Refs.
EMIm(FH) _{1.3} F	-	6.4	3.9	0.48	11	0.39	[4]
EMIm(FH) _{2.3} F	-	21	3.6	0.48	33	1.1	This study
EMPyR(FH) _{1.7} F	1.5	1.6	4.0	0.58	16	0.49	This study
EMPyR(FH) _{2.3} F	0.38	1.9	4.0	0.83	24	1.5	This study
S ₁₁₁ (FH) _{1.9} F	-	-	-	0.23	25	0.46	This study
P ₂₂₂₅ (FH) _{2.1} F	0.033	1.2	4.0	1.3	13	1.2	This study
AS[4.4](FH) _{2.0} F	0.027	2.7	3.9	0.51	32	1.3	This study
0.1 M H ₂ SO ₄	9.8	-	-	-	-	-	[17]
0.5 M H ₂ SO ₄	-	< 1	-	1.1	18	1.5	[18, 24]
Nafion ^{® d}	-	-	-	1.4	0.58	0.063	[25]
EMImBF ₄	-	-	-	1.1	17	0.41	[26]
DEMATfO	-	-	-	1.79	11	1.5	[27]
BMPyrTFSI ^e	0.82	-	-	2.9	12	2.6	[28]

^a At 0.7 V vs. RHE.

^b At 0.2 V vs. RHE.

^c The electrolyte thickness is assumed to be 50.8 μm.

^d Original data was measured for Nafion[®] 117 (177.8 μm) immersed in water.

^e At 303 K.

Table 6-3 Tafel slope and exchange current density (j_0) in EMIIm(FH)_{1.3}F, EMIIm(FH)_{2.3}F, EMPyr(FH)_{1.7}F, EMPyr(FH)_{2.3}F, S₁₁₁(FH)_{1.9}F, P₂₂₂₅(FH)_{2.1}F and AS[4,4](FH)_{2.0}F on Pt electrodes at 298 K.

	Tafel slope / V	j_0 / mA cm ⁻²
EMIIm(FH) _{1.3} F	-	-
EMIIm(FH) _{2.3} F	0.18	5.3×10^{-6}
EMPyrr(FH) _{1.7} F	0.18	2.2×10^{-3}
EMPyrr(FH) _{2.3} F	0.20	1.2×10^{-3}
S ₁₁₁ (FH) _{1.9} F	0.18	2.7×10^{-6}
P ₂₂₂₅ (FH) _{2.1} F	0.17	3.6×10^{-5}
AS[4,4](FH) _{2.0} F	0.16	3.0×10^{-5}

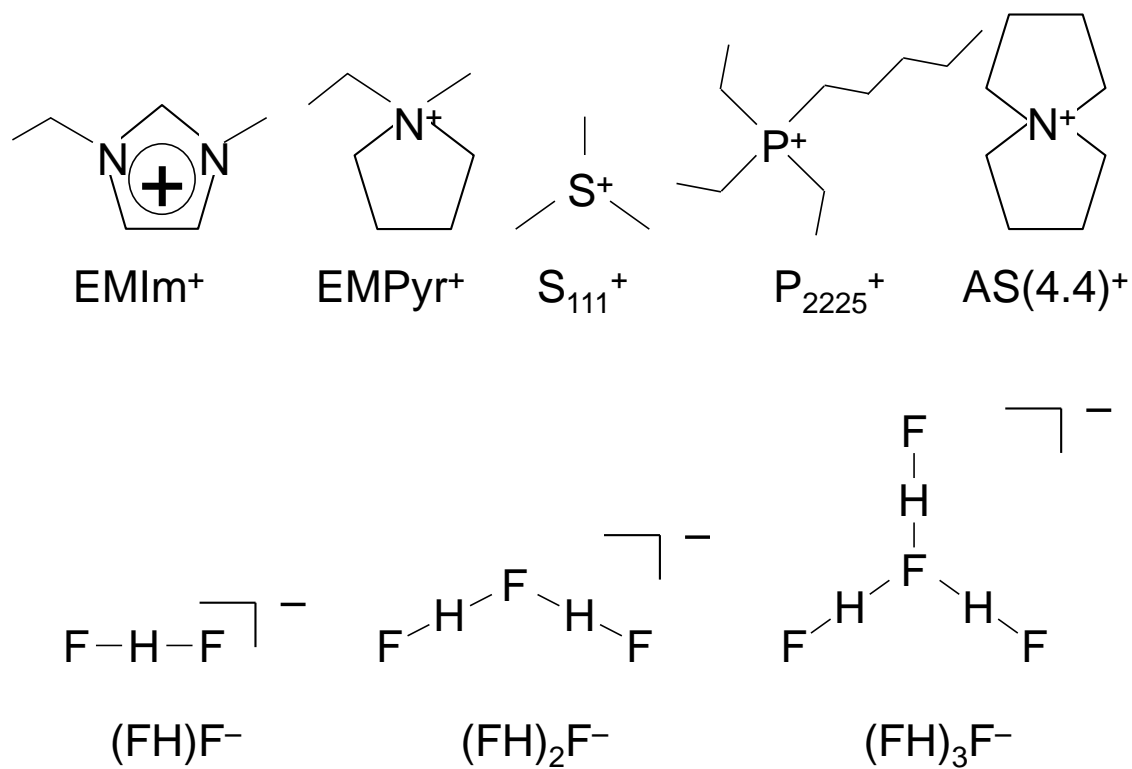


Fig. 6-1 Structures of the cations and fluorohydrogenate anions of FHILs used in this study.

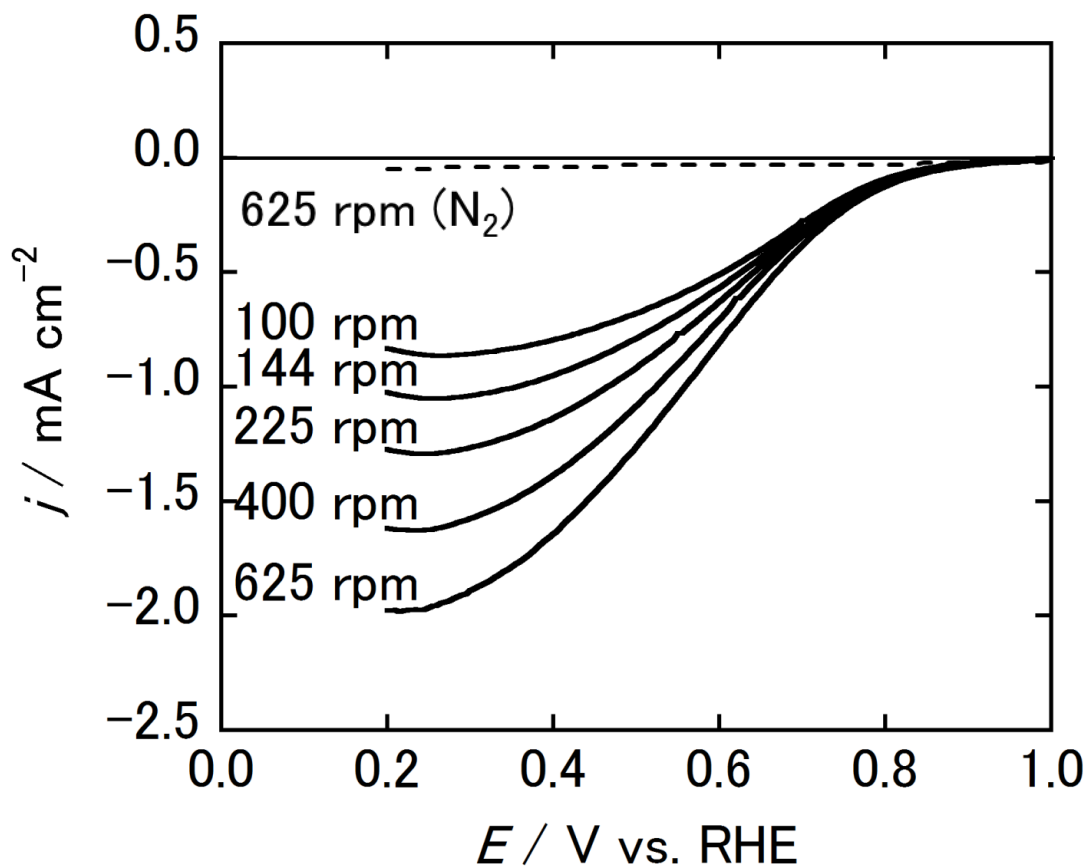


Fig. 6-2 Linear-sweep voltammograms for ORR on a Pt RDE in EMPyr(FH)_{2,3}F at 298 K. Scan rate = 10 mV s^{-1} . Rotating speed = 100–625 rpm. For comparison, the result under nitrogen atmosphere at 625 rpm is also plotted with a dashed line.

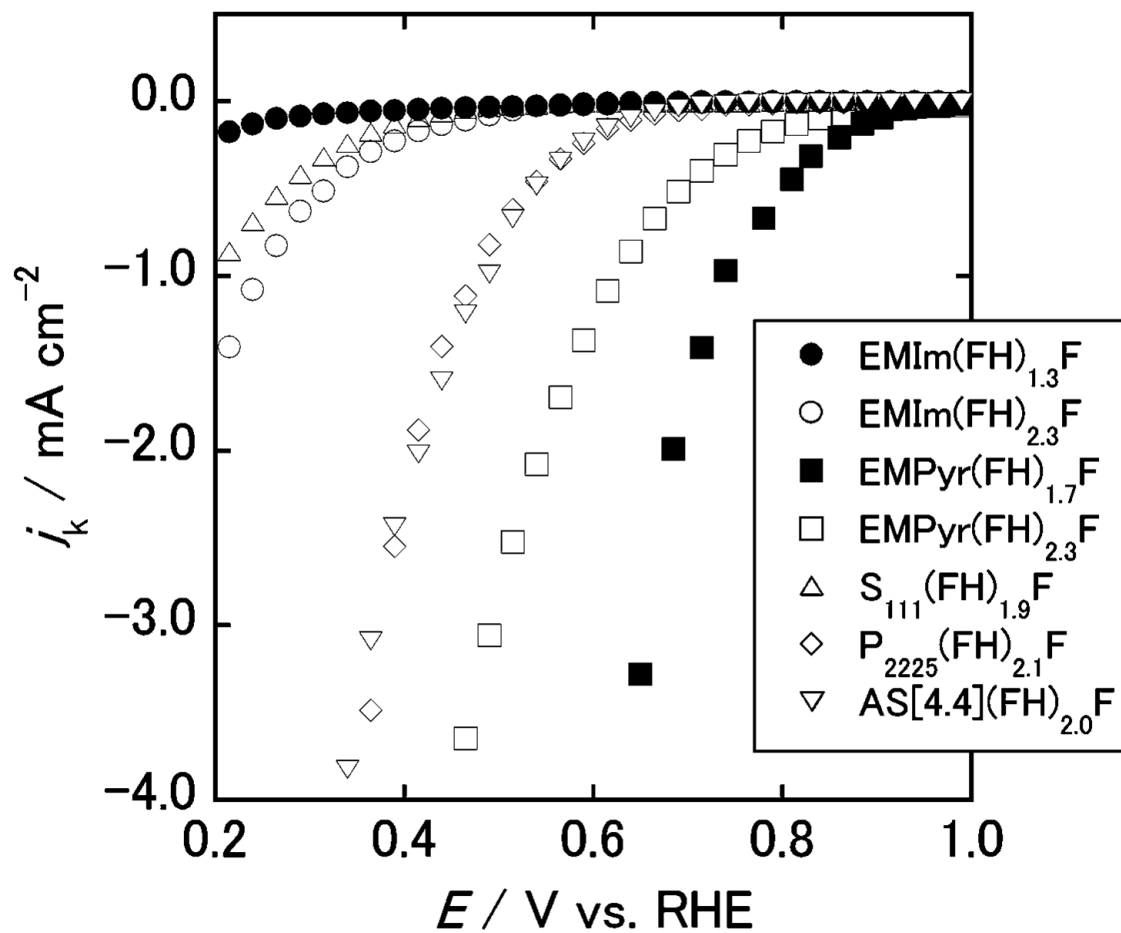


Fig. 6-3 Kinetically limited current densities of ORR (j_k) in EMIm(FH)_{1.3}F (●), EMIm(FH)_{2.3}F (○), EMPyr(FH)_{1.7}F (■), EMPyr(FH)_{2.3}F (□), S₁₁₁(FH)_{1.9}F (△), P₂₂₂₅(FH)_{2.1}F (◇) and AS[4.4](FH)_{2.0}F (▽) on Pt electrodes at 298 K.

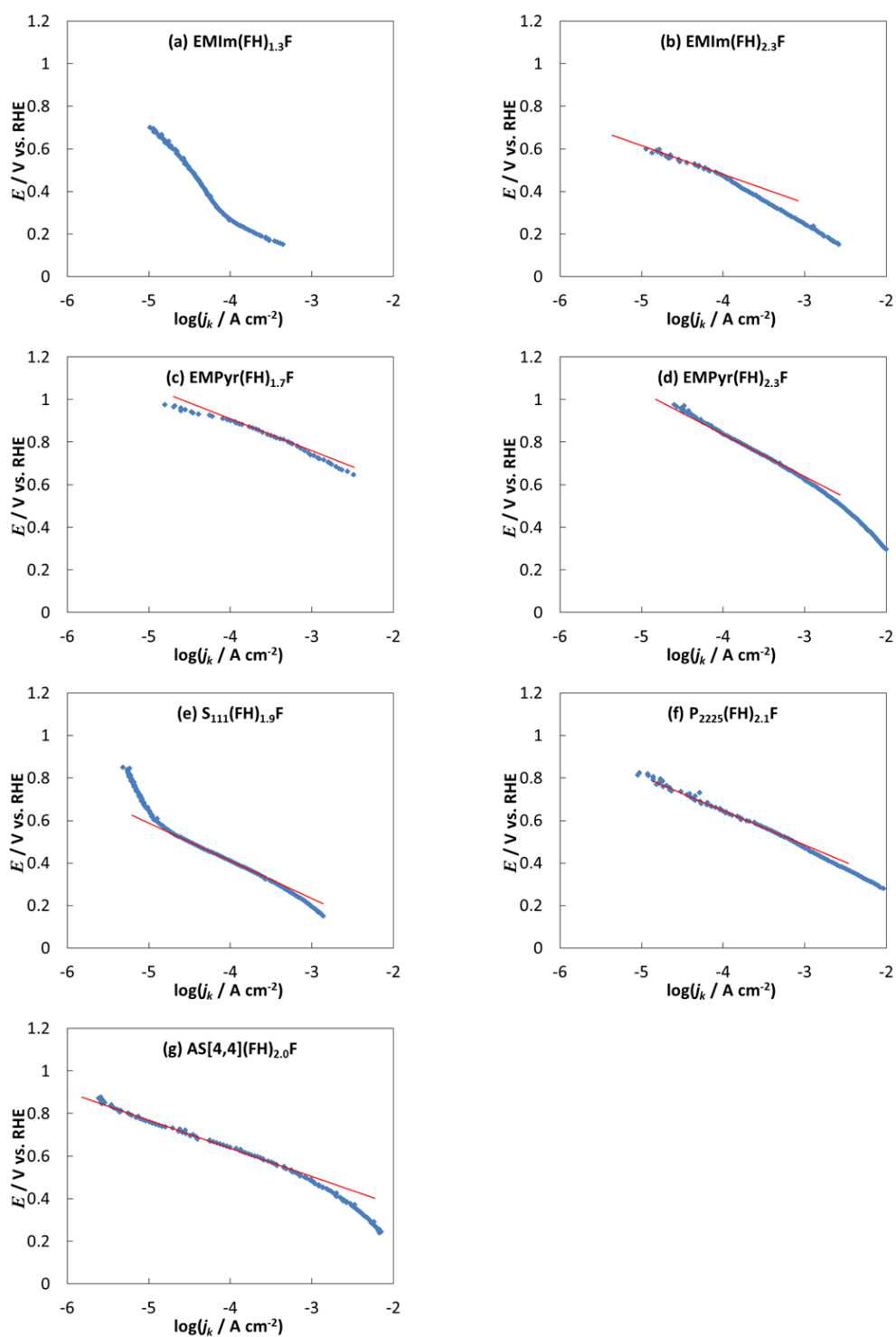
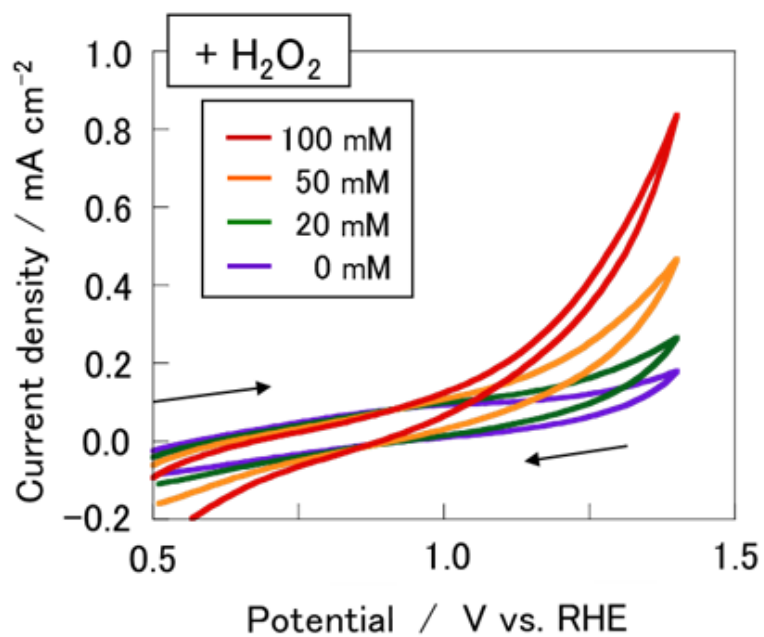
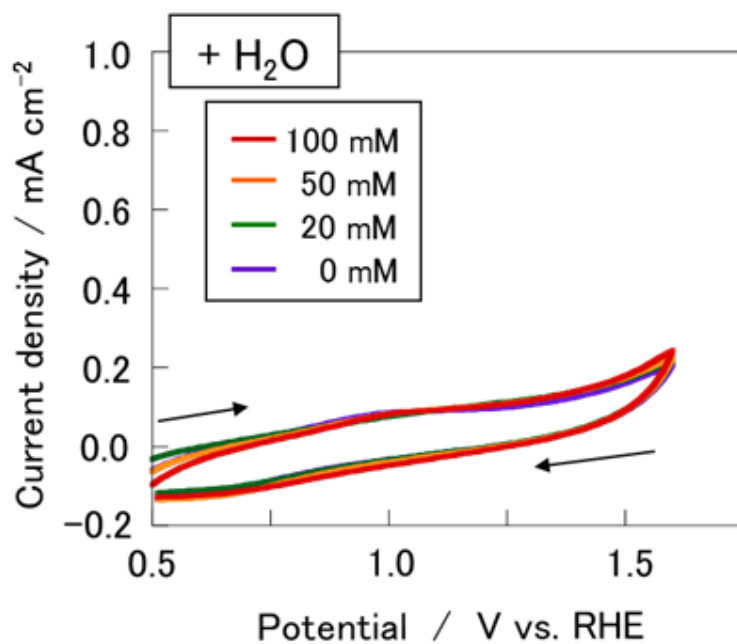


Fig. 6-4 Tafel plots of kinetically limited current densities of ORR (j_k) in (a) EMIm(FH)_{1.3}F, (b) EMIm(FH)_{2.3}F, (c) EMPyr(FH)_{1.7}F, (d) EMPyr(FH)_{2.3}F, (e) S₁₁₁(FH)_{1.9}F, (f) P₂₂₂₅(FH)_{2.1}F and (g) AS[4,4](FH)_{2.0}F on Pt electrodes at 298 K. Red-line represents the Tafel slope.



(a)



(b)

Fig. 6-5 Cyclic voltammograms on a Pt electrode in EMIm(FH)_{1.3}F with the addition of (a) H₂O₂ and (b) H₂O at 298 K. Scan rate = 10 mV s⁻¹.

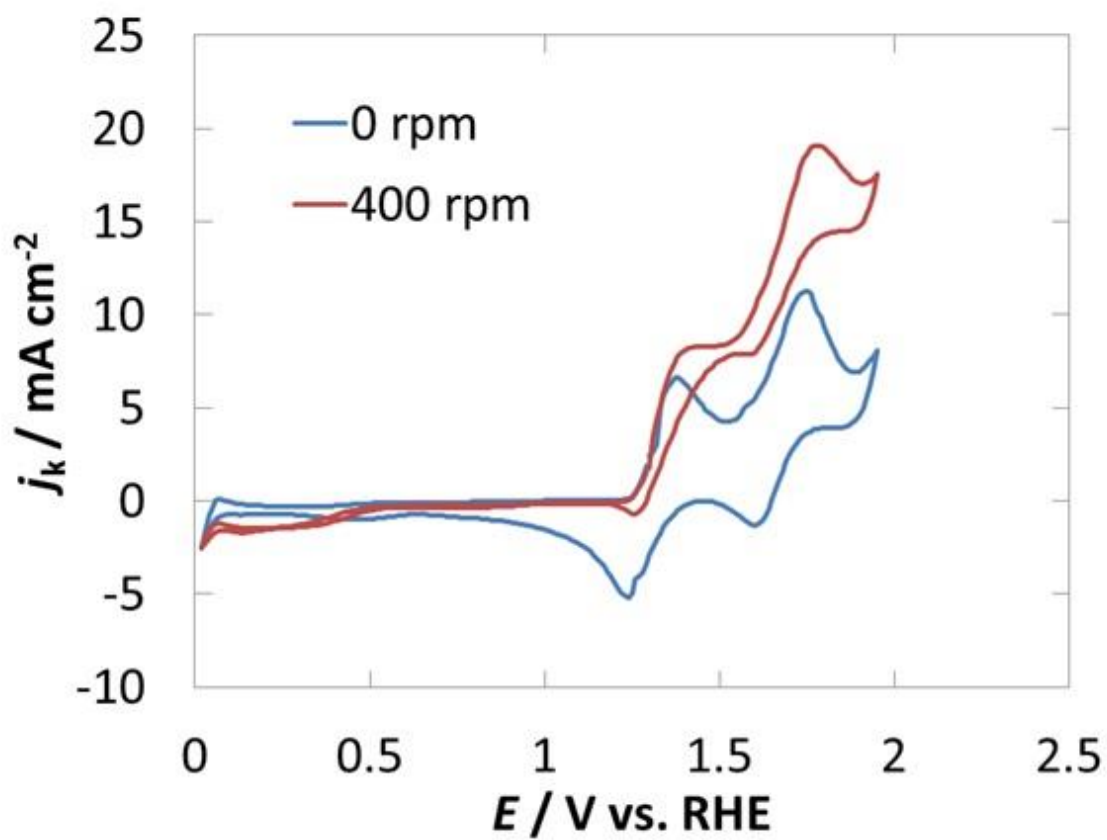


Fig. 6-6 Cyclic voltammograms on a Pt electrode in $\text{S}_{111}(\text{FH})_{1.9}\text{F}$ at 298 K under O_2 atmosphere. Rotating speed = 0 and 400 rpm. Scan rate = 10 mV s^{-1} .

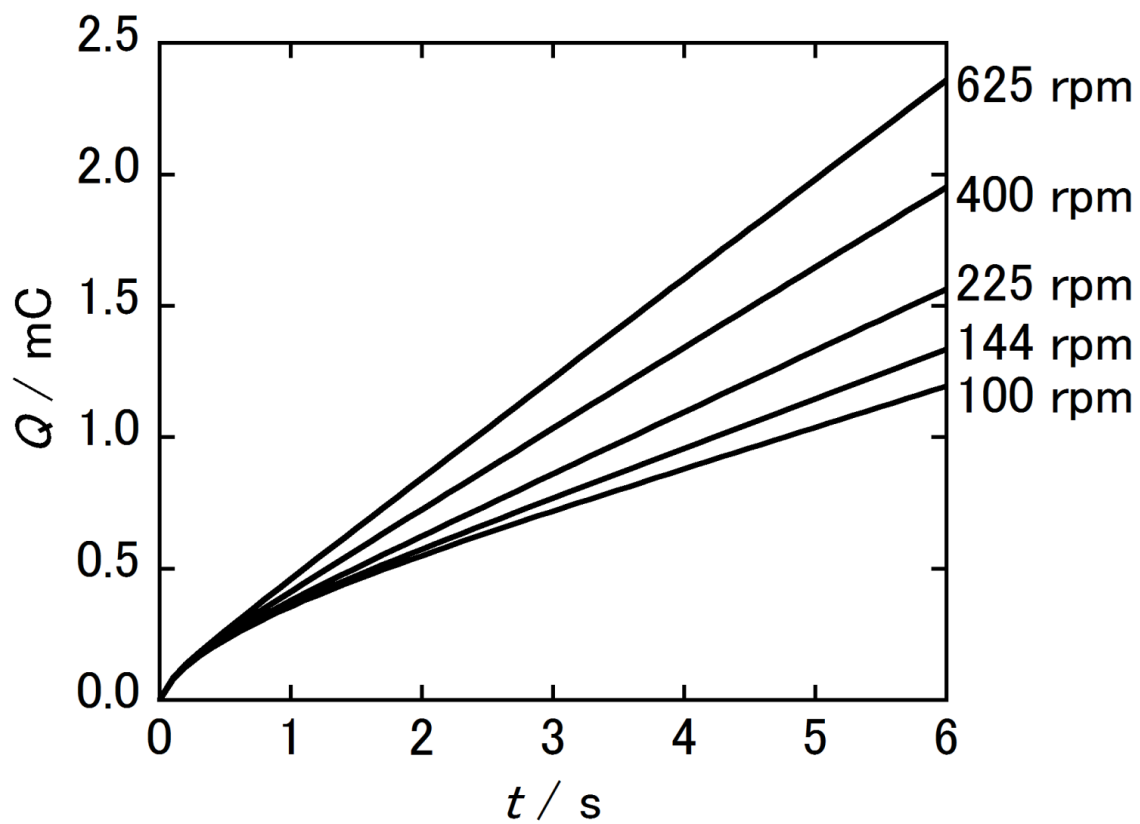


Fig. 6-7 Hydrodynamic chronocoulometric responses for ORR on a Pt RDE in EMPyr(FH)_{2.3}F at 0.2 V vs. RHE at 298 K.

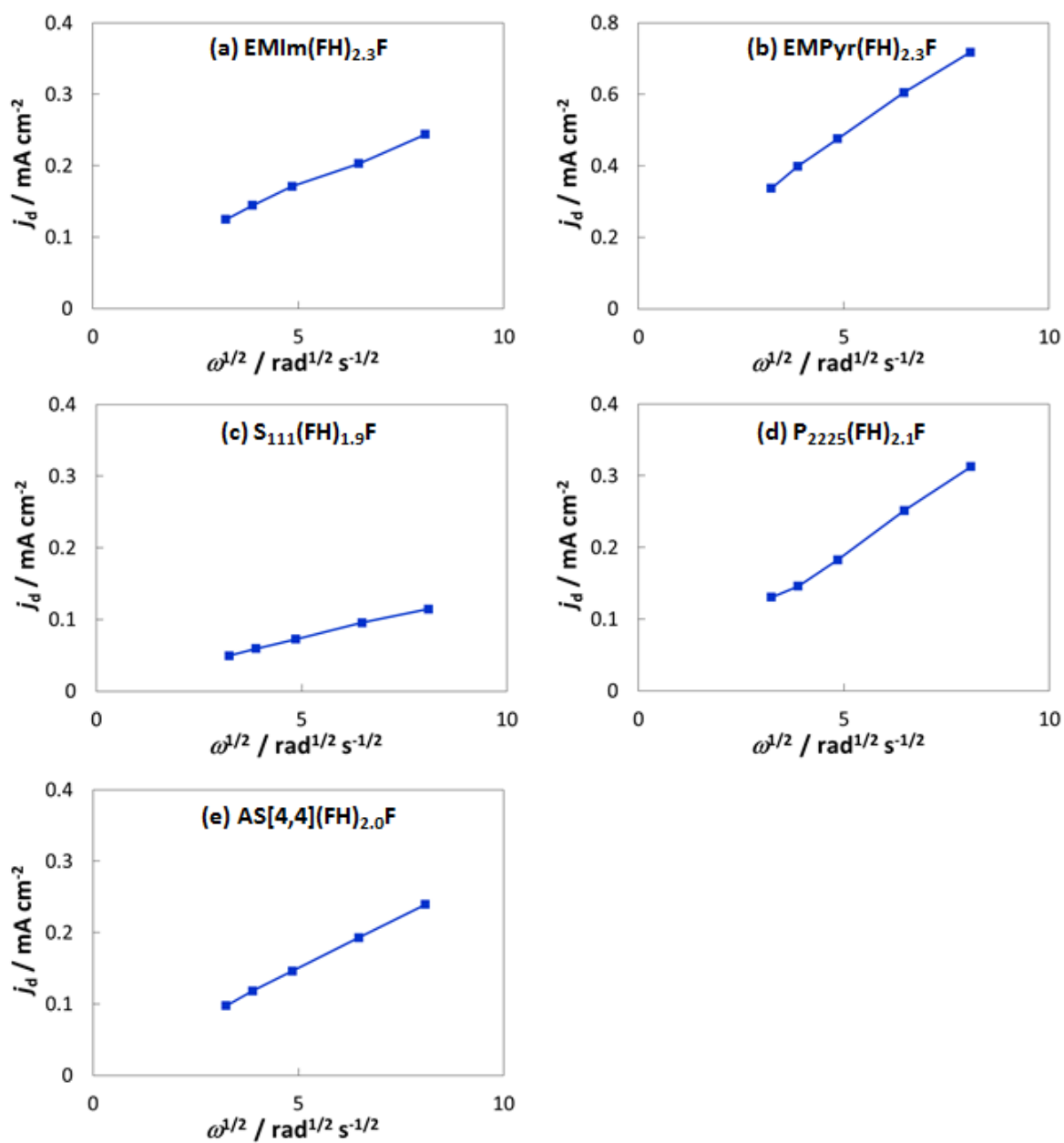


Fig. 6-8 Plots of diffusion limited current density (j_d) against square root of angular frequency ($\omega^{1/2}$) for (a) EMIm(FH)_{2.3}F, (b) EMPyr(FH)_{2.3}F, (c) S₁₁₁(FH)_{1.9}F, (d) P₂₂₂₅(FH)_{2.1}F and (e) AS[4,4](FH)_{2.0} measured at 298 K.

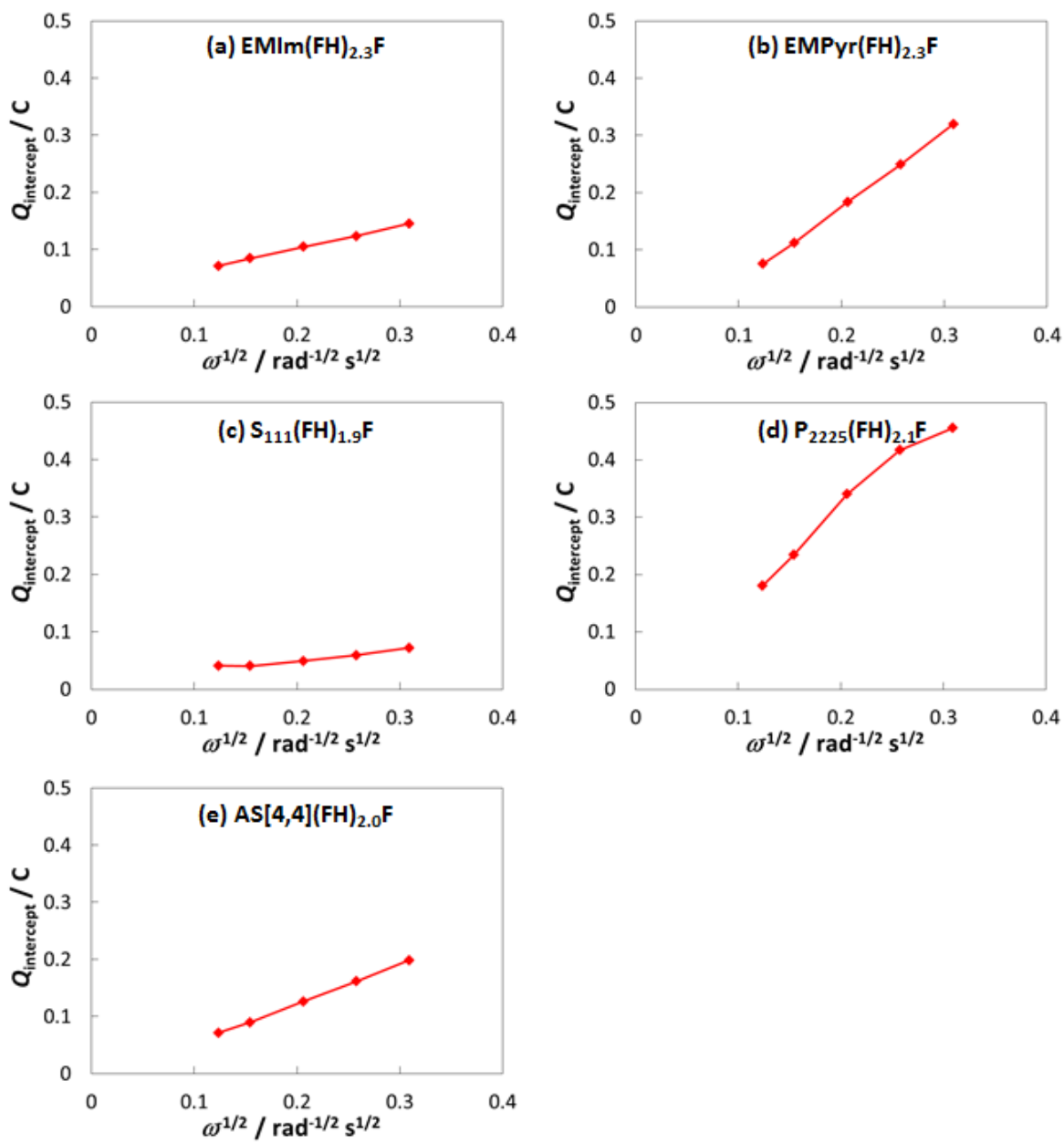


Fig. 6-9 Plots of Q -intercept of the straight line ($Q_{\text{intercept}}$) against reciprocal of square root of angular frequency ($\omega^{-1/2}$) for (a) $\text{EMIm}(\text{FH})_{2.3}\text{F}$, (b) $\text{EMPy}(\text{FH})_{2.3}\text{F}$, (c) $\text{S}_{111}(\text{FH})_{1.9}\text{F}$, (d) $\text{P}_{2225}(\text{FH})_{2.1}\text{F}$ and (e) $\text{AS}[4,4](\text{FH})_{2.0}$ measured at 298 K.

Chapter 7

Catalytic activities of Pt-M alloys (M = Fe, Co, Ni) on oxygen reduction reaction in a fluorohydrogenate ionic liquid

7.1 Introduction

The most generally used cathode catalyst for PEFCs and PAFCs is platinum. The mechanisms of ORR on Pt have been reported by many researchers, and several studies indicate that electrochemical properties of bulk Pt and those of nanoparticle Pt are different [1–6]. For example, it has been reported that the specific activity (j_s), the ratio of current to active surface area, for the ORR decreases with the decrease of crystallite diameter of Pt (d_{Pt}), especially at $d_{Pt} < 3$ nm [1–3]. This is called particle-size effect. In contrast, it has also been reported that the value of j_s depends on the inter-particle distance and/or the shape of Pt nanoparticles [4–6].

The development of cathode catalysts with smaller amount of Pt is crucial. Pt is expensive due to its scarcity of abundance in earth (*c.a.* 0.037 ppm [6]). It is so scarce that it would be depleted if vehicles in all over the world are replaced by FCVs. Many researchers have been investigated other cathode catalysts such as Pt alloy catalysts [8–19], Pt core shell catalysts [20, 21], and Pt-free catalysts [22, 23]. Among them, Pt alloy catalysts exhibited better activity for ORR than Pt in acidic solution. The enhancement of the activity of Pt by alloying has been explained by several different ways; (1) particle-size effect [7], (2) Pt-Pt interatomic distances [8], (3) leaching out of the alloying element, resulting in a rougher Pt surface with a higher atom surface density [10–12], (4) the positive core level shift derived from an increase of back-donation from

the d band of the Pt atom to the π^* orbital of the O_2 molecule helping in the easy dissociation of the O–O bond [13–17], and/or (5) the lack of affinity of OH chemisorption on the Pt in Pt alloys, resulting in the weaker OH poisoning effect on the Pt-alloy electrodes [18,19].

It is interesting to investigate the ORR activities of Pt-alloys in FHILs. The ORR on the cathode of FHFCs is not the reaction with protons but with fluorohydrogenate anions. Thus, it is conceivable that the ORR mechanism in FHILs differs from that in the conventional proton-conductive electrolytes. In other words, catalysts uniquely effective for the cathode of FHFCs may exist.

This chapter deals with the catalytic activities of Pt-alloys and the characterization by XPS and FE-SEM. As Pt-alloys, Pt-Fe, Pt-Co and Pt-Ni were employed since they have been reported to possess better specific activities than Pt in aqueous acidic solution [13, 15, 16]. Rate constants of ORR for the Pt-alloys are compared with those for Pt in EMPyr(FH)_{1.7}F at 298–333 K.

7.2 Experimental

7.2.1 Preparation of Pt alloys

Pt-alloys were prepared by a radio frequency magnetron sputtering deposition system (SVC-700 RF 2, SANYU) as shown in Fig. 7-1. A Pt disk substrate (5 mm in diameter, 5 mm thick), were polished with emery paper and buffing compound. Then, it was set on the stage together with a Si plate in the chamber. The chamber was first evacuated to 1.0×10^{-3} Pa, then, argon gas (Kyoto Teisan, > 99.999%) was introduced into the chamber up to the pressure of 5 Pa. The surface of the substrate was first etched using argon ion plasma to remove the surface oxide layer for 30 min at room

temperature. A Pt, Pt-Fe, Pt-Co, or Pt-Ni layer was deposited by sputtering deposition using Pt, PtFe, PtCo, and PtNi targets (Furuya Metal, purity 3 N), respectively, for 20 min at 573 K.

7.2.2 X-ray photoelectron spectroscopy

X-ray photoelectron spectroscopy (XPS) analysis was performed by JPS-9010 MC (JEOL) with $MgK\alpha$ radiation. Samples were fixed on carbon sheets. Before measurement, samples were etched for 20 s. The obtained peaks were corrected by C1s peak of 284.6 eV.

7.2.3 Electrochemical measurement

A rotating disk electrode (RDE) assembly (Pine Research Instrumentation) was used to estimate the activities of the Pt and Pt-alloys. Pt and Pt-alloy disks were used as the working electrodes while a Pt wire was used as the counter electrode. The reference electrode was a reversible hydrogen electrode (RHE) made of Pt wire and Pt-black. Electrochemical measurements were conducted with the aid of a potentiostat/galvanostat (IVIUMSTAT, Ivium Technologies). Dry hydrogen (purity >99.999%) was supplied from a hydrogen generator (HORIBA STEC) at a flow rate of 10 mL min⁻¹ and dry oxygen (Kyoto Teisan, >99.999%,) was supplied from a cylinder at the same flow rate. Prior to the electrochemical measurement, oxygen was bubbled into the cell for two hours in order to saturate the electrolyte.

7.2.4 Field emission scanning electron microscope

Surface images of the Pt-alloys were obtained using field emission scanning

electron microscope (FE-SEM; SU-8020, Hitachi).

7.3 Results and discussion

7.3.1 XPS analysis before electrochemical measurement

Fig. 7-2 shows XPS spectra of Pt4f_{7/2} and Pt4f_{5/2} for Pt, Pt-Fe, Pt-Co and Pt-Ni. The solid curves represent the XPS spectra before the electrochemical measurement. The compositions of the Pt alloys were calculated from the peak areas to be Pt₅₅Fe₄₅, Pt₅₀Co₅₀, and Pt₅₀Ni₅₀. For all samples, the Pt4f_{7/2} and Pt4f_{5/2} peaks shifted slightly to higher binding energies with respect to pure Pt, which indicates the formation of the alloys. It has been reported that the chemical property of Pt is strongly correlated with the average energy of their valence *d* bands [76]. Electron transfer from non-precious metals into Pt has been reported to induce re-hybridization of the *d*-band, resulting in a positive shift of the Pt4f core levels [14–16]. The present results indicate that Pt-Fe, Pt-Co and Pt-Ni alloys have been successfully formed.

Fig. 7-3 (a)–(c) show XPS spectra of Fe2p_{3/2} for Pt-Fe, Co2p_{3/2} for Pt-Co, and Ni2p_{3/2} for Pt-Ni, respectively. The core levels of Fe2p_{3/2}, Co2p_{3/2} and Ni2p_{3/2} also slightly shift to the positive direction compared with the sputtered samples of Fe [25], Co [27] and Ni metal [28]. Small shoulders observed in Fe and Co suggest the coexistence of small amount of iron and cobalt oxides. The compositions of Pt alloys are calculated from the peak area of XPS spectra, giving the compositions of Pt₅₅Fe₄₅, Pt₅₀Co₅₀, and Pt₅₀Ni₅₀.

7.3.2 Rate constant of ORR

In order to evaluate the ORR activities for the Pt-alloys, j_k was measured in

EMPy_r(FH)_{1.7}F by the RDE method and the rate constant for ORR (k) was calculated using the following equation:

$$j_k = nFkC \quad (7-1)$$

where the values of n for Pt and Pt alloys were assumed to be 4.

Fig. 7-4 shows Arrhenius plots of rate constants for ORR on the Pt, Pt-Fe, Pt-Co and Pt-Ni electrode in EMPy_r(FH)_{1.7}F at 298–333 K. In this temperature range, the Pt-Fe exhibits a higher ORR activity than that of Pt. The rate constant on the Pt-Fe electrode is 16 times larger than that on the Pt electrode at 298 K. The higher ORR activities on Pt-Fe alloy electrode have also been reported for aqueous solution systems [13, 15, 16]. On the other hand, in the present study, the Pt-Co and Pt-Ni exhibit slightly lower ORR activities than that found for Pt.

From the Arrhenius plots, the activation energies of ORR on Pt, Pt-Fe, Pt-Co and Pt-Ni are estimated as 30.8, 26.4, 33.6, and 28.0 kJ mol⁻¹, respectively. The activation energies on Pt and Pt alloys are almost the same value. These values are different from those reported in the previous study on Pt, Pt-Fe, Pt-Co and Pt-Ni (*ca.* 40 kJ mol⁻¹ in 0.1 M HClO₄ [12]). The same ORR mechanism as in the acidic aqueous solution, in which the rate determining step of ORR is a dissociative adsorption of oxygen to the Pt electrode, would also proceed in FHIL. For this reason, fluorohydrogenate anion might affect the dissociative adsorption of oxygen.

7.3.3 XPS analysis after electrochemical measurement

The compositions of Pt alloys after the electrochemical measurements were calculated from the peak areas of XPS spectra. Broken curves in Fig. 7-2 and Fig. 7-3

show Pt4f_{7/2} and Pt4f_{5/2} XPS spectra for Pt, Pt-Fe, Pt-Co and Pt-Ni after the electrochemical measurements. Compositions of Fe, Co, and Ni decreased to give compositions, Pt₉₁Fe₉, Pt₆₀Co₄₀, and Pt₅₁Ni₄₉. In other words, most of Fe in Pt-Fe and part of Co in Pt-Co are dissolved into the ionic liquid, whereas Ni in Pt-Ni remains during the electrochemical measurement. Since the composition of Pt-Fe is almost unchanged even after the Ar ion bombardment, Fe is lost even from the bulk of the sample. As is expected from the Pt-rich composition, the peak shifts of Pt4f were not observed for the Pt-Fe alloy after the electrochemical measurement. These results indicate that the high ORR activity of Pt-Fe is not due to the nature of alloy itself but due to the higher Pt surface area, resulting from the Fe leaching out of the alloy. In the case of phosphoric acid fuel cells, Stonehart et. al reported that the similar phenomena have been found in a series of alloy systems such as Pt/V, Pt/Cr, Pt/Co and Pt/Cu [12].

7.3.4 FE-SEM observation

The surfaces structures of the electrodes were observed by FE-SEM before and after electrochemical measurement. Fig. 7-5 (a) shows an image of the pristine Pt substrate for reference. Figs. 7-5 (b-1) and (b-2) show the images of the Pt-coated Pt electrode before and after the electrochemical measurement, respectively. Comparing (b-1) and (b-2), it can be seen that there was no obvious change in surface structure after the electrochemical measurement. Figs. 7-5 (c-1) and (c-2) exhibit images of the Pt₅₅Fe₄₅-coated Pt electrode both before and after electrochemical measurement, respectively. A nanoporous structure was observed for the Pt-Fe alloy after electrochemical measurement, as shown in (c-2). This result confirms the assumption mentioned above that the enhancement of ORR activity was due to the rougher surface

brought about by the leaching of Fe from the alloy. Figs. 7-5 (d-1) and (d-2) show images of the Pt₅₀Co₅₀-coated Pt electrode before and after electrochemical measurement, respectively. In (d-2), although a nanoporous Pt structure is partially observed, most of the surface is covered with a non-porous structure. The composition of Pt₆₀Co₄₀, as observed by XPS after the electrochemical measurement, is explained by the fact that the surface was mainly covered with the original Pt₅₀Co₅₀ and was only partially covered with the nanoporous Pt. Since the ORR activity of the original Pt₅₀Co₅₀ was much lower than that of the Pt, the observed activity for the Pt-Co electrode was also lower than that for the Pt electrode. Figs. 7-5 (e-1) and (e-2) show images of Pt₅₀Ni₅₀-coated Pt electrode both before and after electrochemical measurement, respectively. Morphologies did not change significantly. This is consistent with the minimal change in composition. Since Ni was barely dissolved in the EMPyr(FH)_{1.7}F, the ORR activity was mainly attributable to the bulk Pt-Ni which was lower than that of Pt in EMPyr(FH)_{1.7}F.

7.4 Conclusion

Rate constants of ORR (k) on the Pt, Pt-Fe, Pt-Co and Pt-Ni electrodes were evaluated in EMPyr(FH)_{1.7}F at 298–333 K. Among them, the Pt-Fe electrode exhibits the best catalytic activity in EMPyr(FH)_{1.7}F due to its large surface area of nanoporous structure remained after the dissolution of Fe. From XPS analysis and FE-SEM observation, it was found that Co and Ni barely dissolved into the FHIL. Thus, the ORR activities observed at these alloys were those of bulk Pt-Co and Pt-Ni, which was lower than that of Pt in EMPyr(FH)_{1.7}F.

References

- [1] M. Nesselberger, S. Ashton, J. C. Meier, I. Katsounaros, K. J. J. Mayrhofer, M. Arenz, *J. Am. Chem. Soc.* **133** (2011) 17428.
- [2] W. Sheng, S. Chen, E. Vescovo, Y. Shao-Horn, *J. Electrochem. Soc.* **159** (2011) B96.
- [3] M. M. Saleh, M. I. Awad, F. Kitamura¹, T. Ohsaka, *Int. J. Electrochem. Sci.* **7** (2012) 12004.
- [4] M. Watanabe, H. Sei, P. Stonehart, *J. Electroanal. Chem.* **261** (1989) 375.
- [5] P. G. Corradini, F. I. Pires, V. A. Paganin, J. Perez, E. Antolini, *J. Nanopart. Res.* **14** (2012) 1080.
- [6] C. Wang, H. Daimon, T. Onodera, T. Koda, S. Sun, *Angew. Chem. Int. Ed.* **47** (2008) 3588.
- [7] Mark Winter, http://www.webelements.com/periodicity/abundance_crust/, accessed on February 4th, 2013.
- [8] S. Mukerjee, S. Srinivasan, *J. Electroanal. Chem.* **357** (1993) 201.
- [9] E. Antolini, J. R. C. Salgado, M. J. Giz, E. R. Gonzalez, *Int. J. Hydrogen Energy* **30** (2005) 1213.
- [10] J. T. Glass, G. L. Cahen, Jr., *J. Electrochem. Soc.* **135** (1988) 1650.
- [11] M. T. Paffett, J. G. Beery, S. Gottesfeld, *J. Electrochem. Soc.* **135** (1988) 1431.
- [12] P. Stonehart, Ber. Bunsenges, *Phys. Chem.* **94** (1990) 913.
- [13] N. Wakabayashi, M. Takeichi, H. Uchida, M. Watanabe, *J. Phys. Chem. B* **109** (2005) 5836.
- [14] V. Stamenkovic, B. S. Mun, K. J. J. Mayrhofer, P. N. Ross, N. M. Markovic, J. Rossmeisl, J. Greeley, J. K. Nørskov, *Angew. Chem. Int. Ed.* **45** (2006) 2897.

- [15]H. Uchida, H. Yano, M. Wakisaka, M. Watanabe, *Electrochemistry* **79** (2011) 303.
- [16]M. Watanabe, D. A. Tryk, M. Wakisaka, H. Yano, H. Uchida, *Electrochim. Acta* **84** (2012) 187.
- [17]B. P. Vinayan, R. Nagar, N. Rajalakshmi, S. Ramaprabhu, *Adv. Funct. Mater.* **22** (2012) 3519.
- [18]S. Mukerjee, S. Srinivasan, M. P. Soriaga, *J. Phys. Chem.* **99** (1995) 4577.
- [19]S. Mukerjee, S. Srinivasan, M. P. Soriaga, J. McBreen, *J. Electrochem. Soc.* **142** (1995) 1409.
- [20]M. Lefevre, E. Proietti, F. Jaouen, J. Dodelet, *Science* **324** (2009) 71.
- [21]J. Ozaki, S. Tanifuji, A. Furuichi, K. Yabutsuka, *Electrochim. Acta* **55** (2010) 1864.
- [22]M. Neergat, R. Rahul, *J. Electrochem. Soc.* **159** (2012) F234.
- [23]R. Lin, C. Cao, T. Zhao, Z. Huang, B. Li, A. Wieckowski, J. Ma, *J. Power Sources*, **223** (2012) 190.
- [24]P. Mills, J. L. Sullivan, *J. Phys. D.* **16** (1983) 723.
- [25]E. Paparazzo, *J. Phys. D.* **20** (1987) 1091.
- [26]S. L. T. Andersson, R. F. Howe, *J. Phys. Chem.* **93** (1989) 4913.
- [27]N. S. Mc Intyre, D. D. Johnston, L. L. Coatsworth, R. D. Davidson, J. R. Brown, *Surf. Interface Anal.* **15** (1990) 265.
- [28]J. Haber, L. Ungier, *J. Electron Spectrosc. Relat. Phenom.* **12** (1977) 305.
- [29]N. S. McIntyre, M. G. Cook, *J. Anal. Chem.* **47** (1975) 2208.

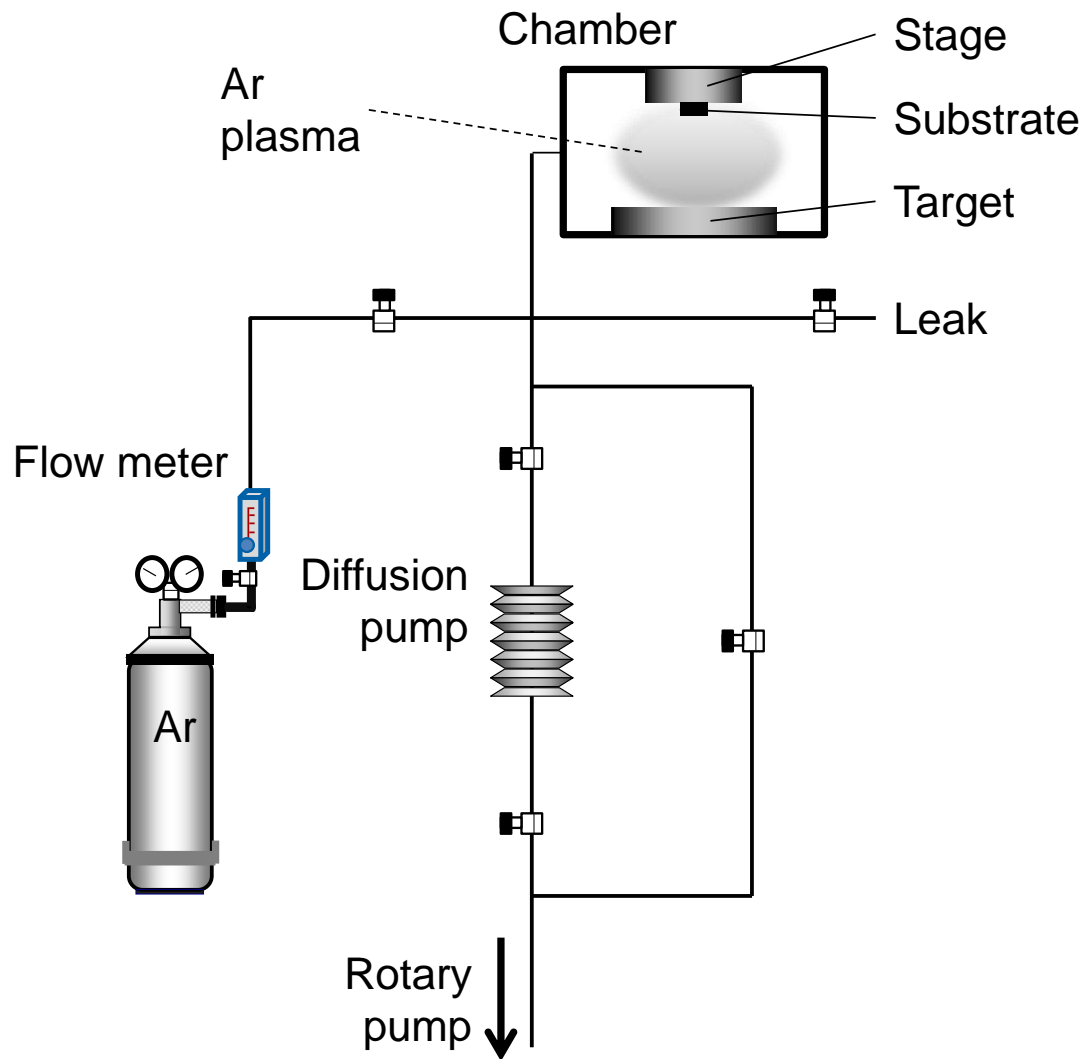


Fig. 7-1 Schematic representation of radio frequency magnetron sputtering deposition system.

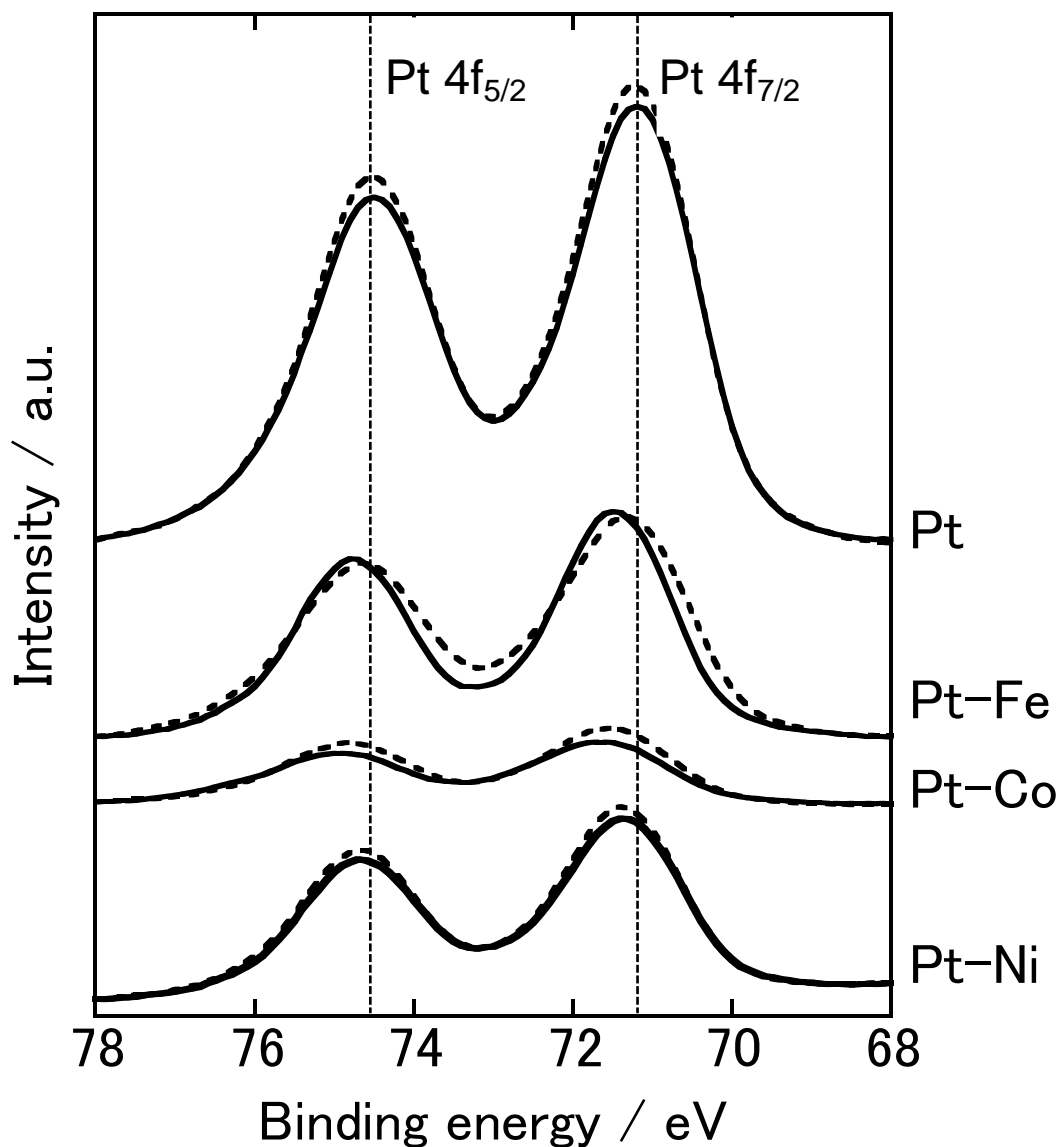


Fig. 7-2 XPS spectra of Pt4f_{7/2} and Pt4f_{5/2} for Pt, Pt-Fe, Pt-Co, and Pt-Ni before (solid curves) and after (broken curves) the electrochemical measurement in EMPyr(FH)_{1.7}F at 298–333 K. The dotted vertical lines indicate the peak energies of Pt4f_{7/2} and Pt4f_{5/2} for Pt.

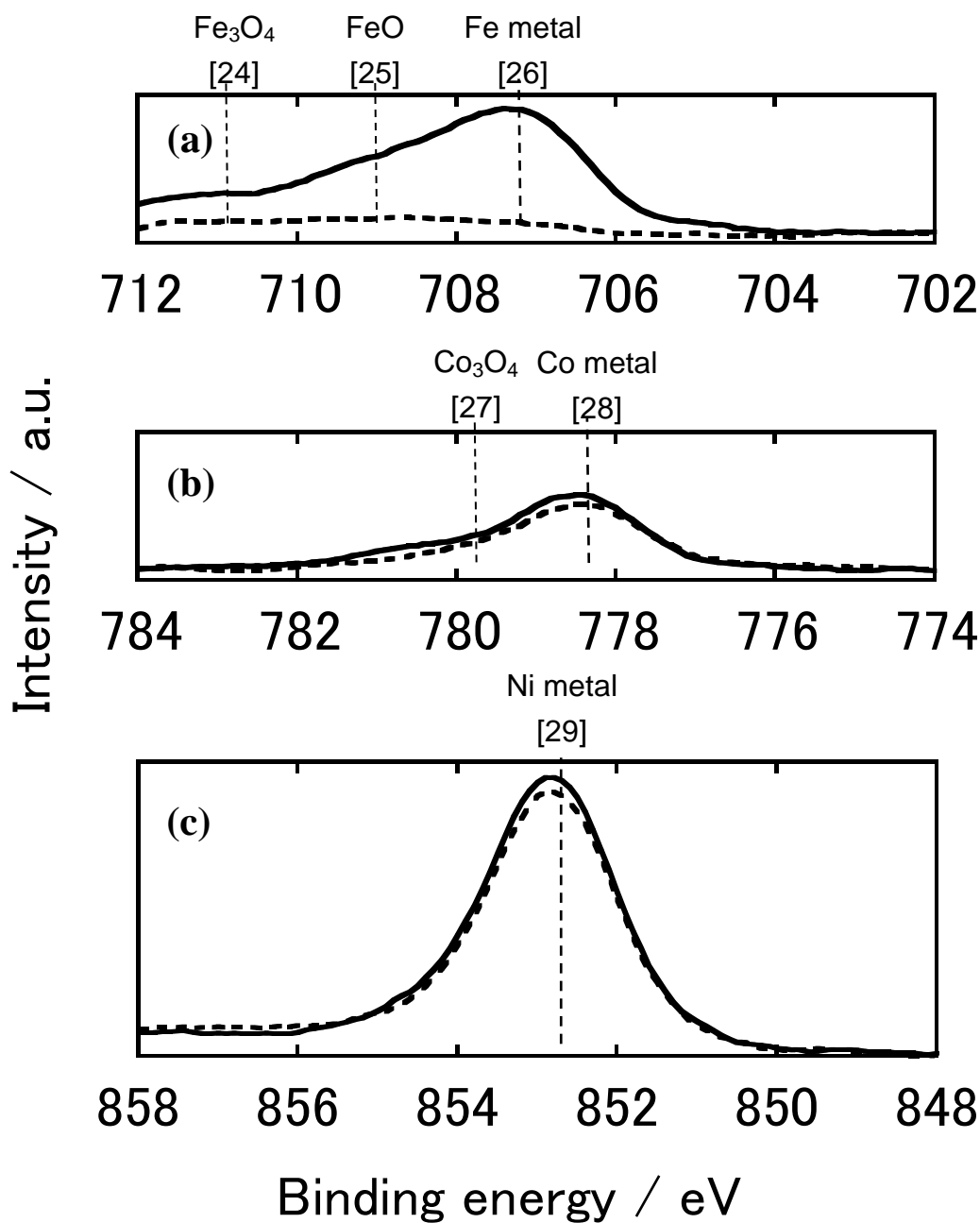


Fig. 7-3 XPS spectra of (a) Fe2p_{3/2} for Pt-Fe, (b) Co2p_{3/2} for Pt-Co, and (c) Ni2p_{3/2} for Pt-Ni before (solid curves) and after (broken curves) the electrochemical measurement in EMPyr(FH)_{1.7}F at 298–333 K.. The dotted vertical lines indicate the referential peak energies of Fe2p_{3/2} for Fe, Fe2p_{3/2} for FeO, Fe2p_{3/2} for Fe₃O₄, Co2p_{3/2} for Co, Co2p_{3/2} for Co₃O₄, and Ni2p_{3/2} for Ni.

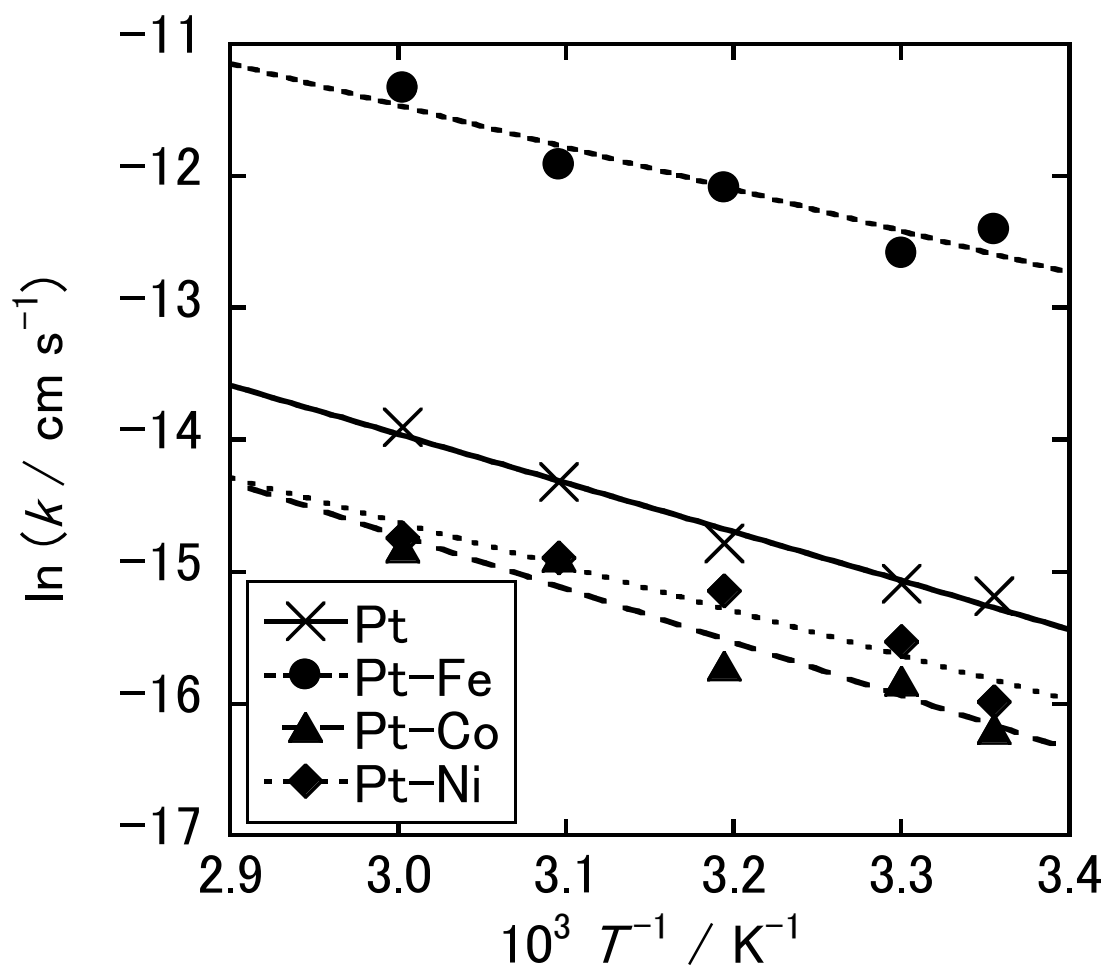


Fig. 7-4 Arrhenius plots of rate constant of ORR on Pt (\times), Pt-Fe (\bullet), Pt-Co (\blacktriangle), and Pt-Ni (\blacklozenge) in EMPyr(FH)_{1.7}F at 298–333 K. $E = 0.9$ V vs. RHE.

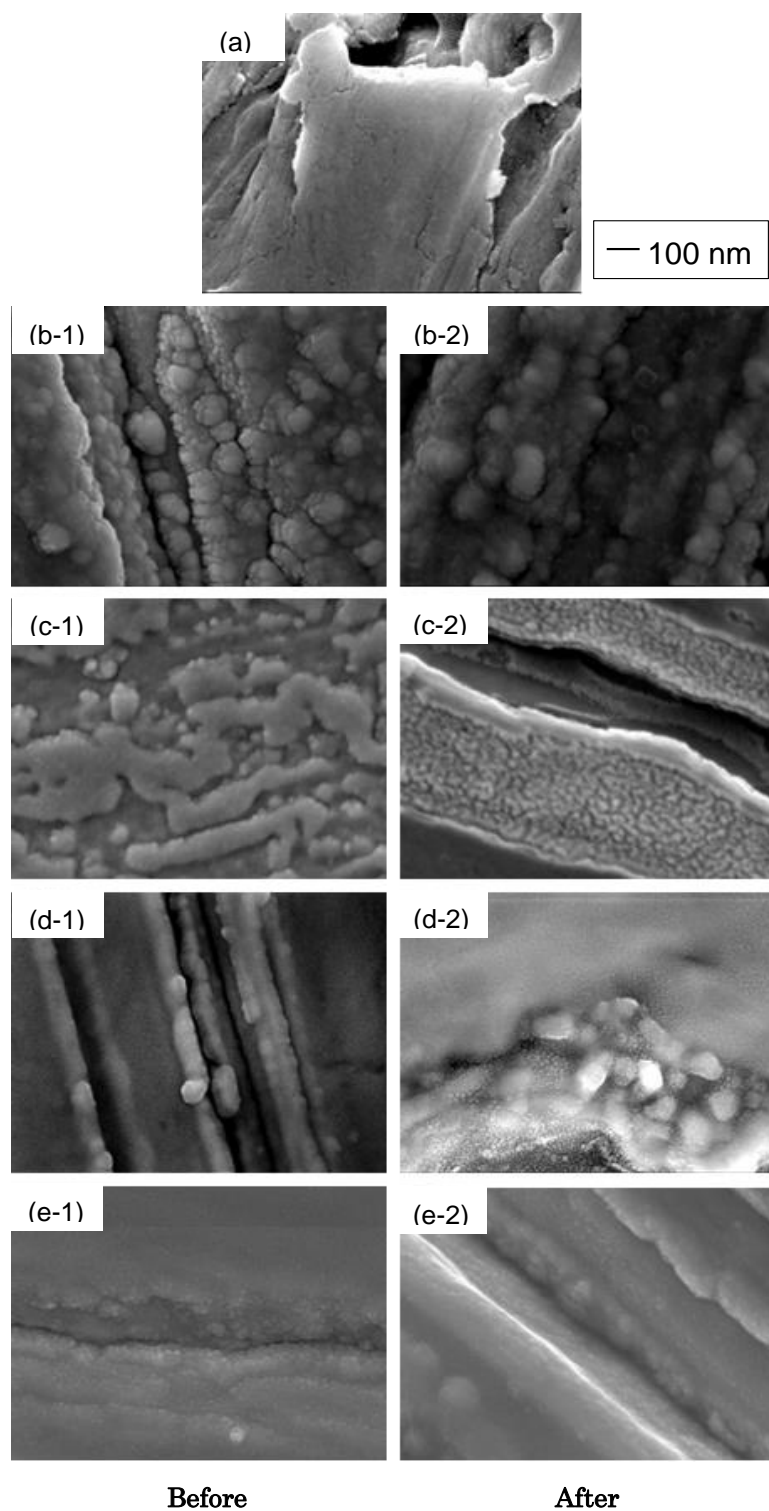


Fig. 7-5 FE-SEM images of (a) pristine Pt substrate, (b-1, b-2) Pt-coated, (c-1, c-2) Pt₅₅Fe₄₅-coated, (d-1, d-2) Pt₅₀Co₅₀-coated, and (e-1, e-2) Pt₅₀Ni₅₀-coated Pt electrodes before and after electrochemical measurement in EMPyr(FH)_{1.7}F at 298–333 K.

Chapter 8

General conclusion

Operation at intermediate temperature ($> 100\text{ }^{\circ}\text{C}$) without humidification offers several benefits such as reduction of expensive noble catalyst and simplicity of the unit for polymer electrolyte fuel cells (PEFCs). In contrast to the conventional PEFCs, fluorohydrogenate fuel cells (FHFCs) can be operated up to $120\text{ }^{\circ}\text{C}$ under nonhumidified conditions. In this study, various efforts have been made to further develop FHFCs which possess high cell performance and good stability.

In chapter 3, composite membranes consisting of EMPyr(FH)_{1.7}F and HEMA polymer were prepared. The composite membranes showed sufficient thermal stability up to $170\text{ }^{\circ}\text{C}$. The ionic conductivities of the EMPyr(FH)_{1.7}F–HEMA (9:1) composite membrane was 81.9 mS cm^{-1} at $120\text{ }^{\circ}\text{C}$. In the single cell tests, a maximum power density of 32 mW cm^{-2} was observed at $50\text{ }^{\circ}\text{C}$ under nonhumidified conditions. The deterioration of the single cell performance at $80\text{ }^{\circ}\text{C}$ is explained by the plug of gas flow in GDEs caused by the softening of the composite membrane at elevated temperatures.

In chapter 4, PI membrane supports have been used in place of PTFE in order to improve the mechanical properties of EMPyr(FH)_{1.7}F and HEMA composite membranes. TG analysis showed that the prepared composite membranes had good thermal stability up to $170\text{ }^{\circ}\text{C}$. Meanwhile, the EMPyr(FH)_{1.7}F–HEMA (9:1) composite membrane supported by a $16\text{-}\mu\text{m}$ -thick PI layer showed good ionic conductivity of 75 mS cm^{-1} at $120\text{ }^{\circ}\text{C}$. Nonhumidified single cell tests ranging from 25 to $120\text{ }^{\circ}\text{C}$ revealed that performance improved with temperature, a result that was distinct from previous

research using PTFE; a maximum power density of 31 mW cm^{-2} was observed at $120 \text{ }^\circ\text{C}$. Meanwhile, cross-sectional SEM images revealed no significant difference in membrane thickness as a result of testing, meaning that the problem of membrane softening and penetration to the GDE in chapter 3 has been solved.

In chapter 5, composite membranes consisting of EMPyr(FH)_{1.7}F IL and PVdF-HFP copolymer were successfully prepared by a casting method using acetone as the solvent. For the EMPyr(FH)_{1.7}F/PVdF-HFP (7:3 weight ratio) composite membrane, the ionic conductivity was 41 mS cm^{-1} at $120 \text{ }^\circ\text{C}$. In a single cell test, a maximum power density of 103 mW cm^{-2} was observed at $50 \text{ }^\circ\text{C}$ under nonhumidified conditions, which is the highest value among reported FHFCs. However, the cell performance decreased at $80 \text{ }^\circ\text{C}$. This deterioration is similar to that found in chapter 3. According to *in situ* a.c. impedance analyses and cross-sectional SEM observations of the MEAs, the deterioration was caused by penetration of the softened composite electrolyte into the gas diffusion electrodes, which decreased the three-phase boundary area in the CL and plugged gas channels in the GDL.

In chapter 6, the ORR was investigated in an attempt to improve the performance of fluorohydrogenate fuel cells from the viewpoint of the electrolyte. The influence of different cationic species on the ORR parameters were evaluated on a Pt electrode in EMIm(FH)_{1.3}F, EMIm(FH)_{2.3}F, EMPyr(FH)_{1.7}F, EMPyr(FH)_{2.3}F, S₁₁₁(FH)_{1.9}F, P₂₂₂₅(FH)_{2.1}F, and AS[4.4](FH)_{2.0}F at 298 K . The ORR parameters were kinetically limited current density (j_k), H₂O₂ yield ($X_{\text{H}_2\text{O}_2}$), solubility (C), and diffusion coefficient (D) of oxygen. EMPyr(FH)_{1.7}F showed the largest j_k value that could be explained by the low adsorbability of the EMPyr⁺ at the Pt surface as a result of the weaker interaction between EMPyr⁺ and Pt. The $X_{\text{H}_2\text{O}_2}$ values in EMPyr(FH)_{1.7}F,

EMPyr(FH)_{2.3}F, and P₂₂₂₅(FH)_{2.1}F were 1.6, 1.9, and 1.2%, respectively. The *C* and *D* values in these FHILs were considered to be appropriate for fuel cell application.

In chapter 7, rate constants of ORR (*k*) on the Pt, Pt-Fe, Pt-Co and Pt-Ni electrodes were evaluated in EMPyr(FH)_{1.7}F at 298–333 K. Among them, the Pt-Fe electrode exhibits the best catalytic activity in EMPyr(FH)_{1.7}F due to its large surface area of nano-porous structure remained after the dissolution of Fe. From XPS analysis and FE-SEM observation, it was found that Co and Ni barely dissolved into the FHIL. Thus, the ORR activities observed at these alloys were those of bulk Pt-Co and Pt-Ni, which was lower than that of Pt.

List of publications

Chapter 3

Pisit Kiatkittikul, Toshiyuki Nohira, Rika Hagiwara

Journal of Power Sources **2012**, 220, 10–14.

“Nonhumidified fuel cell using *N*-ethyl-*N*-methylpyrrolidinium fluorohydrogenate ionic liquid–polymer composite membranes”

Chapter 4

Pisit Kiatkittikul, Toshiyuki Nohira, Rika Hagiwara

Fuel Cells

Published online. (DOI: 10.1002/fuce.201400150)

“Advantages of a polyimide membrane support in nonhumidified fluorohydrogenate–polymer composite membrane fuel cells”

Chapter 5

Pisit Kiatkittikul, Toshiyuki Nohira, Rika Hagiwara

Journal of Power Sources

Submitted.

“Nonhumidified fuel cell using *N*-ethyl-*N*-methylpyrrolidinium fluorohydrogenate ionic liquid–poly(vinylidene fluoride-hexafluoropropylene) composite membrane”

Chapter 6

Pisit Kiatkittikul, Jumpei Yamaguchi, Ryosuke Taniki, Kazuhiko Matsumoto, Toshiyuki

Nohira, Rika Hagiwara

Journal of Power Sources **2014**, 266, 193–197.

“Influence of cationic structures on oxygen reduction reaction at Pt electrode in fluorohydrogenate ionic liquids”

Chapter 7

Pisit Kiatkittikul, Jumpei Yamaguchi, Toshiyuki Nohira, Rika Hagiwara

ECS Electrochemistry Letters

To be submitted.

“Catalytic activities of Pt-M alloys (M = Fe, Co, Ni) on oxygen reduction reaction in a fluorohydrogenate ionic liquid”

Acknowledgments

This thesis would not have been possible without the help, support and patience of my principal supervisor, Professor Rika Hagiwara. The invaluable support, guidance and freedom he gave me throughout this study have been a true blessing, not to mention his unsurpassed knowledge of Fluorine Chemistry. I am sincerely grateful to my second supervisor, Professor Toshiyuki Nohira, whose enlightening instructions, constant encouragement and fruitful discussions have been invaluable on both academic and personal terms.

I would like to extend my heartfelt appreciation to Assistant Professor Kazuhiko Matsumoto and Assistant Professor Kouji Yasuda for their helpful advices, assistances and technical instructions.

A special thank is given to Professor Takashi Sagawa for his fruitful discussions and suggestions.

I owe my gratitude to Mr. Jumpei Yamaguchi and Dr. Ryosuke Taniki, whose kindly helps, advices and co-operations have been extremely helpful, especially for the studies in chapter 6 and 7.

I truly appreciate the wholehearted helps, earnest discussions and warm encouragements I received from all the present and former members of Energy Chemistry Laboratory throughout this study. They have made my time here an enjoyable and unforgettable experience.

I wish to express my appreciation to the Ministry of Education, Culture, Sports, Science and Technology in Japan, for their financial supports for my living in Japan.

Last, but by no means least, I want to thank all my friends and family, whose

encouragements and supports are the source of my strength to overcome the bad times.

Not all acknowledgments are described here. Without any single helps I was given, this study could not be accomplished. I am truly thankful to all those who are related to this study.

March, 2015

Pisit Kiatkittikul